ABSTRACT

Title of Dissertation: OXYGEN EXCHANGE MECHANISMS ON SOLID OXIDE FUEL CELL CATHODE MATERIALS IN THE PRESENCE OF GAS PHASE CONTAMINANTS

Christopher R. Pellegrinelli, Doctor of Philosophy, 2016

Dissertation directed by: Professor Eric D. Wachsman, Department of Materials Science and Engineering, Department of Chemical and Biomolecular Engineering

Polarization losses associated with the oxygen reduction reaction (ORR) at the cathode and degradation of cathode materials remain as hurdles for high performance solid oxide fuel cells (SOFC). Rates of degradation depend significantly on the operating temperature and gas conditions, such as the presence of unwanted oxygen-containing compounds, namely H_2O and CO_2. In this study ORR fundamentals for the common cathode materials, $La_{0.6}Sr_{0.4}Co_{0.2}Fe_{0.8}O_{3-\delta}$ (LSCF) and $(La_{0.8}Sr_{0.2})_{0.95}MnO_{3\pm\delta}$ (LSM), as well as their composites with $Gd_{0.10}Ce_{0.90}O_{1.95}$ (GDC) and $(Y_2O_3)_{0.08}(ZrO_2)_{0.92}$ (YSZ), respectively, are evaluated as a function of operating environment. A combination of electrochemical impedance spectroscopy (EIS) and gas phase oxygen isotope exchange is used to probe the kinetics of heterogeneous gas-solid reactions and electrode performance under a wide range of conditions. The results suggest that CO_2 and H_2O actively participate in the ORR and that the level of participation and governing mechanisms are dependent on the specific conditions. It was found that CO_2 adsorbs readily on the surface of LSCF and leads to significant performance loss, while the affect of CO_2 on LSM, an arguably similar material, is minimal. We propose that intrinsic material properties, such as vacancy concentration, will alter the contaminant interactions significantly, leading to specific contaminant-material relationships. The ORR on LSM is compared to that on LSM-YSZ composite, where the triple phase boundary (TPB), gas-electrode-electrolyte interface, plays a vital role. Further, the role of water in both the single phase, and composite materials is explored. A new *in operando* isotope exchange technique that couples electrochemical polarization with gas phase isotopic transient and steady state results is proposed, and initial results discussed. The development of *in operando* experiments is crucial to gain a full understanding of electrodes under real operating conditions, where chemical species are being driven by an electrochemical potential. The results contribute to the understanding of gas-solid reaction kinetics on ion conducting catalysts, and provide a basis for future experimental investigations.

OXYGEN EXCHANGE MECHANISMS ON SOLID OXIDE FUEL CELL CATHODE MATERIALS IN THE PRESENCE OF GAS PHASE CONTAMINANTS

by

Christopher R. Pellegrinelli

Dissertation submitted to the Faculty of the Graduate School of the
University of Maryland, College Park, in partial fulfillment
of the requirements for the degree of
Doctor of Philosophy
2016

Advisory Committee:
Professor Eric D. Wachsman, Chair
Professor Bryan W. Eichhorn
Professor Lourdes G. Salamanca-Riba
Professor Chunsheng Wang
Associate Professor Liangbing Hu

Acknowledgements

I thank my advisor, Prof. Eric Wachsman, for the opportunity to perform this research and his continued guidance and support throughout the process.

I would also like to thank my project collaborators, Prof. Salamanca-Riba, and Josh Taillon. I owe a special thanks to Yi-Lin Huang for all of the time we spent together discussing impedance spectroscopy, oxygen isotope exchange, and a vast number of other topics.

I also thank Prof. Bryan Eichhorn and Aaron Geller for their “chemistry” point of view and many discussions.

I would also like to thank all of the members of the Wachsman research group for helping create a wonderful place to work.

Lastly, I would like to thank my friends and family for their encouragement and support.

Table of Contents

List of Tables

List of Figures

Chapter 1: Introduction

1.1 Solid Oxide Fuel Cells

The electrochemical conversion of fuels into electricity using solid oxide fuel cell (SOFC) technology is a promising alternative to more common combustion-based generation methods. SOFCs can provide both higher efficiencies and cleaner exhaust, reducing environmental impact. As many renewable energy technologies are non-dispatchable, SOFCs have attracted significant attention as a bridging technology that utilizes the current energy infrastructure[1–3].

A SOFC consists of three main components, a cathode, an electrolyte and an anode, where reduction, transport and oxidation take place, respectively. Fuel cells operate on principles similar to other electrochemical devices such as batteries, and rely on electronically separated Red-Ox reactions, which generate an electrochemical potential as described by the Nernst equation:

$$V_{th} = \frac{RT}{4F}\ln\left(\frac{P_{O_2}^{cath}}{P_{O_2}^{anode}}\right) \qquad [1.1]$$

PO_2^{anode} and PO_2^{cath} describe the oxygen partial pressures at the anode and cathode, and R, T and F are the gas constant, temperature, and Faraday constant, respectively. The theoretical voltage V_{th} is the electrical driving force arising from the oxygen chemical potential between O_2 and H_2. Figure 1.1 illustrates typical SOFC operation, which can be broken down into three steps. First, oxygen gas is reduced at the cathode from molecular oxygen, to oxygen ions. Then the oxygen ions are incorporated into the oxygen-conducting electrolyte and transported to the anode. Finally, at the anode, the oxygen ions oxidize a fuel. Movement of electrons through an external circuit compensates for transport of O^{2-} through the electrolyte, allowing for the extraction of useful work. The equations governing fuel cell operation are:

$$\frac{1}{2}O_2 + 2e^- \rightleftarrows O^{2-} \quad [1.2]$$

$$H_2 + O^{2-} \rightleftarrows H_2O + 2e^- \quad [1.3]$$

$$H_2 + \frac{1}{2}O_2 \rightleftarrows H_2O \quad [1.4]$$

where [1.2], [1.3] and [1.4] are the cathode, anode and overall reactions, respectively. As can be seen from the overall reaction, using H_2 as a fuel, the only product is H_2O. SOFCs differ from other fuel cell systems, such as PEM (proton exchange membrane), as they operate through anion transport. The transport of O^{2-} through a solid electrolyte requires elevated operating temperatures and limits the materials that can be used. Although this can be seen as a disadvantage for SOFCs, it also allows for use of a variety of fuels other than pure H_2, as the proton does not need to be transported through the electrolyte[4]. One alternate fuel for SOFCs is methane (CH_4), the main component in natural gas. The overall reaction using methane is:

$$CH_4 + 3O_2 \rightleftarrows CO_2 + 2H_2O \quad [1.5]$$

The properties of the materials chosen for each of the three layers are derivative of the basic SOFC function. The electrolyte material should have high O^{2-} and low e^- conductivity, blocking electron transport through the electrolyte, and "forcing the electrons through the external circuit. For the cathode and anode, the material should ideally have both high ionic and electronic conductivity to assist in the charge transfer reactions [1.2] and [1.3] and transport to/from the electrode electrolyte interface. Additionally, the cathode should be stable in oxidizing atmospheres, and the anode stable in reducing atmospheres, across the entire range of operation. Despite the advantages of SOFCs over other generation technologies, there remain some significant issues, namely the performance and stability of cathode materials[5–8].

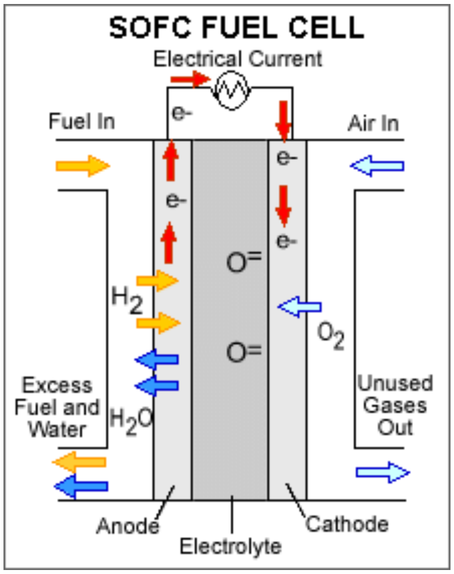

Figure 1.1: A diagram describing the fundamental operation of solid oxide fuel cells. Oxygen from the cathode side of the cell is transported across an electronically insulating oxygen conductor to the anode, where it oxidizes a fuel. Movement of electrons in an external circuit compensates the movement of O^{2-} ions in the cell[9].

1.2 Cathodes

As stated previously, the purpose of the cathode in an SOFC is to catalyze what is commonly referred to as the oxygen reduction reaction (ORR). The ORR is a multi-step heterogeneous reaction involving the reduction of gaseous O_2 molecules to O^{2-} ions that can then be incorporated into the electrolyte. It is generally accepted that there are at least two steps comprising the overall ORR for SOFC cathode materials[10–12]:

(1) Adsorption (dissociative):

$$\frac{1}{2}O_2 + * \rightleftharpoons O^* \qquad [1.6]$$

(2) Incorporation:

$$O^* + V_O \rightleftharpoons O_O + * \qquad [1.7]$$

where $*$ denotes an available surface site, and V_O and O_O denote an oxygen vacancy and an occupied oxygen site, respectively. A high performance cathode needs to be catalytically active toward the dissociation of oxygen, as the O-O bond is strong (498 kJ mol^{-1})[11].

Suitable candidates for cathodes should meet the criteria of high catalytic activity and high electronic conduction. Perovskite oxides with the chemical formula ABO_3 are most promising structure for SOFC cathodes due to its tunable properties and low cost. Two of the most common perovskite cathodes are $La_{1-x}Sr_xMnO_{3\pm\delta}$ (LSM) and $La_{1-x}Sr_xCo_yFe_{1-y}O_{3-\delta}$ (LSCF)[13–16]. Although these two materials both have perovskite structures their properties are quite different. LSM is an electronic conductor, and is highly catalytic toward the ORR. However, as a majority electronic conductor LSM provides limited oxygen ion conductivity, confining reactions to the triple phase boundary (TPB) region where oxygen gas, cathode and electrolyte meet.[15,17] On the other hand, LSCF is a mixed ionic-electronic conductor (MIEC) with predominant electronic conduction, extending the active region of the cathode beyond the TPB through the high oxygen ion conduction in bulk [15,16].

The differences between LSM and LSCF arise from the transition metals occupying the B-sites in the lattice. In LSM, Mn prefers to have 3+ and 4+ valence states at high temperature and low PO_2, meaning that the oxygen stoichiometry of the material remains relatively constant[18,19] over a wide range of temperature and PO_2. In contrast, Co and Fe tend to decrease their valence states, moving toward 3+ and 2+, as temperature increases, resulting in the creation of oxygen vacancies to compensate[20–22]. There are a greater number of vacancies for LSCF than LSM as temperature increases, and as a result the oxygen conductivity for LSCF is also greater.

In SOFC cathodes, the existence of TPB is necessary to provide reaction sites for electron, ions, and gasses to meet. A common solution for the lack of active area for the ORR on LSM are composite cathodes containing a mixture of LSM particles with the electrolyte yttria-stabilized zirconia (YSZ)[23,24]. Composite LSM-YSZ cathodes increase the effective TPB significantly, and are a common cathode material for industry. Similarly, LSCF is often mixed with gadolinia doped ceria (GDC) in an attempt to improve the performance of LSCF cathodes[25]. The use of GDC as an electrolyte for LSCF arises from the higher ionic conductivity of GDC than YSZ and the reaction between LSCF and Zr in YSZ[26]. However, the performance enhancement of LSCF-GDC composite over pure LSCF is not as readily observed as LSM-YSZ composite over pure LSM, due to the already mixed conducting nature of LSCF.[25,27]

1.3 Performance Losses in SOFCs

As discussed previously, the Nernst equation describes the open circuit voltage of an SOFC, and is a function of the PO_2 on the anode and cathode sides of the cell. The maximum theoretical voltage for a fuel cell can be calculated using the Nernst potential, however it is never achieved due to losses associated with each component in the fuel cell and the temperature required for operation. The voltage drop is the sum of a number of different losses throughout the cell. Ohmic, is mainly associated with the ionic conductivity of the electrolyte, and as indicated by the name, scales linearly with increasing current density. Additionally, there are overpotential losses that arise from the activation of the electrodes, e.g. the resistances of the charge transfer processes at the cathode and anode. Finally, we also have to consider that under high current density conditions there can be an additional voltage drop due to a concentration gradient in the gas phase, where transport of the O_2 or H_2 is limiting the reaction. In summary, the performance of an SOFC is controlled by losses arising from activation, ohmic and concentration polarizations.

Activation polarization losses in cathodes are of particular concern, as ORR kinetics can be slow, limiting cell performance. Figure 1.2 shows the voltage profile of a typical cell and the losses attributed to the cathode, anode and electrolyte as functions of temperature. It is clearly shown that there is a decrease in cell voltage, and that the losses associated with the cathode become larger, as operation temperature decreases, contributing relatively greater losses than the other two cell components. Additionally, there has been a push in the SOFC community to decrease the operating temperature for SOFCs[1]. At lower operating temperatures the cost of components decreases, cheaper metallic parts can replace expensive ceramic ones. As shown in Figure 1.2 the fraction of losses associated with the cathode increase with decreasing temperature.

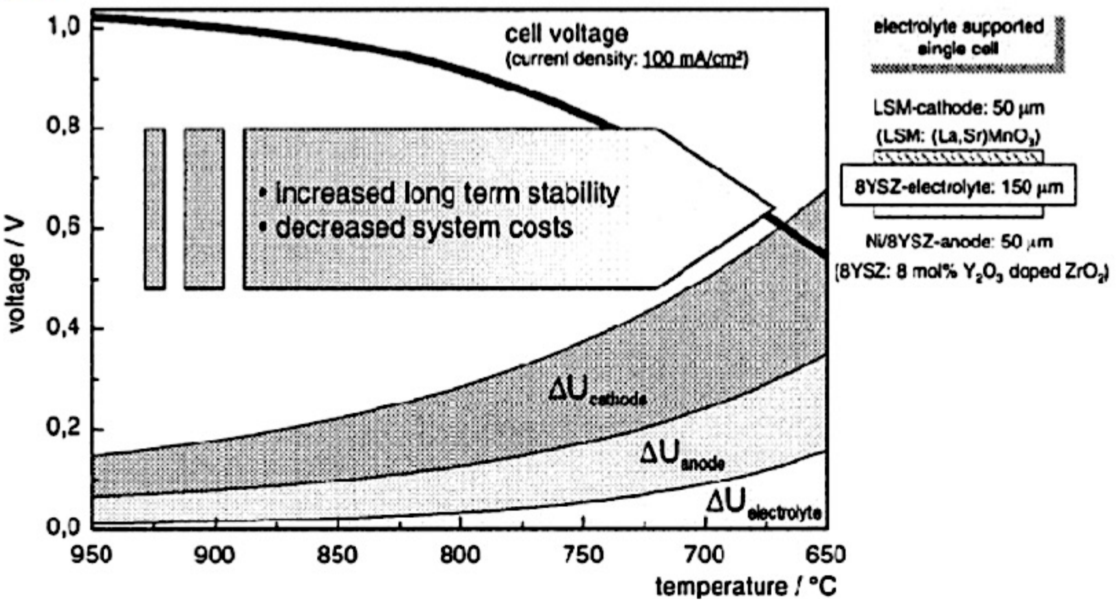

Figure 1.2: Voltage profile of a typical SOFC as a function of temperature. Included are voltage losses for the cathode, anode and electrolyte. As temperature decreases, the proportion of losses associated with the cathode increases[8].

1.4 Cathode Degradation

In addition to potential losses associated with the ORR, there are also issues regarding the degradation of cathode materials[7,28,29]. Cathode degradation can be separated into two key categories, reversible and irreversible degradation[30]. As indicated by the names, reversible degradation can be recovered from, while irreversible degradation is permanent. A good example of reversible degradation is the adsorption of unwanted molecules that block sites for the ORR, better known as "poisoning" in catalysis[11]. Irreversible degradation consists of physical or chemical degradation. Physical changes in the cathode, such as delamination from the electrolyte or coarsening of the microstructure change the morphology of cathodes, leading to degradation. Chemical degradation includes both inter-diffusion, precipitation/phase segregation, and secondary phase formation, and is mostly irreversible[6,29,31]. However, some secondary phases can be removed through thermal treatment or the application of a voltage. The latter has been shown for the removal of SrO that has formed on the surface of LSM[32].

Contaminants such as H_2O, CO_2 and Cr can enhance degradation of cathode materials[30,33–38]. The degradation that occurs is dependent on the cathode material and the contaminant and different combinations have different interactions. More surface-active materials such as LSCF are more reactive with CO_2, forming high concentrations of surface carbonates. The surface carbonates can often be removed through some thermal, pure-O_2 treatments, however irreversible degradation such as the precipitation of SrO from the lattice can arise, permanently decreasing the performance of the cathode. In such a case, strontium carbonate is a reaction intermediate, catalyzing the separation of Sr from the LSCF lattice[39].

The chemical relationship between contaminants and the material is important, however, it is equally important to consider the effects of contaminants on physical properties such as cathode microstructure. Microstructure consists of important performance characteristics such as porosity, surface area, and two/three phase boundaries. Changes in these parameters will not change the intrinsic material properties, but can change the effectiveness of the cathode[24,40,41]. A full understanding of cathode degradation therefore needs to include the relationship between contaminants and chemical kinetics, as well as contaminants and cathode microstructure.

Degradation of cathode materials is a real issue and improvement of cathode durability under operating conditions has the potential to significantly increase the overall performance of SOFCs. In order to determine the methods for enhancing cathode stability, a deeper understanding of the mechanisms is required. In this study degradation of the two most common cathode materials in industry, composites of LSM-YSZ and LSCF-GDC were investigated using a range of techniques. More specifically, the effects of H_2O and CO_2 were determined, and rates of degradation and identify the mechanisms by which degradation occurs. Fundamentally, there are two ways in which the contaminants can interact with the cathodes; causing changes in either the chemical (kinetic) or physical properties of the material. Using techniques that probe kinetics, conductivity and microstructure, we aim to elucidate both chemical and physical degradation, and the role of operating conditions in the degradation process. The knowledge obtained can then be used to enhance the performance and durability of SOFC cathodes. This dissertation discusses the mechanisms that govern contaminant-cathode reactions, with a focus on their effect on the overall ORR.

Chapter 2: Experimental Techniques

There are a number of techniques to investigate reaction mechanisms in SOFC cathodes, including contaminant reactions that lead to material instability and performance degradation. SOFC performance is determined by two main factors: ORR kinetics and cathode microstructure, where kinetics is derivative of the fundamental material properties, and the microstructure is controlled by fabrication methods, including the use of composite electrodes. Using gas phase oxygen isotope exchange and electrochemical impedance spectroscopy (EIS), we can determine the elementary reactions of O_2, H_2O and CO_2 on common cathode materials, and how the ORR kinetics change in a realistic electrode under working conditions. Details regarding the theory and experimental of EIS and isotope exchange are provided in the following.

2.1 Electrochemical Impedance Spectroscopy

Electrochemical impedance spectroscopy (EIS) is a powerful tool for investigating the movement of charged species and is used in a number of different fields, ranging from biology to corrosion studies.[42,43] One area that EIS has been deemed particularly useful is in solid-state electrochemistry. The response (impedance) of the system (material(s)) to a sinusoidal perturbation at fixed frequency is analogous to chemical and physical processes with distinct time constants. Using an electrical model, such as an equivalent circuit, that is representative of these chemical and physical processes, we can extract useful information from the impedance measurements. EIS has been used often to study the performance and kinetics of SOFC cathodes.[40,44–48] Impedance spectra contain substantial quantitative data, however the information can only be extracted through the use of an appropriate model. Fitting impedance spectra can provide information regarding the solid-state conductivity of the cathode material, as well as kinetics of the ORR[27,32,49]. Further, EIS is an *in situ* technique, and can therefore be used to investigate cathode materials as a function of operating condition.

2.1.1 Theory

Fundamentally, EIS uses an AC signal perturbation to probe the response of a system, which is later analyzed in terms of the dependence of the response on the applied frequency. In a typical EIS experiment the sample is excited using an AC current of a predetermined frequency and amplitude. The current response is recorded and used to calculate impedance, a combination of resistance and phase shift. This measurement is then repeated across a range of discrete frequencies and the resistance and phase shift recorded for each.

The impedance (Z) is a complex relationship between the sinusoidal input current (I_t) and voltage response (E_t) signals. Using Ohm's law we can relate E_t and I_t:

$$Z = \frac{E_t}{I_t} \quad [2.1]$$

Substituting E_0 and I_0 to describe the amplitude of each signal, and ϕ for the phase shift of the response, we get:

$$\frac{E_0 \sin(\omega t+\phi)}{I_0 \sin(\omega t)} = Z_0 \frac{\sin(\omega t+\phi)}{\sin(\omega t)} \quad [2.2]$$

where Z_0 is the magnitude of the impedance response. Using Euler's formula we can describe the impedance as a function of frequency (ω), as a complex function with real and imaginary components.

$$Z(\omega) = Z_0(\cos(\phi) + j\sin(\phi)) \quad [2.3]$$

Equation 2.3 provides the basis for Nyquist plots, where the x-axis is the real portion of the response and the y-axis the imaginary portion. These are commonly denoted Z' and Z'' for real and imaginary, respectively. Another common method for plotting impedance is using Bode plots, where Z_0 and ϕ are both plotted as functions of frequency. Both methods are useful for qualitative analysis of impedance spectra.

$$Z' = Z_0 \cos(\phi)\,;\ Z'' = Z_0 \sin(\phi) \qquad [2.4]$$

The most common technique for fitting impedance spectra is through the use of equivalent circuit models. These circuit models use common discrete components (i.e. resistors, capacitors, and inductors) to describe the electrochemical processes occurring in the sample. A circuit that is often used to represent a simple electrochemical interface, is the Randles circuit[50], comprised of a resistor in series with a parallel resistor and capacitor. A schematic a simplified Randles circuit is shown in Figure 2.1, where R_1 represents the resistance of an electrolyte, and C a double layer capacitance and R_2 a charge transfer resistance, both associated with the charge transfer process at the electrode electrolyte interface. The charge transfer process is described by a time constant (τ), and a characteristic frequency (ω_0), where τ = RC and ω_0 = 1/RC.

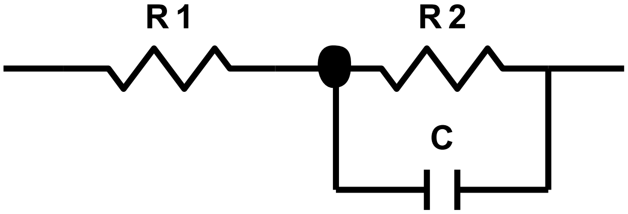

Figure 2.1: Schematic of a simple Randles circuit (cell), representing the resistance of the electrolyte (R_1) and a charge transfer process (R_2-C) at the electrode/electrolyte interface.

2.1.2 Experimental Setup

A typical impedance spectroscopy measurement is carried out using a frequency response analyzer (FRA) capable of generating a discrete sinusoidal signal over a wide range of frequencies, and measuring the magnitude and phase response. In an electrochemical experiment where driving the system in a particular direction, as is the case in an operating fuel cell, a direct current (DC) signal can be added using a potentiostat/galvanostat. The systems are often coupled/integrated using a commercial software package.

Figure 2.2 is schematic of the set-up used for electrochemical measurements in this study. The set-up consists of an 8-channel 1470E Cell Test System (Solartron Analytical) potentiostat/galvanostat combined with an 8-channel 1400 chassis (Solartron Analytical) with eight separate FRAs, controlled using MultiStat software (Scribner). The 1470E/1400 combination is capable of controlling 8 separate measurements simultaneous on each of its channels. The software has a variety of preprogrammed measurements, including EIS and potentiostatic/galvonastatic variation and holds. The frequency range of the 1451 FRA cards is 10μHz to 100kHz. The 1470E has a set of four cables that are connected to each channel for performing four-wire measurements. A working electrode (WE), counter electrode (CE), reference electrode 1 (RE1) and reference electrode 2 (RE2). The generated signal is applied through across the WE and CE and the measured response between the RE1 and RE2.

Samples are loaded into a custom built reactor capable of testing cells in a single gas environment, controlled using a variety of gas tanks and mass flow controllers. Additionally, a fritted glass impinger is including for humidified gas studies. The reactor is heated to SOFC operating temperatures using a furnace and temperature controller monitoring the temperature at the cell using a K-type thermocouple (TC).

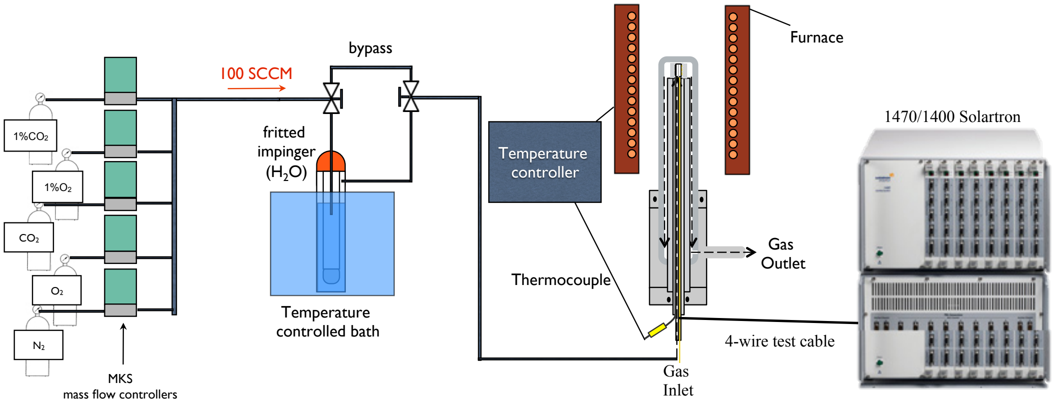

Figure 2.2: Drawing of the experimental set-up for *in situ* EIS measurements. The design includes multiple gas tanks and mass flow controllers (MFCs), along with a fritting glass impinger for incorporation of water, to control the cell environment. A temperature controlled and furnace maintains a steady sample temperature, controlled by a thermocouple (TC) located next to the sample, inside the reactor test fixture. A 1470E/1400 Cell Test System (Solartron Analytical) is used for electrochemical measurements, including impedance spectroscopy.

2.1.3 Equivalent Circuit Analysis

A simple circuit composed of discrete circuit elements (resistors and capacitors), often referred to as a "dummy cell", is often used to test EIS equipment and fitting software. Measurements performed on a dummy cell configured as a simplified Randles cell, using the equipment described above, are provided in Figure 2.3. In the measurement, an AC input signal is applied across the entire sample using the WE and CE wires. The signal response was measured between three sets of points, depicted by the symbol "V" for a voltage measurement, across the entire cell, R_1 only, and R_2-C, between the RE_1 and RE_2 probes. The results are shown in the characteristic Bode and Nyquist plots in Figure 2.3 (b) and (c) and Figure 2.3 (d), respectively. In the Bode plots, we can see the magnitude $|Z|$ and phase ϕ responses as a function of frequency. Where the R-C portion of the circuit results in a maximum phase shift centered on ω_0, and $|Z|$ increases as a function of decreasing frequency. While Bode plots are ideal for conveying frequency dependent data, they can sometimes be challenging to extract qualitative information about the overall resistance of a process such as charge transfer, especially when multiple processes may be present. A Nyquist plot on the other hand, can offer a clearer picture of the various processes occurring in the cell.

The response observed for R_1, corresponding to the placement of RE1 and RE2 shown in blue in Figure 2.3 (a) and the blue data points in (b) – (e), is just that for a simple resistor. There is no change in $|Z|$ and ϕ is zero across the entire range of frequencies measured. This results in a single point on the Z' axis for a Nyquist plot, highlighted in Figure 2.3 (e), where the imaginary portion of the impedance is zero. Adding a little complexity, we can observe the response to the R-C parallel circuit, shown in red. The R-C circuit results in $\phi = 90°$ at high frequency with $|Z| = 0$, and ϕ decreases with decreasing frequency while $|Z|$ increases. Plotted as Z' versus Z" a parallel R-C circuit yields a semi-circle that increases along Z', with decreasing frequency (as can be seen in the $|Z|$ Bode plot). The arc has a high-frequency Z'-intercept at $Z' = 0$ and a low frequency intercept at $Z' = R_2$. Measuring the response of the entire circuit, we get the result shown in black. The $|Z|$ response and Z'-Z" plot yield results very similar to those acquired for just the R-C parallel components. The difference is just a shift in the real impedance, where the high frequency intercept $Z' = R_1$ and the low frequency intercept $Z' = R_1 + R_2$. This semi-circle or arc shifted along the Z' axis is a good analog to a simple electrochemical interface, and a good starting point for constructing an equivalent circuit to model SOFC electrodes.

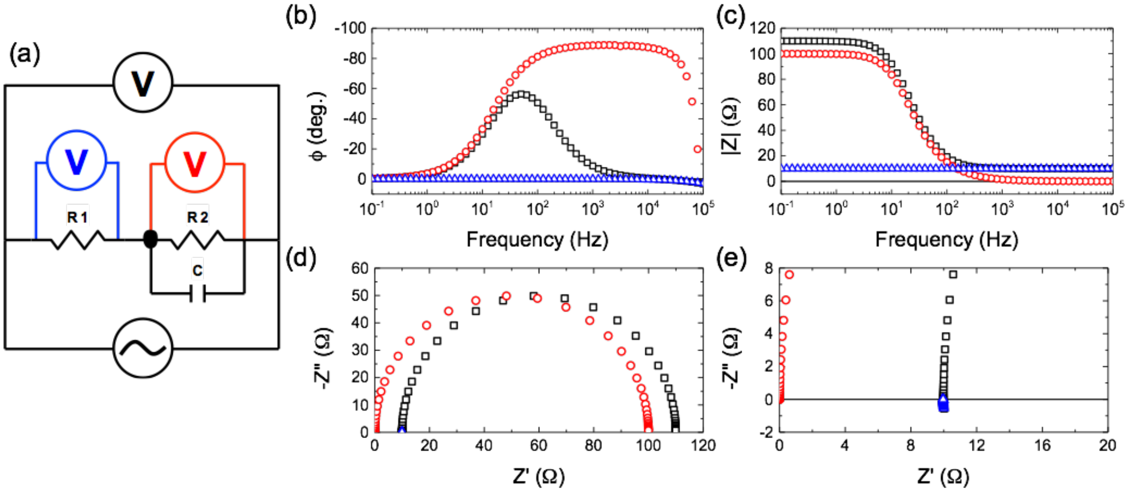

Figure 2.3: Schematic of a "dummy cell" (a) used to check impedance spectroscopy measurements and fitting. The cell is composed of a simple Randal's circuit with a resistor in series with a resistor and capacitor in parallel. An AC current, depicted as "~", is applied across the entire cell and voltage response measured across different portions of the cell, shown as "V's". The real responses are shown in (b)-(e), where the whole cell (black), R_1 (blue), and R_2-C (red) can be compared. Measuring the impedance of the sample as a function of frequency, we can plot the impedance in terms of the phase shift-ϕ (b) and magnitude-|Z| (c), as complementary Bode plots. The impedance response can be converted into a Nyquist plot (c), where the real (x-axis) and imaginary (y-axis) are labeled Z' and Z", respectively.

Fitting an equivalent circuit model to EIS results can be performed through different programs, including ZView (Scribner Associates), ZSimpWin (Echem Software), or LEVM (jrossmacdonald.com), where the equivalent circuit component values that provide the lowest sum of error between experimental data and the model are assumed to be the best fit. All of these fitting programs utilize complex non-linear least squares (CNLS) fitting based on the Marquardt-Levenberg algorithm.[51] Using ZView we can build an equivalent circuit model (the same as the dummy cell) and provide initial guesses for component values. For a simple circuit such as the dummy cell, initial guesses can be made based on the high and low frequency intercepts for R_1 and R_2, around 10 and 110, respectively, and the capacitance from peak frequency using the relationship $\omega_0 = 1/RC$ ($f_0 = 1/2\pi RC$). The initial guesses are crucial to finding the global instead of a local minimum. The equivalent circuit fit yields values of $R_1 = 9.987\Omega$, $R_2 =$

99.91Ω and C = 1.04×10^{-5}, which match the values provided for the individual components of 10Ω, 100Ω, and 100μF, respectively.

In electrode materials we need to consider other conducting species in addition to electrons and holes. For most high temperature oxygen conductors the majority charge carrier is oxygen vacancies, as is the case for LSM, LSCF, YSZ, and GDC. Using impedance spectroscopy we can probe how these charged species move across interfaces. The resistances and capacitances that describe interfaces are derivative of the governing reactions, and in a real system there are multiple interfaces that need to be considered. It is useful to note that certain capacitance or ω_0 values can help to determine what a particular interface is. For instance, in a solid oxide electrode/electrolyte cell operating at higher temperature, capacitance values smaller than 10^{-9}F are related to bulk diffusion, while values between 10^{-6}F and 10^{-9}F are associated with grain boundary conductivity. This is useful information when attempting to fit experimental data for SOFC materials. In addition to solid-state conduction, chemical interfaces, like gas/solid (O_2/electrode) are typically observed when studying electrode materials, and yield capacitance values closer to 10^{-3}F or greater. Eventually, at high enough capacitance (low frequency) it is also possible to observe gas-diffusion losses associated with the porosity of the sample. Using EIS it is possible to define the overall reaction process and determine the reaction steps quantitatively and qualitatively. More detailed analyses and typical equivalent circuits are provided throughout.

2.2 Gas Phase Oxygen Isotope Exchange

2.2.1 Isotope Exchange Theory

There are a number of methods aimed at probing the fundamental mechanisms of the ORR.[20,21,52,53] One particularly useful approach is through the use of isotopically labeled oxygen as a tracer. There are two main types of isotope exchange techniques, categorized by analysis of solid phase ^{18}O or gas phase ^{18}O. In the former, solid ^{18}O is quantified *ex-situ* using isotope exchange depth profiling (IEDP) with secondary ion mass spectrometry (SIMS) on dense bulk samples.[54–56] IEDP-SIMS provides a route to study the incorporation and diffusion properties of oxide materials that conduct O^{2-}. However, the *ex-situ* nature of IEDP-SIMS limits the ability of the technique to probe specific steps in the ORR, yielding a single surface exchange coefficient (k_{ex}). In contrast, gas phase analysis[53,57–61] the sample, typically in powder form, is subjected to a switch in the gas environment, from $^{16}O_2$ to $^{18}O_2$, creating a isotopic gradient between the gas and solid phase. Reaction rates are determined by tracking the change in $^{16}O_2$, $^{16}O^{18}O$ and $^{18}O_2$ signals in real time. Much of the literature covering gas phase isotopic analysis is centered on SSITKA, a well-developed technique for tracing oxygen exchange between various gas phase reactants, intermediates and products. Our approach is similar to SSITKA but isotope exchange on SOFC materials includes the exchange between gas and solid, as these materials actively incorporate oxygen into the lattice. In this case, the oxygen catalysts are actively involved in the reaction process and cannot be ignored. Gas phase oxygen isotope exchange can provide real-time information for both surface catalytic reactions and solid-state transport. Throughout this dissertation we focus on the development of gas phase oxygen isotope exchange experiments to probe oxygen exchange on oxygen conductors.

There are two main types of gas phase exchange experiments, isothermal isotope exchange (IIE) and temperature programmed exchange (TPX) that have been discussed thoroughly in previous works[62,60,58,57,63–65,61]. As indicated by the names, IIE is an isotopic exchange experiment that is performed under constant temperature conditions, while TPX involves a constant heating rate for the sample. TPX is able to rapidly determine levels of oxygen exchange across a wide range of temperatures. However, the technique is limited in its ability to determine fundamental rate constants, due mostly to changes in materials properties during heating. In contrast, IIE is performed at constant temperature, as well as under isobaric conditions. In this case, the sample, whose lattice is saturated with ^{16}O, is exposed to a complete switch of oxygen flowing through the system from $^{16}O_2$ to $^{18}O_2$, while all other conditions remain constant. If we consider ^{16}O and ^{18}O to be equivalent, we can model the system in IIE under equilibrium conditions. Here, we focus on the use of a modified IIE experiment, 1:1IIE, in which the inlet concentrations of $^{16}O_2$ and $^{18}O_2$ are equal. This provides some advantages, which will be discussed below.

2.2.2 Homogeneous and Heterogeneous Exchange

From a catalysis point of view, provided by the foundational work from Boreskov and others,[10,66,67] there are two main types of surface exchange for molecular oxygen: homogeneous exchange, only related to the dissociation/re-association reactions on the oxide surface; heterogeneous exchange, involving dissociation, incorporation of oxygen into the lattice and re-association of O_2 with an O-atom that originated from inside the oxide lattice.

In heterogeneous exchange, the exchange process involves the participation of lattice oxygen. Single heterogeneous exchange (R_1) is the exchange of one oxygen atom in O_2 with one lattice, or solid phase, oxygen, while double heterogeneous exchange (R_2) is the exchange of both atoms in O_2 with two atoms in the solid phase. The total rate of heterogeneous exchange (R_{ex}) is the sum of both single and double heterogeneous exchange:

$$R_{ex} = \frac{1}{2}R_1 + R_2 \qquad [2.5]$$

Two possible reaction paths for ^{16}O appearing in the gas phase are shown in Eqs. [2.6] and [2.7], and are referred to as R_1 and R_2, respectively.

$$^{18}O_2 + {}^{16}O_O \overset{R_1}{\rightarrow} {}^{16}O^{18}O + {}^{18}O_O \qquad [2.6]$$

$$^{18}O_2 + 2\ {}^{16}O_O \overset{R_2}{\rightarrow} {}^{16}O_2 + 2\ {}^{18}O_O \qquad [2.7]$$

where $^{16}O_O$ and $^{18}O_O$, represent ^{16}O and ^{18}O atoms occupying oxygen lattice sites, respectively. Our aim is to measure the rates of homogeneous and heterogeneous exchange on the surface.

2.2.3 1:1IIE

In 1:1IIE, a QMS measures the amount of each oxygen isotopologue in the reactor effluent. Isotopologue concentrations are calculated using the corresponding mass/charge (m/z) signals measured from the reactor effluent with a quadrupole mass spectrometer (QMS). The m/z ratios for $^{16}O_2$, $^{16}O^{18}O$, and $^{18}O_2$ are 32, 34 and 36, respectively. The oxygen in the reactor effluent is a sum of both exchanged and non-exchanged O_2:

$$[O_2]^{total} = [^{16}O_2]^{non-ex} + [^{16}O_2]^{ex} + [^{18}O_2]^{non-ex} + [^{18}O_2]^{ex} \qquad [2.8]$$

where $[^{16}O_2]^{non\text{-}ex}$ and $[^{18}O_2]^{non\text{-}ex}$ are concentrations of $^{16}O_2$ and $^{18}O_2$ that are not participating in exchange on the surface, and $[^{16}O_2]^{ex}$ and $[^{18}O_2]^{ex}$ are concentrations that are participating. The reaction products in isotope exchange are only related to those oxygen participating in the exchange reactions:

$$[{}^{16}O_2]^{ex} + [{}^{18}O_2]^{ex} = [{}^{16}O_2]^{ex-p} + [{}^{16}O{}^{18}O]^{ex-p} + [{}^{18}O_2]^{ex-p} \qquad [2.9]$$

where $[{}^{16}O_2]^{ex\text{-}p}$, $[{}^{16}O{}^{18}O]^{ex\text{-}p}$, and $[{}^{18}O_2]^{ex\text{-}p}$ are the possible reaction products after surface exchange.

In 1:1 IIE experiments, $[{}^{16}O_2]$ and $[{}^{18}O_2]$ are the combinations of both non-exchanged and exchanged flows, as shown in Eq. [2.9], but $[{}^{16}O{}^{18}O]$, the scrambled product, appears only after surface exchange occurs. Thus, the rate of $[{}^{16}O{}^{18}O]$ formation can be used to determine the apparent rate of dissociation occurring on the catalyst surface. As we be discussed again below.

Considering the system from the perspective of the solid-state electrochemist, where the elementary steps for oxygen exchange are dissociation adsorption and incorporation. The first elementary step, dissociative adsorption[11,59] is:

$$O_2 + * \leftrightarrow 2O_* \qquad [2.10]$$

where * denotes an available surface site, k_1 is the forward rate constant and k_{-1} is the backward rate constant. As we are probing an exchange reaction, where electrons are not supplied externally and there is no net change in oxidation state, we can ignore charge transfer. However, in SOFC cathodes where an external current is present, the oxygen dissociation reaction will involve a charge transfer step, where isotopically labeled O_2 molecules form surface ions. The possible forward reactions for dissociation are:

$${}^{16}O_2 + 2* \xrightarrow{k_1} 2\,{}^{16}O_* \qquad [2.11]$$

$${}^{18}O_2 + 2* \xrightarrow{k_1} 2\,{}^{18}O_* \qquad [2.12]$$

where O_* represents a charged oxygen on a surface site, assuming the charge transfer step occurs during dissociation, and *e* denotes an electron. After dissociative adsorption, atomic oxygen can recombine with another oxygen and desorb from the surface, giving the backward reactions:

$$ {}^{16}\mathrm{O}_* + {}^{18}\mathrm{O}_* \xrightarrow{k_{-1}} {}^{16}\mathrm{O}{}^{18}\mathrm{O} + 2* \qquad [2.13]$$

$$ 2{}^{16}\mathrm{O}_* \xrightarrow{k_{-1}} {}^{16}\mathrm{O}_2 + 2* \qquad [2.14]$$

$$ 2{}^{18}\mathrm{O}_* \xrightarrow{k_{-1}} {}^{18}\mathrm{O}_2 + 2* \qquad [2.15]$$

From The formation of ^{16}O^{18}O follows a series of surface reactions involving dissociative adsorption and desorption, and can be expressed as:

$$\frac{d[{}^{16}\mathrm{O}{}^{18}\mathrm{O}]^{ex-p}}{dt} = k_{-1}(S^2\Theta_*^2 k_1 \left([{}^{16}\mathrm{O}_2]^{ex}\right)^{1/2}\left([{}^{18}\mathrm{O}_2]^{ex}\right)^{1/2}) \qquad [2.16]$$

where *S* is the number of sites per unit surface area and Θ_* is the fraction of available surface sites. The forward and backward rates have temperature dependent activation and can be written as:

$$\frac{d[{}^{16}\mathrm{O}{}^{18}\mathrm{O}]^{ex-p}}{dt} = (S^2\Theta_*^2 \left([{}^{16}\mathrm{O}_2]^{ex}\right)^{1/2}\left([{}^{18}\mathrm{O}_2]^{ex}\right)^{1/2})A_{-1}A_1\exp(\frac{E_{-1}+E_1}{RT}) \qquad [2.17]$$

where A_1 and A_{-1} are the pre-exponential terms and E_1 and E_{-1} are the activation energies for the forward (dissociation) and backward (re-association) reactions, respectively. The apparent activation energy for the formation of ^{16}O^{18}O (E_d) is the sum of the energy for forward and backward reactions (E_1+E_{-1}), as O_2 needs to be dissociated and then be recombined back to the gas phase. The slope of the Arrhenius plot can give us information about the activation of the exchange process on cathodes, as shown in Eq. [2.17]. The overall exchange reaction can be expressed as:

$$2{}^{16}\mathrm{O}_2 + 2{}^{18}\mathrm{O}_2 \Leftrightarrow {}^{16}\mathrm{O}_2 + 2{}^{16}\mathrm{O}{}^{18}\mathrm{O} + {}^{18}\mathrm{O}_2 \qquad [2.18]$$

The final concentrations of $^{16}O_2$, $^{16}O^{18}O$, and $^{18}O_2$ at steady state can provide information about the catalytic activity of materials towards the dissociation of oxygen at different temperatures. Slow rates of heterogeneous exchange only delay the time for the isotopologue concentrations to reach a plateau.

During the switching process (not steady state) we also have to consider incorporation of oxygen into the lattice. After oxygen molecules are catalyzed on the material's surface, intermediate oxygen species can randomly exchange with another oxygen, which can be either a surface oxygen atom (homogeneous exchange) or a lattice oxygen atom (heterogeneous exchange). If lattice oxygen is involved in the exchange process, solid-state diffusion plays an important role in determining how fast ^{16}O can transport from the bulk of the material to the surface.

The surface exchange coefficient (k_{ex}) (cm/s) is used to quantitatively represent the level of heterogeneous exchange. The exchange flux (J) is proportional to the isotopic gradient at the gas-solid interface and scales by k_{ex}. Notice that as typically defined k_{ex} involves both dissociation and incorporation. Consider that the gas-solid surface exchange flux is equal to the ^{18}O flux that diffuses in the solid; the boundary condition for the gas-solid interface can be written as:[68]

$$J_{18O} = k_{ex}\left([^{18}O_g] - [^{18}O_s]\right) = -D\frac{\partial[^{18}O_s]}{\partial r} \qquad [2.19]$$

where $[^{18}O_g]$ and $[^{18}O_s]$ (#/cm^3) are the isotopic oxygen concentrations in gas and solid phases, respectively, and D (cm^2/s) is the diffusion coefficient. The general solution for diffusion into a sphere with surface exchange is:[68]

$$\frac{M(t)}{M_\infty} = 1 - \left[\sum_{m=0}^{\infty} \frac{6L^2 \exp(-\frac{\beta_n^2 Dt}{a^2})}{\beta_n^2(\beta_n^2 + L^2 - L)} \right] \qquad [2.20]$$

where t denotes the total exchange time and t_0 is the time at which ^{18}O is introduced into the system. M(t) is accumulated ^{18}O in the solid phase at time t and M(∞) is the total amount of ^{18}O exchanged into solid phase at t=∞. D (cm^2/s) is the diffusion coefficient. The radius of the spherical powder sample is a, and β_n are the roots, as shown in Eq. [2.21] and [2.22].

$$\beta_n \cot \beta_n + L - 1 = 0 \qquad [2.21]$$

$$L = a\frac{k_{ex}}{D} \qquad [2.22]$$

The characteristic length (L) is an important parameter that is used to determine the sensitivity of the characterization technique. Because k_{ex}/D is related to material properties, L values can be tuned by simply altering the sample size and/or geometry. Therefore, observed kinetic behaviors can be controlled to be sensitive to either surface exchange or bulk diffusion. The materials tested herein have particle sizes on the order of several hundred nanometers, making IIE an experiment mainly controlled by surface exchange.[58] Therefore the equation can be simplified for the fitting process to:

$$\frac{M(t)}{M_\infty} = 1 - \exp\left(-\frac{3k_{ex}t}{a}\right) \qquad [2.23]$$

2.2.4 Experimental Set-up

The experimental set up is shown in Figure 2.4, which can be divided into three different sections: gas source, isotopic switch, and micro-reactor. Mass flow controllers are used to control the oxygen and CO_2 concentrations. A water cooling system using thermoelectric, as shown in Figure 2.4, is used to control the temperature of a glass fritted impinger (bubbler) for introducing water into the system. The isobaric switch consists of a pneumatically actuated 6-port valve (VICI) that is capable of switching between 5% ^{16}O (balance He) and 5% ^{18}O (balance He +1000ppm Argon). A low concentration of argon (1000ppm) is used as a tracer to track the switch between $^{16}O_2$ and $^{18}O_2$. A custom built micro-reactor with an inner diameter of 4mm is used to support the powder sample. The total flow rate is fixed at 20 SCCM.

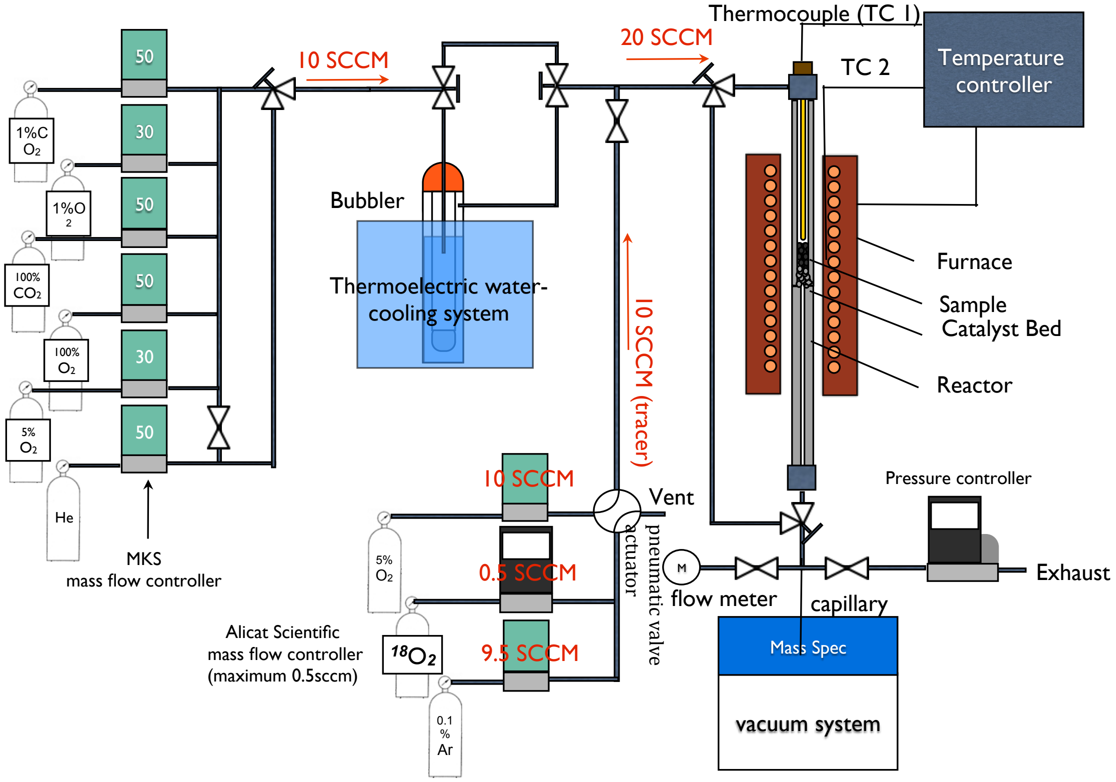

Figure 2.4: Experimental set-up for gas phase oxygen exchange experiments. The left side of the figure shows the gasses and concentrations that can be fed into the system. These gasses can be fed through a custom thermoelectrically cooled water bubble. The other half of the inlet is the ^{16}O-^{18}O switch controlled using a pneumatically actuated valve (VICI). The ^{18}O is connected to a special low-flow MFC (Alicat Scientific), and the He balance for the ^{18}O gas stream includes a 0.1% Ar tracer to detect the switch. The powder sample is loaded into quartz reactor and heated in a furnace controlled with an internal thermocouple (TC1). The gas effluent is measured using the downstream QMS that samples the exhaust with a capillary tube. A flow meter is used to measure the total flow rate and an additional pressure controller to maintain a constant pressure at the QMS inlet.

Before each isotope exchange experiment, the sample was pretreated at 800°C or

850°C in a normal $^{16}O_2$ isotope environment with PO_2=0.05 for 30 minutes to ensure that the powder surface is clean and completely saturated with ^{16}O. After the pretreatment, the sample was brought to the temperature of interest and equilibrated in $^{16}O_2$ with PO_2=0.05. In a separate line isotopically labeled $^{18}O_2$ (Sigma-Aldrich; 95% pure), with a PO_2=0.025, and 1000ppm of Ar (Airgas), used as an inert tracer, was flowed. Then, using a pneumatically actuated valve, half of the $^{16}O_2$ flowing through the powder was switched to the $^{18}O_2$ flow with 1000ppm Ar tracer creating a 1:1 ratio of ^{16}O: ^{18}O. The evolution of oxygen species, $^{16}O_2$, $^{16}O^{18}O$, and $^{18}O_2$ were then recorded using a quadrupole mass spectrometer (QMS). The $^{16}O^{18}O$ production rate is normalized to the total surface area of testing powder, 0.1 m^2. Based on the length of powder bed (1~2mm) and the theoretical density of powder, the residence time of the gas through the powder bed is around 10^{-6}~10^{-7} seconds. Therefore, a differential plug flow reactor model is assumed.

Chapter 3: Degradation Mechanisms in LSCF-GDC Composite Cathodes

3.1 Introduction

Solid oxide fuel cells (SOFCs) are a promising technology for the generation of electricity through the electrochemical oxidation of fuels[1,3,4]. There are a number of performance hurdles for the successful implementation of SOFCs, most notably high polarization losses associated with the oxygen reduction reaction (ORR) that occurs at the cathode and degradation of cathode performance under operating conditions. Further, cathode polarization losses and degradation can be exacerbated by the presence of gasses other than O_2 in the cathode feed stream, which is typically supplied from ambient air. Of the different components that constitute ambient air, H_2O (humidity) and CO_2 are the greatest concern for cathode stability [30,33,35–39,69–73]. Concentrations of H_2O and CO_2 vary across the world depending on climate, weather, and other factors such as emissions from hydrocarbon fuel consumption. Here we have explored the effects of H_2O and CO_2 on $La_{0.6}Sr_{0.4}Co_{0.2}Fe_{0.8}O_{3-\delta}$ - $Ce_{0.90}Gd_{0.10}O_{1.95}$ (LSCF-GDC) composite cathodes. LSCF is a mixed ionic-electronic conductor (MIEC) that has promise as an SOFC cathode for cells operating at reduced temperatures (<750°C). The high performance of LSCF is brought about by a number of different factors including its catalytic activity toward the ORR [12,69] and its high oxygen ion conductivity (~0.2 S/cm at 800°C)[17]. In comparison to $(La_{0.8}Sr_{0.2})_{0.95}MnO_{3-\delta}$ (LSM), the staple SOFC cathode material, LSCF has both higher ionic and electronic conductivity as well as O_2 reduction kinetics [69]. Crucially, the ability of LSCF to conduct oxygen ions extends the active region of the cathode beyond the triple phase boundary (TPB), a significant drawback limiting the performance of LSM[15]. Unfortunately, the high performance resulting from the greater oxygen non-stoichiometry of LSCF brings with it a number of obstacles, namely the instability of the material under operating conditions[33,72].

Cathode performance is controlled by a number of different factors that are related to intrinsic material properties and cathode microstructure: catalytic activity toward the ORR, electronic conductivity, ionic conductivity, gas phase conductivity, two-phase boundary area, triple phase boundary length, etc. Degradation of LSCF-GDC performance by H_2O and CO_2 must therefore cause changes in one or more of these factors. There have been a number of reports in literature that explore the degradation of LSCF and similar perovskites, including the effects of contaminants such as H_2O and CO_2. In general, one of the most common degradation mechanisms discussed for LSCF is Sr segregation on the surface of the material, and has been widely discussed in literature [5,7,33,38,39,74,75]. Additionally, it has been shown that the presence of CO_2 can enhance the kinetics of Sr segregation through the formation of $SrCO_3$ [39]. Benson et al.[33] investigated the effects of H_2O and CO_2 on surface exchange through isotope exchange depth profiling (IEDP), and found that CO_2 improves oxygen exchange at annealing temperatures above 750°C, while H_2O has no effect. Interestingly, samples annealed in both CO_2 and H_2O at lower temperatures showed changes in oxygen exchange. In addition, Zhao et al.[38] describe operation of cells with LSCF cathodes under $O_2/CO_2/H_2O$ gas environments to be stable at temperatures above 680°C. Similarly, Hayd et al.[70] reported that for $La_{0.6}Sr_{0.4}CoO_{3-\delta}$ (LSC), CO_2 leads to reversible cathode poisoning at temperatures above 500°C and PO_2 dependent reversibility below 500°C, while H_2O on

LSC affects only the ionic diffusion of oxygen. The literature shows that CO_2 and H_2O do affect cathode performance and are clearly determined by temperature, PO_2, and reaction kinetics. This paper aims to elucidate the temperature dependencies of LSCF-contaminant interactions, and highlight the differences between CO_2 and H_2O reaction mechanisms.

Our previously reported gas phase oxygen isotope exchange data indicated a strong interaction between water and LSCF powders at temperatures close to 450°C, with levels of exchange decreasing as the temperature was increased up to 800°C[69]. Additionally, other results showed an increasing interaction between LSCF and CO_2 as the temperature was increased from 50°C to 800°C[76]. We believe that the temperature dependent changes in exchange rates with and without the presence of contaminants are related to different reaction mechanisms controlling the overall oxygen exchange reaction. Unfortunately, gas phase isotope exchange is performed with experimental parameters that are not representative of typical SOFC cathode operating conditions. The factors governing cathode performance include not only the intrinsic material properties of LSCF, but also the arrangement of the cathode microstructure, which is absent during gas phase isotope exchange experiments. In this study electrochemical impedance spectroscopy was used to investigate LSCF-contaminant interactions with realistic working conditions. Electrochemical impedance spectroscopy (EIS) is a powerful tool that allows us to identify changes in conductivity for the reaction steps comprising the overall ORR. EIS can provide information about bulk, interfacial, and chemical properties of the material[47,77–79]. We have developed a strategy for identifying the steps in the ORR that contribute to the overall impedance spectra, and how each contribution changes as a function of operating conditions and aging time.

In this investigation we used EIS to determine the effects of the common cathode contaminants, water and CO_2, on the ORR kinetics and material stability of LSCF-GDC (50-50 % by weight) composite cathodes. Three-electrode measurements were conducted on LSCF-GDC symmetrical cells aged within a controlled environment. The changes in cells during aging were monitored by EIS *in-situ*. Cells were aged in H_2O and CO_2 environments between 450°C and 750°C and impedance spectra were recorded as a function of aging time. In addition, impedance spectra were gathered under a wide range of conditions to determine the dependence of the various contributions to the overall impedance as a function of temperature, PO_2, and PCO_2. The results are then used to determine the different reaction/degradation mechanisms on LSCF with the presence of H_2O or CO_2 in different temperature regions for both short-term and long-term exposures.

3.2 Experimental

Symmetrical cells consisting of an LSCF-GDC working electrode, GDC electrolyte, and LSCF-GDC counter electrode were fabricated using standard procedures. GDC powder (Fuel Cell Materials) was uni-axially pressed in a 10mm diameter die and sintered at 1450°C for 6 hours. The sintered pellets were then polished to a sintered thickness of 5mm, and a thin groove cut equidistant from the top and bottom of the pellet for placement of a Pt reference electrode. Subsequently, LSCF-GDC composite cathode paste (Fuel Cell Materials) was printed on the top and bottom of the GDC pellets and then sintered at 950°C for 2 hours. Commercially available electrolyte powder and cathode paste were chosen for material consistency and as representative of the current status of LSCF and GDC. The thickness of the composite cathode was controlled to be around 25 μm. Finally, a thin layer of Au paste was painted on both the working and counter electrodes and dried at room temperature for 1 hour. The cells were then loaded into a custom built single-environment reactor and heated to 875°C for 15 minutes to finish drying the Au paste before being cooled to the temperature of interest to begin testing.

A schematic showing the cell geometry for LSCF-GDC/GDC/LSCF-GDC symmetrical cells is shown in Figure 3.1 (a). The schematic drawing of reactor set up is shown in Figure 3.1 (a). The reactor was made with alumina tubes to avoid any cross-contaminations, such as silica, with a closed environment, enabling the control of gas concentrations. A thermocouple was placed inside the reactor, near the cell to ensure accurate temperature measurements. Gas flow rates and mixtures were controlled using a set of mass flow controllers (MKS). EIS measurements were performed using a 1400 Frequency Response Analyzer and a 1470 Cell Test System (Solartron Analytical). During aging tests, cells were held at a constant temperature, in a constant gas environment, and EIS spectra measured throughout the aging process. Aging studies were performed at an O_2 concentration of air with either 5% CO_2, controlled by a mass flow controller, or 3% H_2O, introduced through a glass impinger at room temperature. Cells aged at 750°C were aged for 500 hours, while cells aged at 450°C were cooled after 350 hours. All samples were aged and EIS spectra measured, under open circuit voltage. Post-analysis X-ray diffraction of cells was performed using a Bruker D8 Advance, Cu K_α.

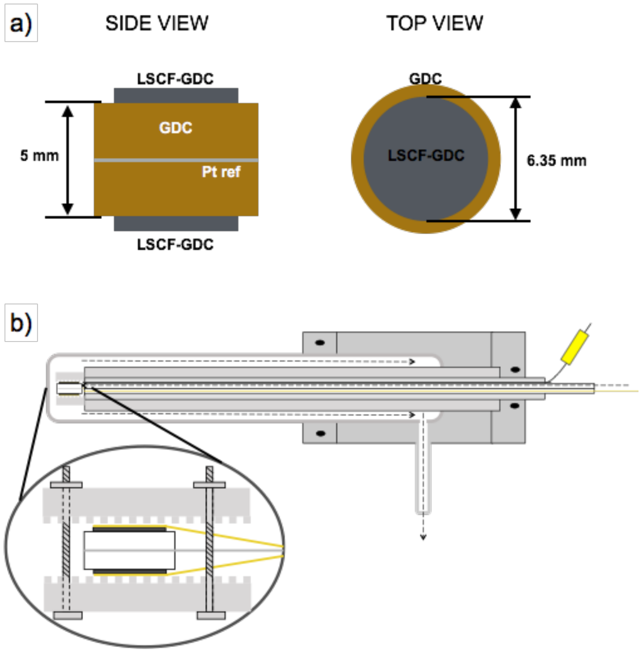

Figure 3.1: (a) A drawing of an LSCF-GDC/GDC/LSCF-GDC three-electrode test cell, showing configuration and geometric dimensions. (b) A schematic of the custom-built reactor for single-environment three-electrode cell testing.

3.3 Results and Discussion

A common degradation mechanism for LSCF is the formation of secondary phases, namely SrO. This is especially true for LSCF aged in the presence of CO_2, as it is believed that strontium carbonate ($SrCO_3$) is an effective intermediate for SrO formation. Figure 3.2 (a) shows the X-ray diffraction (XRD) pattern for an unaged sample, with diffraction peaks labeled for LSCF, GDC and Au (contact paste). Figure 3.2 (b)-(e) shows the XRD results for cells aged in synthetic air with the presence of 3% H_2O (b) and (c) and a 5% CO_2 (d) and (e), at 450°C (b) and (d) and 750°C (c) and (e). The presence of LSCF, GDC, and Au is seen in the diffraction pattern, but no secondary phases are discernable. It is possible that the resolution of XRD is such that a small amount of surface segregates will not be detected. While the total amount of segregation may be small compared to the bulk of the cathode material, degradation of the surface can have significant effects on the performance of the material. EIS can give insight into the surface properties of LSCF-GDC cathodes that *ex-situ* post-analysis techniques may not be able to provide.

EIS was used extensively in this study to investigate the effects of H_2O and CO_2 on LSCF-GDC composite cathodes. The power of EIS comes from its ability to observe the entire range of processes occurring in an electrochemical system. Within the scope of this work a process will be defined as a chemical or physical phenomena that contributes to the overall cathode reaction. The power of EIS can also be seen as a shortcoming, as simultaneously observing all of the processes that govern the cathode reaction can cause difficulty in attributing different portions of the spectra to specific processes. Further, the ability to observe, and the response provided by, any individual process, depends significantly on sample composition, fabrication methods, and testing conditions. Acknowledging the limitations of impedance spectroscopy, an attempt is made throughout this paper to provide a level of analysis that is quantitative and sufficiently descriptive, while avoiding claims that are overreaching and potentially misleading.

De-convolution and quantification of EIS data is performed through equivalent circuit modeling. Figure 3.3 (a) shows a modified Voigt circuit that is commonly used to model the impedance of SOFC cathode materials[43,45,49]. The component L represents inductance, commonly attributed to lead wires. The second component, R_S, is a resistance that describes the high frequency intercept of the impedance spectra and stems in large part from the conductivity of the electrolyte material. Finally, there are a number of individual parallel resistive-capacitive components that describe the physical and chemical phenomenon that make up the overall cathode reaction. In a Nyquist plot, a parallel resistor-capacitor circuit appears as a semi-circle, or what is commonly referred to as an arc. Here we use a variation of the 'perfect' capacitor known as a constant phase element (CPE) to extract an average capacitance for a process that cannot be described by a single capacitance value. A CPE is often categorized as a distributed circuit element that varies in its capacitance value as a function of frequency, and has been described in depth elsewhere[80].

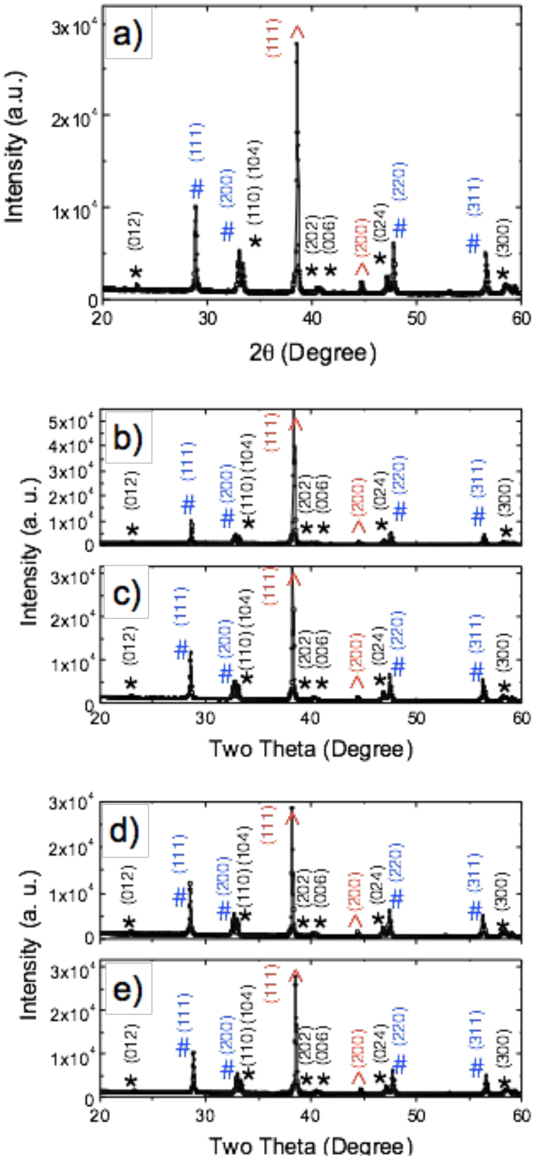

Figure 3.2: XRD results for an un-aged LSCF-GDC cell (a), cells aged in air + 3% H_2O at 450°C (b) 750°C (c), and cells aged in air + 5% CO_2 at 450°C (d) 750°C (e). Diffraction peaks corresponding to diffraction planes of LSCF, GDC and Au (from current collecting contact paste) are labeled using (#), (*) and (^) respectively. Despite long-term (250+ hours) of exposure to 3% H_2O or 5% CO_2 there are no discernable secondary phases, such as SrO or $SrCO_3$.

The Voigt circuit model is flexible and allows for the number of arcs, *n*, to be increased or decreased to best describe the system in question. Figure 3.3 (b) is a representative Nyquist plot for an LSCF-GDC composite cathode cell that was tested at 450°C in synthetic air (21% O_2, 79% N_2) with a 200 SCCM gas flow rate. The frequency decades are shown as solid points and labeled accordingly. An error-minimization fit obtained through ZSimpWin (Echem Software) using the equivalent circuit shown in Figure 3.3 (a), with n=2, yielding two R-CPE components, is shown as a solid line in Figure 3.3 (a). In the Nyquist plot we can see an inductive tail pulling the high frequency data below zero on the y-axis; the contribution of the electrolyte is shown as R_S, at the high frequency intercept, and the two arcs, one high frequency and one low frequency, are labeled R_{HF} and R_{LF} respectively.

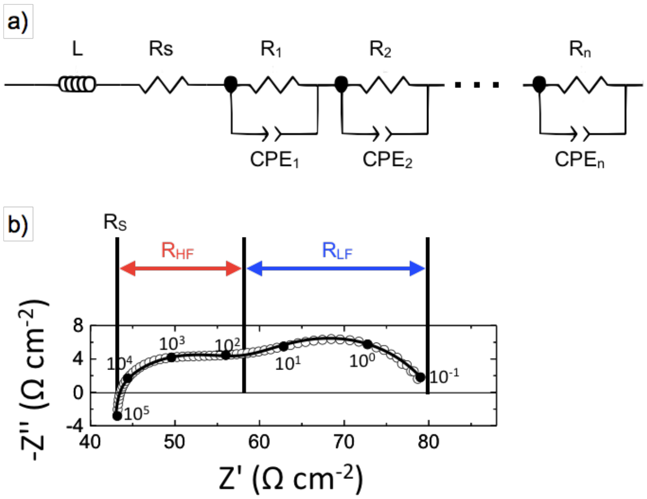

Figure 3.3: (a) An altered Voigt-circuit used to fit the impedance spectroscopy data obtained during cell testing. The circuit is composed of an inductor (L), attributed to the inductance from testing leads/wires, a resistor (R_S), representing the ionic resistance of the electrolyte, and *n* resistor-constant phase element (R-CPE) parallel circuits, representing the physical and chemical phenomena that make up the overall cathode reaction. (b) A Nyquist plot of a representative impedance spectrum for an LSCF-GDC cell (open symbols) with labeled frequency decades (closed symbols). The best fit of the spectrum is shown as a solid line, with labels depicting approximations of the resistive components from the equivalent circuit.

Figure 3.4 shows Nyquist plots for EIS measurements made at (a) 450°C, (b) 550°C, (c) 650°C, (d) 750°C, and (e) 800°C. At each temperature, the LSCF-GDC cells were exposed to both air (black circles) and air with 3% water (blue squares). Additionally the decade points are shown as solid symbols. Qualitatively, we can observe a number of different things from the impedance spectra shown in Figure 3.4. Looking at the evolution of the impedance spectra as a function of temperature we can identify changes that occur in the various arcs. At 450°C there appear to be at least two distinct arcs, one with a peak frequency of 1kHz and a second lower frequency arc with a peak near 3Hz. As the temperature of the cell is increased 800°C, we can see that the sizes of both the high and low frequency arcs are decreasing. The low frequency arc, with a characteristic frequency of 3Hz, in comparison to the high frequency arc, appears to be decreasing more rapidly. There is a shift to higher characteristic frequencies for both R_{LF} and R_{HF}, resulting from the thermally activated gas-solid reactions. In contrast, we can see that the high-frequency arc is unchanged with the presence of water. Comparing the two spectra as a function of increasing temperature, in Figure 3.4 (b)-(e), the change in the impedance spectra is smaller. At 550°C (Figure 3.4 (b)) and 650°C (Figure 3.4 (c)) the increase in R_{LF} is still readily apparent. However, at 750°C and 800°C (Figure 3.4 (d) and (e)) there is no apparent change in either R_{LF} or R_{HF} with the presence of H_2O, suggesting that the reaction kinetics on LSCF-GDC is affected by H_2O differently at different temperatures.

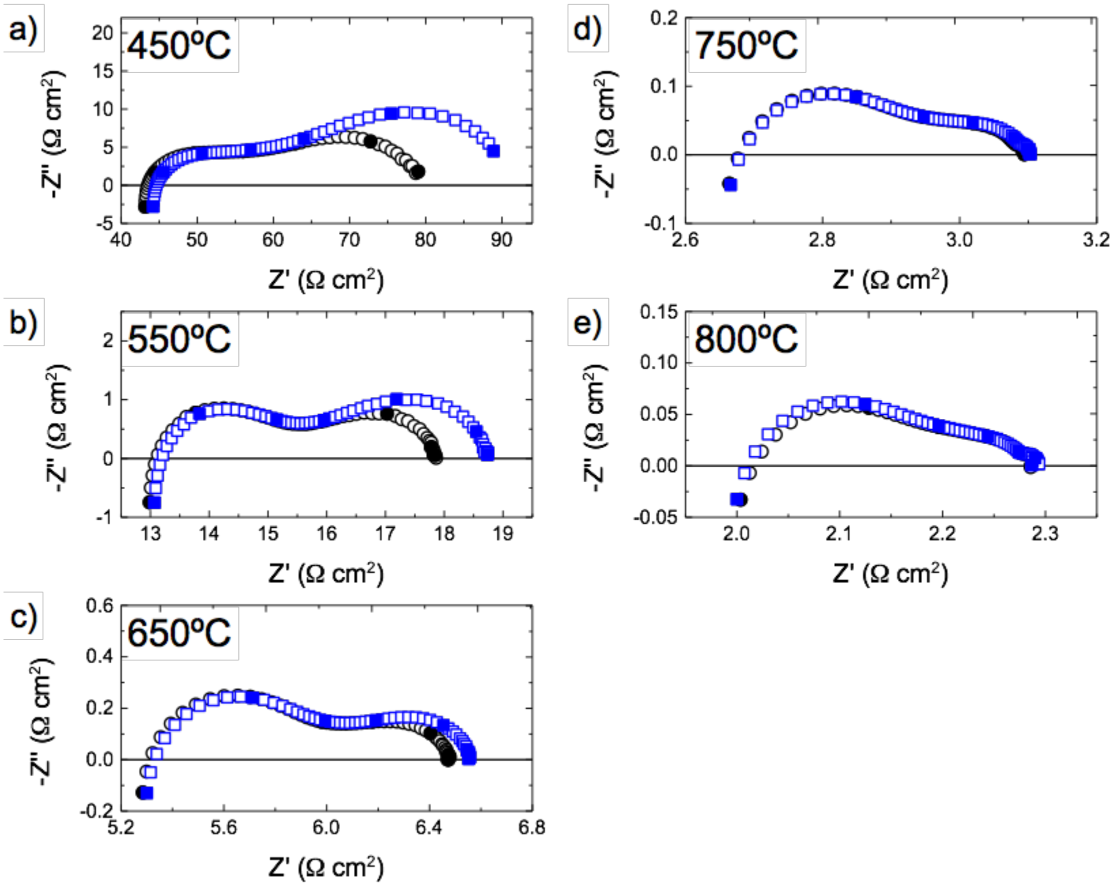

Figure 3.4: Impedance spectra for an LSCF-GDC cell tested in synthetic air (black circles) and synthetic air + 3% H_2O (blue squares) at temperatures ranging from 450°C to 800°C. Frequency decades (100kHz to 0.1Hz) are not directly labeled but are shown as closed symbols. The presence of 3% H_2O appears to increase the size of the low frequency arc for (a) 450°C, (b) 550°C, and (c) 650°C, but shows almost no effect at temperatures of (d) 750°C and (e) 800°C.

Figure 3.5 (a)-(b) are Arrhenius plots of R_S and area specific resistance (ASR) of R_{LF} with respect to reciprocal temperature. In Figure 3.5 (a) one can see the Arrhenius dependence for the ohmic portion of the measured impedance spectra with (closed symbol) or without (open symbol) the presence of H_2O. The conductivity clearly increases as a function of temperature, with an activation energy of ~66kJ/mol. This is in close agreement with literature values for the Arrhenius dependence of GDC electrolyte[81,82]. The presence of water does not affect the bulk conductivity of GDC. Further, we can see from Figure 3.5 (b) how the resistances of the low frequency arc, R_{LF}, change with temperature with (blue circles) and without (black squares) the presence of water. The increase in R_{LF} is more prevalent at 450°C and 550°C than at higher temperatures, resulting in an increase of the apparent activation energy of R_{LF} for this cell from 97kJ/mol to 111kJ/mol. The increase in activation energy for R_{LF} when water is present is likely caused by H_2O blocking oxygen exchange sites, impeding the overall ORR. As temperature increases, H_2O adsorption decreases, lessening the impact of water on the ORR.

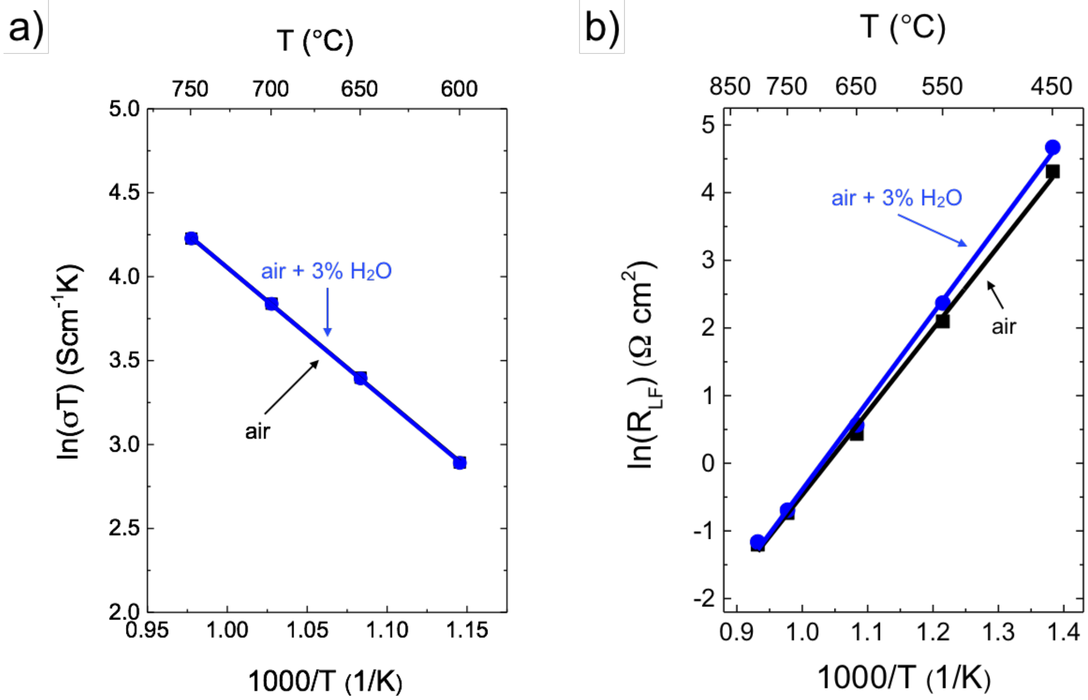

Figure 3.5: An Arrhenius plot of the temperature dependence of R_{LF} for an LSCF-GDC composite cathode in synthetic air (black squares) and synthetic air + 3% H_2O (blue circles). The best fit lines depict a clear increase in the temperature dependence of the process(-es) contributing to the low-frequency portion of the impedance spectrum with the presence of 3% H_2O. The values for R_{LF} were extracted from the impedance spectra shown in Figure 3.4 (a)-(e) using the equivalent circuit from Figure 3.3 (a).

Long-term effects of water were investigated at two operating temperatures, 750°C and 450°C, where we see clear differences in the interaction between water and LSCF-GDC cathodes. Figure 3.6 (a) shows the percent change in ASR for R_S, R_{HF} and R_{LF} as a function of time during exposure of LSCF-GDC to air +3% water for 500 hours at 750°C. From this figure we can see the changes occurring in each portion of the impedance spectrum, and then associate these changes with a degradation mechanism. First, we can see a clear increase in R_S during the aging process. This change occurs more rapidly in the beginning and slows down as the cell approaches 500 hours of exposure. Next, we can see a decrease in the size of the high frequency arc that appears to be almost opposite the change in R_S. Finally, there is a relatively small amount of change occurring in R_{LF}, which appears to first increase, but fluctuates significantly as a function of time. The trends shown in Figure 3.6 (a) indicate that the likely mechanism occurring is sintering. This sintering process however, may be accelerated by the presence of water in the gas stream.

A separate sample was also aged at 450°C in air + 3% water to study the effects of water at different temperatures. To best present the effects of H_2O at this temperature, the impedance spectra at selected aging-time intervals are shown in Figure 3.6 (b) as Nyquist plots. The initial measurement in air, before exposure to water, is shown as black squares in Figure 3.6 (b). This is a typical impedance plot in air at 450°C, as shown previously in Figure 3.4 (a). The impedance spectra shown as blue squares, is of the LSCF-GDC cathode after aging at 450°C for 250 hours in air + 3% water. Comparing the spectra shown as the black squares to that shown as blue squares, we can see a significant increase in the overall polarization. The main contribution is from R_{LF}, and almost no change in R_{HF}. This is very similar to what we saw for non-aged samples at 450°C. Subsequently, after aging the LSCF-GDC sample for 250 hours with the presence of 3% water, a switch was turned to bypass the water bubbler, effectively removing water from the system. Measurements made at 5 (pink circles), 10 (green triangles) and 15 (purple inverted triangles) hours are also shown in Figure 3.6 (b). From these plots we can see that there is a relatively quick decrease in the magnitude of R_{LF}, eventually reaching its original shape. As such, it is apparent that the effect of water on LSCF-GDC cells at 450°C is one that is reversible.

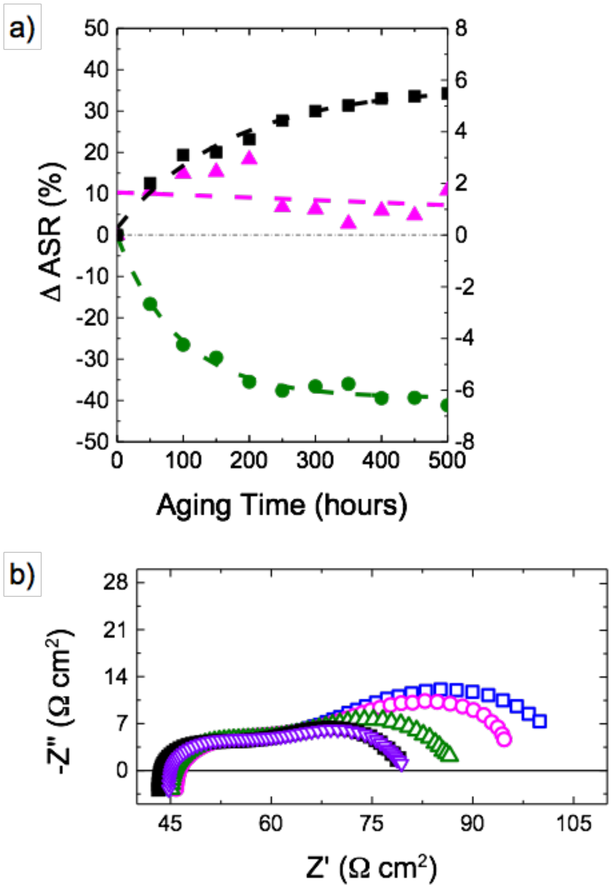

Figure 3.6: (a) A plot of the percent change in values of R_S (black squares), R_{HF} (green circles), and R_{LF} (pink triangles) as a function of aging time at 750°C in 3% H_2O. Dashed lines are used to show the general trend in each component. Values for R_S, R_{HF}, and R_{LF} are extracted by fitting the impedance spectra with the equivalent circuit shown in Figure 3.3 (a) at selected times throughout aging. (b) Nyquist plots for aging in 3% H_2O at 450°C for 250+ hours. The various spectra correspond to impedance measurements made before exposure to water (closed black squares), after ~280 hours of exposure to air + 3% H_2O (open blue squares) and at 2 (open pink circles), 5 (open green triangles), and 25 (open purple inverted-triangles) hours after exposure to dry air. The Nyquist plots in (b) show the reversibility of exposure to 3% H_2O.

To directly compare the water and CO_2 effects on LSCF, experiments performed under the presence of air and water were replicated with air + CO_2. Figure 3.7 (a)-(d) shows Nyquist plots for LSCF-GDC samples tested in air (black circles) and air + 5% CO_2 (red squares) between 450°C and 800°C. Unlike water, the effect of CO_2 is apparent across the entire temperature range, increasing the size of the R_{LF}. The relative increase in R_{LF} is better exemplified in Figure 3.8, showing the Arrhenius dependence of R_{LF} with and without 5% CO_2 in air. From Figure 3.8 we can see that there is an increase in R_{LF} with the presence of CO_2 but the slope of the line under both conditions is the same. The results brought out an interesting point that CO_2 effect on LSCF doesn't have temperature dependence. The high temperature neither promotes the CO_2 reaction nor the decrease of overall CO_2 adsorption.

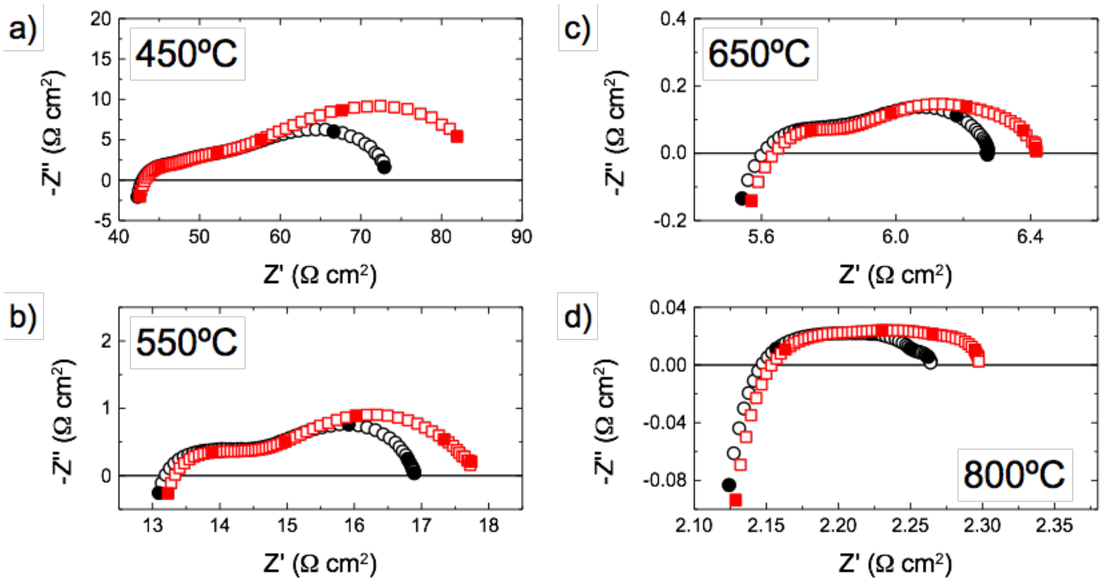

Figure 3.7: Impedance spectra for an LSCF-GDC cell tested in synthetic air (black circles) and synthetic air + 5% CO_2 (red squares) at temperatures ranging from 450°C to 800°C. Frequency decades (100kHz to 0.1Hz) are not directly labeled but are shown as closed symbols. The presence of 5% CO_2 appears to increase the size of the low frequency arc across the entire temperature range studied, unlike the effect of 3% H_2O shown in Figure 3.4.

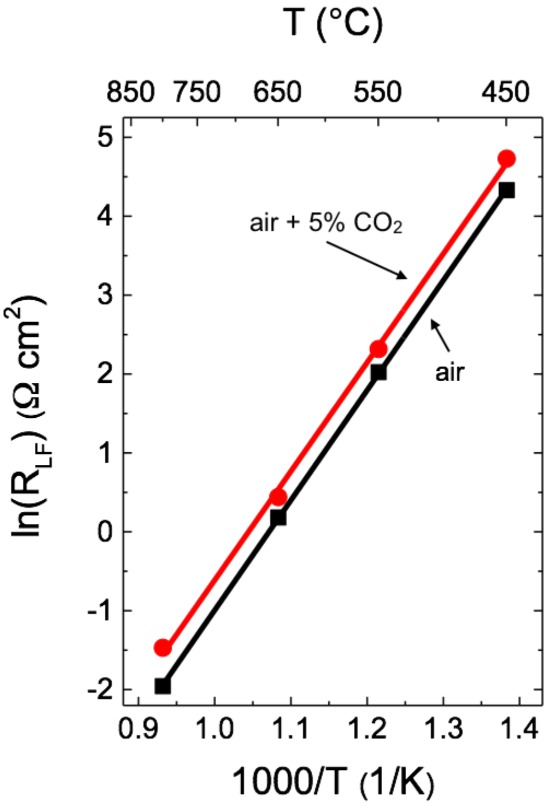

Figure 3.8: An Arrhenius plot of the temperature dependence of R_{LF} for an LSCF-GDC composite cathode in air (black squares) and air + 5% CO_2 (red circles). The best-fit lines show that the temperature dependence of R_{LF} is the same for both air and air + 5% CO_2; there is an increase in the resistance at each temperature, but no change in the slope of the line. The values for R_{LF} were extracted from the impedance spectra shown in Figure 3.7 (a)-(d) using the equivalent circuit from Figure 3.3 (a).

In addition to studying the temperature dependence of CO_2 exposure, we also investigated the PCO_2 dependence to clarify how O_2 and CO_2 molecules act on the surface at different temperatures. Figure 3.9 (a) is Nyquist plots showing the PCO_2 dependence of LSCF-GDC at 450°C. Under increasing PCO_2 we observe a corresponding increase in the size of the low frequency arc. In all but the case for 100% CO_2, in which we see a Warburg at low frequency, there is still 21% oxygen being flowing to the sample, in addition to the labeled concentration of CO_2. Figure 3.9 (b) shows the PCO_2 dependence at 800°C using the same concentrations of CO_2 as those investigated at 450°C. In this figure there appears to be little to no change in the size of any of the arcs as a function of CO_2 concentration. The only significant change is observed when 100% of the gas flowing to the system is CO_2, e.g. no oxygen. From Figure 3.9 (a) and (b) we can see that the dependence of R_{LF} on CO_2 concentration changes significantly between low and high temperature operation, despite an effect existing across the entire temperature range studied.

Long-term aging experiments for LSCF-GDC samples in air + 5% CO_2 were conducted at 750°C and 450°C. Figure 3.10 (a) shows the percent change in ASR as a function of aging time at 750°C in air with 5% CO_2. We observe a similar trend in the sample exposed to 5% CO_2 to that which was exposed to 3% H_2O: a relative increase in R_S and a relative decrease in R_{HF}. Additionally, we observe some small fluctuations in R_{LF} during the aging process. The overall changes in R_S and R_{HF} after 500 hours of aging are small as compared to Figure 3.6 (a). This may indicate that sintering of the cell occurs more readily under the presence of water as opposed to CO_2. LSCF-GDC samples aged in air + 5%CO_2 at 450°C are shown using Nyquist plots in Figure 3.10 (b). The initial impedance spectrum, measured in air without CO_2 is shown as the sold black squares. The impedance spectrum after 250 hours of exposure to 5% CO_2 is shown as the open blue squares. As expected, we see a significant increase in the size of the low frequency arc after being exposed to CO_2. However, this increase was not immediate, like that shown in Figure 3.7 (a), it increased as a function of aging time. Impedance spectra after stopping the flow of CO_2 (air only) are also shown in Figure 3.10 (b), for 5 (pink circles), 10 (green triangles) and 15 (purple inverted triangles) hours of exposure to only oxygen and nitrogen.

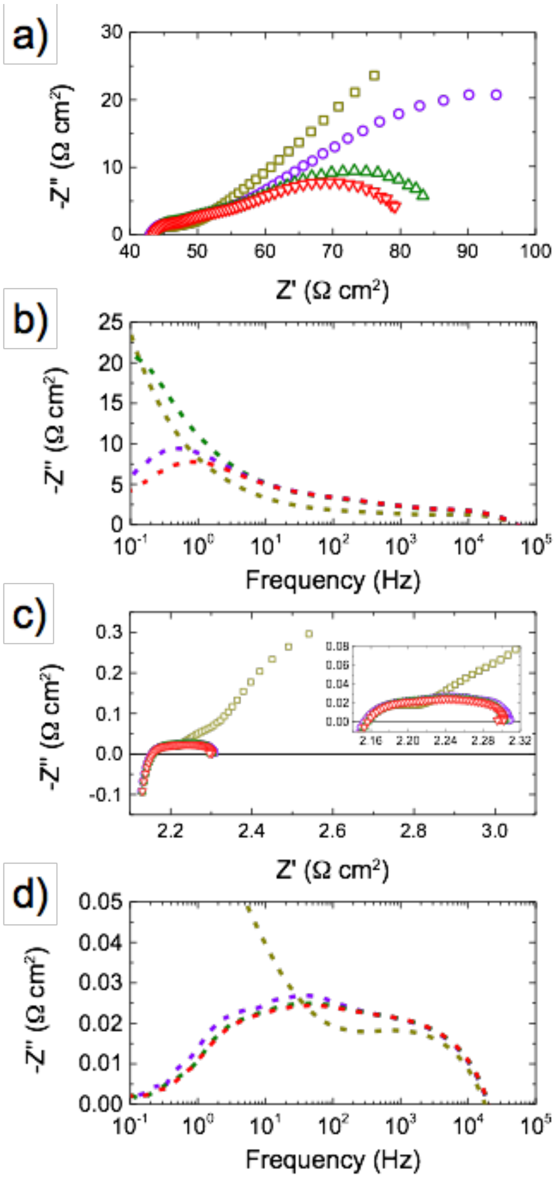

Figure 3.9: The *P*CO_2 dependence of LSCF-GDC cells at 450°C (a)(b) and 800°C (c)(d) presented as both Nyquist (a)(c) and Bode (b)(d) plots. The concentration of CO_2 was controlled through the fraction of CO_2 gas flowing to the reactor; 100%, 50%, 10%, and 5% CO_2 are shown as gold squares, purple circles, green triangles and red inverted triangles, respectively, in (a) and (c) and the same colors for the dashed lines in (b) and (d). At 450°C there is a clear dependence of R_{LF} on the concentration of CO_2, while at 800°C there appears to be no *P*CO_2 dependence. For 50%, 10% and 5% CO_2 the fraction of O_2 in the gas stream is 20%.

The removal of CO_2 from the gas stream rapidly decreases the size of R_{LF} after just 5 hours, and the trend continues after 10 hours as well. However, R_{LF} does not return to its original value in air after 15 hours without any CO_2 flowing to the cell, and the impedance spectrum at 10 hours of air is very similar to that of 15 hours in air. The total change in R_{LF} after aging in 5% CO_2 for 250 hours is close to 60%, even after stopping the flow of CO_2 to the cell. Unlike 3% H_2O, it appears that the effect of CO_2 at 450°C is irreversible.

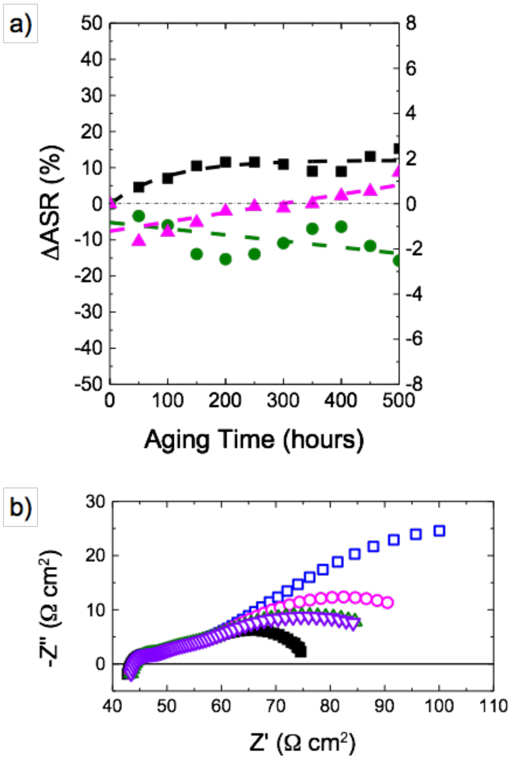

Figure 3.10: (a) A plot of the percent change in values of RS (black squares), R_{HF} (green circles), and R_{LF} (pink triangles) as a function of aging time at 750°C in 5% CO_2. Dashed lines are used to show the general trend in each component. Values for R_S, R_{HF}, and R_{LF} are extracted by fitting the impedance spectra with the equivalent circuit shown in Figure 3.3 (a) at selected times throughout aging. (b) Nyquist plots for aging in 5% CO_2 at 450°C for 500+ hours. The various spectra correspond to impedance measurements made before exposure to water (closed black squares), after ~500 hours of exposure to air + 5% CO_2 (open blue squares) and at 1 (open pink circles), 8 (open green triangles), and 9 (open purple inverted-triangles) hours after exposure to air without CO_2. Unlike the rapid reversibility seen for water exposure at 450°C in Figure 3.6 (b), after 9 hours without the presence of 5% CO_2 the size of R_{LF} is still ~60% larger than it's initial value.

It is advantageous to look at the differences between how H_2O and CO_2 interact with LSCF-GDC cathodes in order to gain a better understanding of each contaminant separately. Table I summarizes the effects seen under the different testing conditions during both short and long-term exposure to H_2O and CO_2. For H_2O we observed that the

Table I: Summary of H_2O and CO_2 effects on LSCF-GDC composite cathodes as a function of testing condition.

		Low Temp.	High Temp.
H_2O	Short-term	Increase in R_{LF}, reversible	No observable change
	Long-term	Rapid increase in R_{LF}, reversible after exposure to air	Increase in R_S, decrease in R_{HF}
CO_2	Short-term	Increase in R_{LF}, partially reversible	Increase in R_{LF}, reversible
	Long-term	Gradual increase in R_{LF}, not reversible	Increase in R_S, decrease in R_{HF}

short-term, or the impact on surface reaction kinetics, is more significant at low temperature than it was at higher temperatures. At 450°C we see an increase in the size of R_{LF} with the presence of 3% H_2O, and that the increase becomes less apparent at higher temperatures, until it disappears at 800°C. From these results we may assume that the H_2O readily adsorbs on the surface of LSCF blocking sites at which the ORR occurs. As the temperature increases, the adsorption of H_2O on LSCF decreases, making it more favorable for oxygen to adsorb and dissociate on the cathode. In terms of the reversibility after long term aging at 450°C, we may conclude that although H_2O adsorbs on the surface, blocking oxygen adsorption sites, it does not cause any irreversible degradation. In contrast, aging at 750°C does show change in the various components of the impedance spectrum. Previously, we described these changes as likely being caused by sintering. We see similar trends in R_S, R_{HF} and R_{LF} for the sample aged with CO_2 at 750°C, just less overall change occurring. This supports the theory that H_2O intensifies sintering at high temperatures. Despite the similarities between CO_2 and H_2O exposure in long-term degradation at 750°C for LSCF-GDC cathodes, we see a significant difference in the both the short-term effect, as well as low-temperature aging at 450°C. For the sample exposed to 5% CO_2 we see that the effect of CO_2 is apparent between 450°C and 800°C and is best presented in the Arrhenius dependence in Figure 3.8. In this figure, we see a shift upward, showing the increase in R_{LF} with the presence of CO_2 but no change in the activation energy. This means that CO_2 occupies a number of surface sites at both 450°C and 800°C, unlike H_2O.

We can more clearly see the difference in long term exposure to water and CO_2 at lower temperatures through the contour plots in Figure 3.11. In these contour plots phase shift (θ) is shown as a function of frequency and aging time for samples aged at 450°C in 3% H_2O Figure 3.11 (a) and (b) and 5% CO_2 Figure 3.11 (c) and (d). Changes in θ are closely related to the overall change in the size of an arc, (or peak when referring to Bode plots) and are a fundamental part of impedance measurements. Fundamentally, θ is related to Z" and Z' through:

$$\tan(\theta) = \frac{Z''}{Z'} \qquad [3.1]$$

Assuming Z' remains constant throughout our measurements, based on Eq. 3.1 we can assume that changes in θ correspond to increasing values of Z". The color bar indicates the phase shift values, increasing from the lowest (purple) to the highest (red). In (a) from 0 hours for to about 280 hours we see that the phase is relatively constant throughout the aging process. This indicates that there is little change in the cell throughout this time period. At around 280 hours the water bubbling system was bypassed and only air was flowed to the cell. The subsequent decrease in the low frequency portion of the phase is rapid reaching a steady state 5 hours after switching. This portion of the plot is emphasized in Figure 3.11 (b). The contour plots depicting aging at 450°C in 3% CO_2 Figure 3.11 (c) show a slow, steady increase in the low frequency phase shift values over the course of 500 hours. At around 544 hours the flow of CO_2 to the reactor was shut off and a drop in the low frequency phase shift values is observed. Unlike the sample aged in 3% H_2O there is an initial sharp decrease, followed by a much slower decay continuing beyond 9 hours in air only.

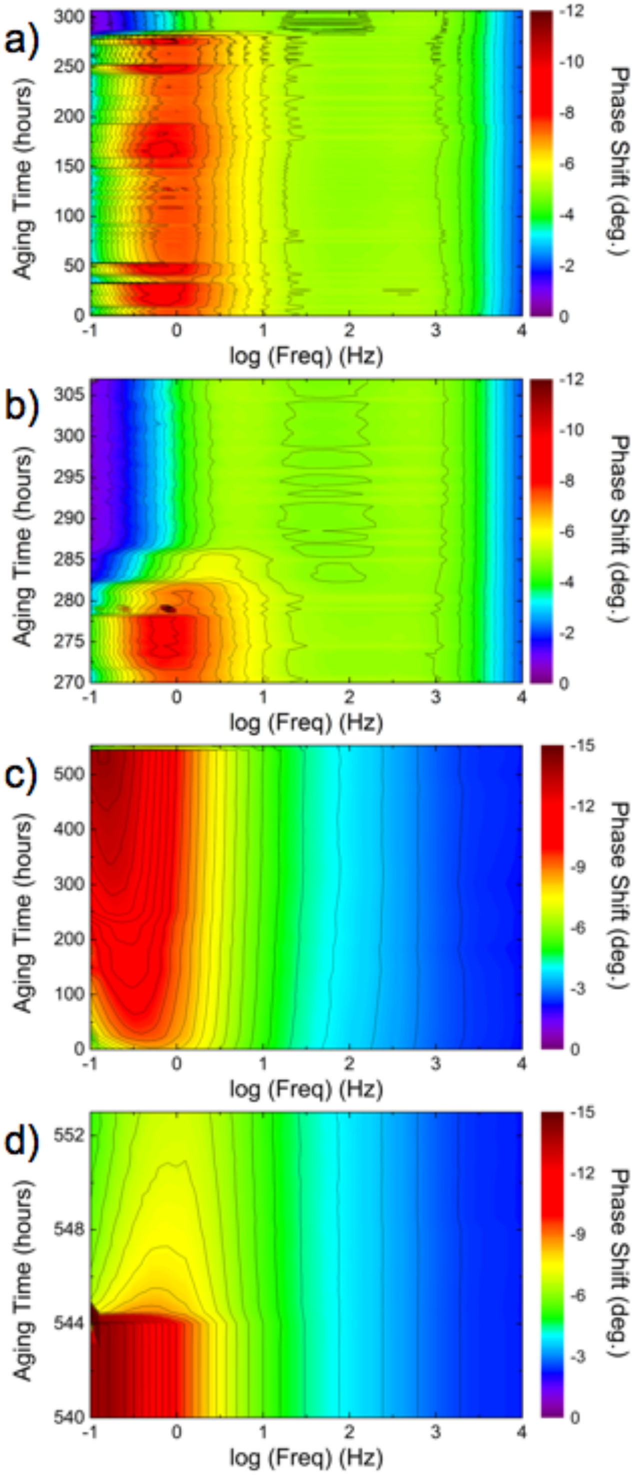

Figure 3.11: Contour plots showing phase shift (θ) as a function of log(Freq) and aging time for samples aged at 450°C in 3% H_2O (a)(b) and 5% CO_2 (c)(d). The colors indicate the phase shift values, increasing from the lowest (purple) to the highest (red).

3.4 Conclusions

The short-term and long-term effects of water and CO_2 on the ORR and cell performance of composite LSCF-GDC cathodes were investigated. We have established a robust approach to de-convolute impedance data and extract meaningful quantities for the various contributions, i.e. the capacitance and resistance of individual components. Our results show that at higher temperatures water may promote the sintering effect on LSCF-GDC and changes microstructure. In addition, the presence of H_2O appears to limit the chemical process of the ORR (R_{LF}), especially as temperature decreases. As operating temperature of SOFC decreases, the effect of water blocking would dramatically increase the polarization loss and should take into account. However, despite the short-term effect of water at lower temperature, the long-term aging affects appear to be non-existent. On the contrary, CO_2 actively participates in the ORR at the LSCF-GDC surface. The short-term effects of CO_2 are similar to those of H_2O but irreversible. There is a definite increase in R_{LF} at both 450 and 750°C, but there are limited changes in the cell after low temperature aging. CO_2 and H_2O effects on LSCF-GDC are both a function of operating temperature. Blocking effects and irreversible increases changes in ORR kinetics at low temperature could significantly decrease cell performance for lower temperature SOFCs.

Chapter 4: Direct Observation of Oxygen Exchange Pathways in Composite Electrodes

4.1 Introduction

Many electrochemical and catalyst technologies depend on the oxygen reduction and oxygen evolution reactions, ORR and OER, respectively.[1,83,84] In solid oxide fuel cells (SOFC), the reduction of oxygen from gaseous molecules to solid phase ions at the cathode is often considered to be the most significant obstacle preventing commercially viable high performance SOFCs.[8,85,86] One route to improve the performance of SOFC cathodes is to gain a more complete understanding of the fundamentals governing the ORR.

The ORR is comprised of at least three major steps:[13,15,16,77] dissociative adsorption – the splitting of the oxygen diatom into individual atoms on the cathode surface, incorporation – a surface bound oxygen atom filling a three-dimensionally bound oxygen site in the lattice, and diffusion (bulk) – the conduction of oxygen ions between lattice sites. The best cathode materials are those that are able to accomplish all three of the steps listed above, along with the ability to transport sufficient electrons to facilitate charge transfer. The most commonly studied SOFC cathode material is strontium-doped lanthanum manganite (LSM).[32,41,47,48,87] LSM, a perovskite oxide, is an electronic conductor that is catalytically active toward the dissociation of oxygen at SOFC operating temperatures[88,57]. However, due to the limited ionic conductivity of LSM,[89] incorporation is confined to the triple phase boundary (TPB) region where oxygen gas, LSM and the ion-conducting electrolyte meet.[16,90] The main approach to overcome this limitation is to create a composite cathode by mixing LSM with the ion conducting electrolyte material, yttria stabilized zirconia (YSZ), significantly increasing the TPB.[23,45,91,92] This study describes the development of a method for investigating the ORR on composite materials, elucidating changes in oxygen exchange mechanisms for LSM, YSZ and their composite LSM-YSZ. In a composite cathode, the kinetics of the ORR can change significantly, with the appearance of new temperature dependent rate limiting steps that don't exist for either individual material.

There are a few techniques described in literature for probing oxygen exchange on non-stoichiometric oxide materials; where catalysis meets solid-state ionics. Isotope exchange depth profiling with secondary ion mass spectroscopy (IEDP-SIMS) has been used to extract surface exchange constants (k_{ex}) and diffusion coefficients (D^*) for a number of cathode materials.[90,54,56] Unfortunately, more detailed information concerning the individual reaction steps that contribute to k_{ex} cannot be determined from *ex-situ* analysis. Other techniques such as impedance spectroscopy[27,44,45,93] or current-voltage analysis (e.g. Tafel-plots)[94–96] use electrochemical measurements to probe cathode kinetic and can provide an abundance of information from the material response. However, the assignment of specific kinetic processes under such testing conditions can be somewhat arbitrary, partially due to the fusion of multiple steps in the ORR.[97] Here, we have developed a method to probe the ORR using a combination of *in-situ* gas phase isotopic oxygen exchange and electrochemical impedance spectroscopy (EIS) on LSM, YSZ and LSM-YSZ composite.

Using a technique known as 1:1 isothermal isotope exchange (1:1 IIE), described in detail previously[61] we can determine the rate of dissociation (r_{dis}) and the surface exchange coefficient (k_{ex}). This *in-situ* technique probes the isotopically labeled transient signal of the oxygen self-exchange process at steady state, allowing us to separately monitor oxygen dissociation and overall surface reactions. From a catalysis perspective, the dissociation of oxygen is perhaps the most important role of the cathode material, as the energy required to dissociate oxygen is extremely high (498kJ/mol).[11] In 1:1 IIE a powder sample with a total surface area of 0.1 m^2 placed inside a plug-flow reactor is subjected to an isobaric switch in the concentration of isotopically labeled oxygen gas from $^{16}O_2$, the most abundant isotopologue, to a 50-50 split of $^{16}O_2$ and $^{18}O_2$. The gas effluent is monitored by a down-stream quadrupole mass spectrometer (QMS), which is used to determine concentrations of the three oxygen isotopologue mass signals: *32* (m/z) from $^{16}O_2$, *36* (m/z) from $^{18}O_2$, and *34* (m/z) resulting from the mixed product $^{16,18}O_2$. The relative concentration of each oxygen isotopologue as a function of exchange time can be used to determine kinetic parameters governing the ORR, such as dissociation rate (r_{dis}), isotope fraction in the lattice (λ_{latt}), and surface exchange coefficient (k_{ex}).

Oxygen exchange on O^{2-} conducting materials can be classified into two major types, homogeneous exchange, and heterogeneous exchange.[52] In homogeneous exchange, two dissociated oxygen molecules exchange an atom, where the oxide surface provides sites for dissociative adsorption and decreases the energy for the reaction. Heterogeneous exchange involves a more intimate role of the oxide, where a solid phase surface atom from the oxide exchanges with an atom in the adsorbed oxygen molecule. This type of exchange is more relevant to the ORR for SOFC cathodes as it is leads to the bulk diffusion of oxygen ions. Figure 4.1 is a simple sketch showing the exchange process during 1:1IIE. Initially the inlet oxygen *32* and *36* dissociate on the surface and form surface bonded atoms, as depicted in I. Following I, either homogeneous exchange (IIa), or heterogeneous exchange (IIb), will occur. The types and rates of exchange on the surface (I, IIa, and IIb) determine the isotopologue distribution in the effluent gas.

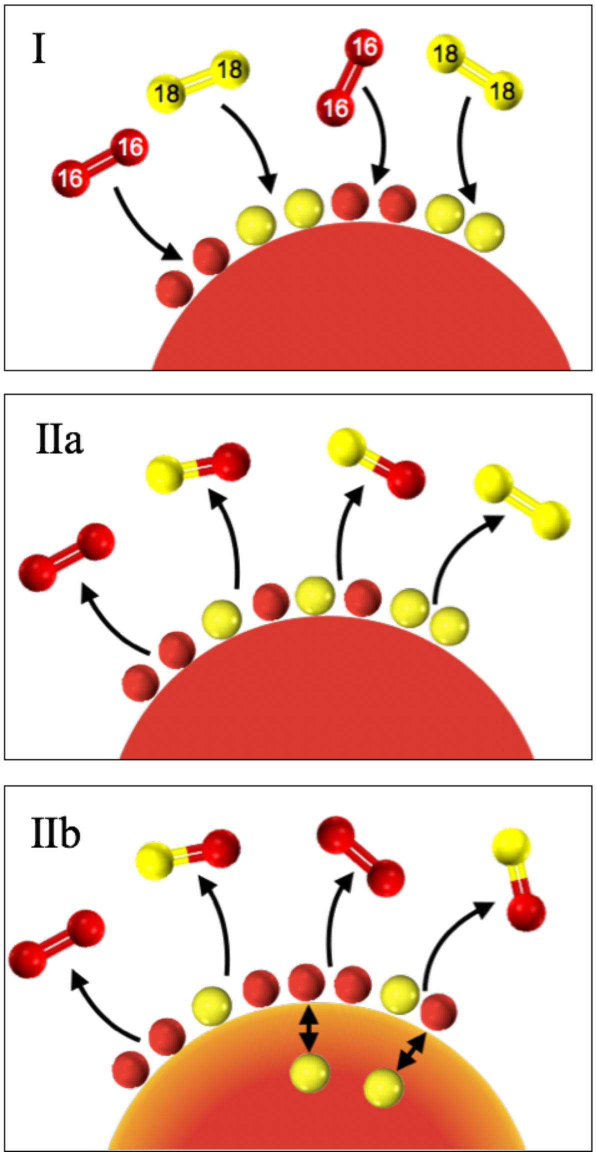

Figure 4.1: A sketch showing the exchange process during 1:1IIE. (I) Inlet $^{16}O_2$ (*32*) and $^{18}O_2$ (*36*) dissociate on the powder surface. The exchange can then follow one of two paths: (IIa) re-association and desorption, commonly referred to as homogeneous exchange; (IIb) incorporation and exchange with lattice (solid phase) oxygen, referred to as heterogeneous exchange. Heterogeneous exchange, IIb, also typically results in O^{2-} diffusion and a change in the isotopic distribution in the solid.

Using fundamental kinetic information obtained for LSM and YSZ as independent materials, we consider the ORR kinetics and the role of each material in composite LSM-YSZ system. Isotope exchange is a powerful technique for extracting fundamental kinetics, however, it does not account for the impact of microstructure on the ORR. In order to relate the oxygen exchange from a materials perspective back to oxygen exchange on a real cathode, we performed EIS on LSM and LSM-YSZ composite cathodes using symmetrical cell measurements. Combining results from 1:1 IIE and EIS we have determined ORR kinetics for LSM, YSZ and their composite, and propose a reaction pathway based on the results.

4.2 Experimental

Commercial LSM (Fuel Cell Materials), YSZ (Tosoh), and composite LSM-YSZ (Fuel Cell Materials) powders were used and the sample weights were selected such that the total surface area from N_2 adsorption was 0.1 m^2. The powders, loaded in quartz tube reactors, were then connected into the isotope exchange set-up, where we control the gas environment inside the reactor and measure the effluent using a quadrupole mass spectrometer (QMS). Mass flow controllers (MKS) were used to control the mass flow rates of He and O_2 (Airgas), while the isotopically labeled $^{18}O_2$ (95% pure; Sigma-Aldrich) flow rates were controlled with a special low-range mass flow controller (Alicat Scientific). Samples were heated to 800°C to clean the surface of any adsorbents, then cooled to the test temperature. A pneumatically actuated valve (Valco Instruments) was used to change the gas composition entering the reactor from 5% $^{16}O_2$ to 2.5% $^{16}O_2$ with 2.5% $^{18}O_2$, all balanced in He. The He carrying the $^{18}O_2$ gas stream also contains a small amount (1000ppm) of Ar, used to detect the gas switch.

Symmetrical cells consisting of an LSM (LSM-YSZ) working electrode, YSZ electrolyte, and LSM (LSM-YSZ) counter electrode were fabricated using standard procedures. YSZ powder was uni-axially pressed in a 10mm diameter die and sintered at 1400°C for 6 hours. The sintered pellets were then polished to a thickness of 5mm. Subsequently, LSM (LSM-YSZ) cathode paste (Fuel Cell Materials) was printed on the top and bottom of the YSZ pellets and sintered at 1100°C for 2 hours. A thin layer of Au paste was painted on both the working and counter electrodes and dried at room temperature for 1 hour. The cells were then loaded into a custom built single-environment reactor and heated to 875°C for 15 minutes to fire the Au paste before being cooled to the testing temperature. The gas environment was controlled using mass flow controllers (MKS). EIS measurements were performed using a 1400 Frequency Response Analyzer and a 1470 Cell Test System (Solartron Analytical).

4.3 Results and Discussion

Representative results from 1:1 IIE on LSM, YSZ and LSM-YSZ composite at 400°C, 600°C, and 800°C are show in Figure 4.2 (a), (b), and (c) respectively. The experiments are performed under atmospheric pressure with a total PO_2=0.05 atm., balanced in He. The concentrations of *32*, *34* and *36* as a function of time are shown for each plot, as black, red and blue symbols, respectively. The isobaric switch from $^{16}O_2$ to a 1:1 ratio of $^{16}O_2$:$^{18}O_2$ occurs at time t=0. The experiments are concluded once there are no longer changes in the concentrations of each isotopologue. It is readily apparent from the exchange curves that there are significant differences in oxygen exchange for the samples at each temperature. At lower temperatures, where less total heterogeneous exchange occurs, the time to reach equilibrium is much shorter, as seen for LSM at 400°C and

600°C and YSZ at 400°C. The experiments are stopped at much shorter time lengths as to not waste $^{18}O_2$. The relative amounts of homogeneous and heterogeneous exchange will determine the values of *32*, *34* and *36* throughout the experiment. In the following, we perform an in depth analysis of the exchange curves.

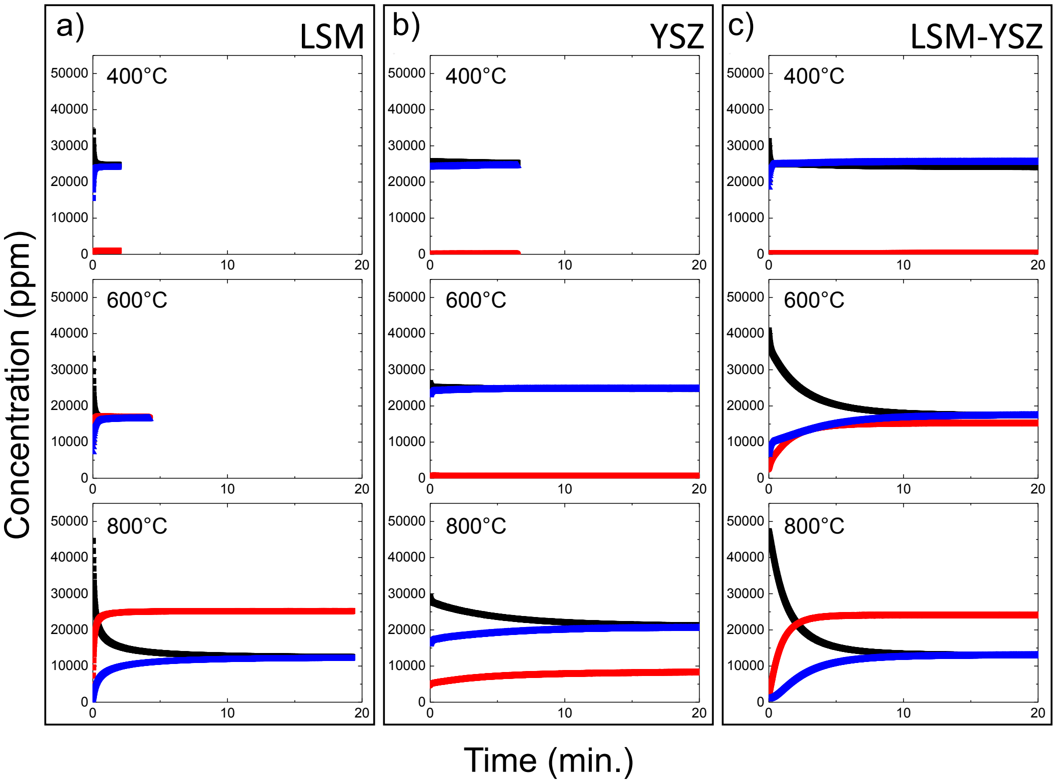

Figure 4.2: 1:1IIE exchange curves for LSM, YSZ, and LSM-YSZ, (a), (b), and (c), respectively. The concentrations in ppm of *32*, *34* and *36* as a function of time in minutes are shown for each plot, as black, red and blue symbols, respectively. The isobaric switch from $^{16}O_2$ to a 1:1 ratio of $^{16}O_2$:$^{18}O_2$ occurs at time t=0 and the experiments are stopped once the curves level off.

One important aspect of an exchange curve is the steady state value of the *34* signal. At steady state, the isotopic distribution in the gas phase is in equilibrium with the isotopic distribution in the solid phase, and any further gas-solid exchange is unobservable. The steady state condition allows us to separate the gas-surface reactions (e.g. dissociation and reassociation) from the other steps in the ORR, where the formation of *34*, the mixed $^{16}O^{18}O$ oxygen molecule, represents the dissociation of oxygen on the catalyst surface, and a greater value of *34* is a higher rate of dissociation. At 400°C all three samples show low *34* signals once the sample has reached steady state, indicating that the gas phase oxygen is not exchanging with the powder surface. At 600°C and 800°C, we can see a difference between YSZ and the two samples that contain LSM. The YSZ sample still has very low *34* formation at 600°C and less than 10,000ppm at 800°C, while LSM and LSM-YSZ show similar steady state *34* concentrations at both 600°C and 800°C, with higher values than YSZ. Figure 4.3 (a) is a plot of the concentration of *34*, the mixed oxygen product, as a function of temperature. The *34* concentrations are extracted from the end of each 1:1 IIE experiment, when the isotopologues are at their steady-state values. YSZ has the lowest *34* values across all temperatures, only reaching 10,000ppm at 800°C. LSM and LSM-YSZ both show exponential increases in dissociation from 400°C to around 700°C, where the concentrations of *34* reach a maximum of 25,000ppm. If we consider a system in which we have four ^{16}O atoms and four ^{18}O atoms, and we randomly select two atoms (or a molecule) from the system, the probability to pick a 16-16 pair or an 18-18 pair is 25%, while a 16-18 pair (or 18-16, as they are the same) pair is 50%, leading to a ratio of 1:2:1 for *32*:*34*:*36*. Based on this random distribution, we can expect a maximum of 25,000ppm for the *34* signal. Therefore, for both LSM and LSM-YSZ we reach a maximum *34* signal at around 700°C, meaning all of the oxygen molecules entering the system are dissociated by the powder sample and the reaction is limited by mass transfer, i.e. the amount of oxygen molecules flowing across the powder per unit time. Normalizing the *34* concentration to the sample surface area and the O_2 flow rate, we can extract the dissociation rate, r_{diss} (mol m^{-2} s^{-1}). An Arrhenius plot of r_{diss} versus inverse temperature is shown in Figure 4.3 (b). From this plot we can extract apparent activation energies for dissociation for LSM, YSZ, and their composite. It is important to note that r_{diss} does not account for the number of active sites per surface area for each material, due to difficulty quantifying the number of active sites in nonstoichiometric metal oxides under actual test conditions. A more rigorous characterization of the material surface could potentially lead to a fundamental rate constant for oxygen dissociation and re-association and extraction of the turn-over-frequency (TOF).

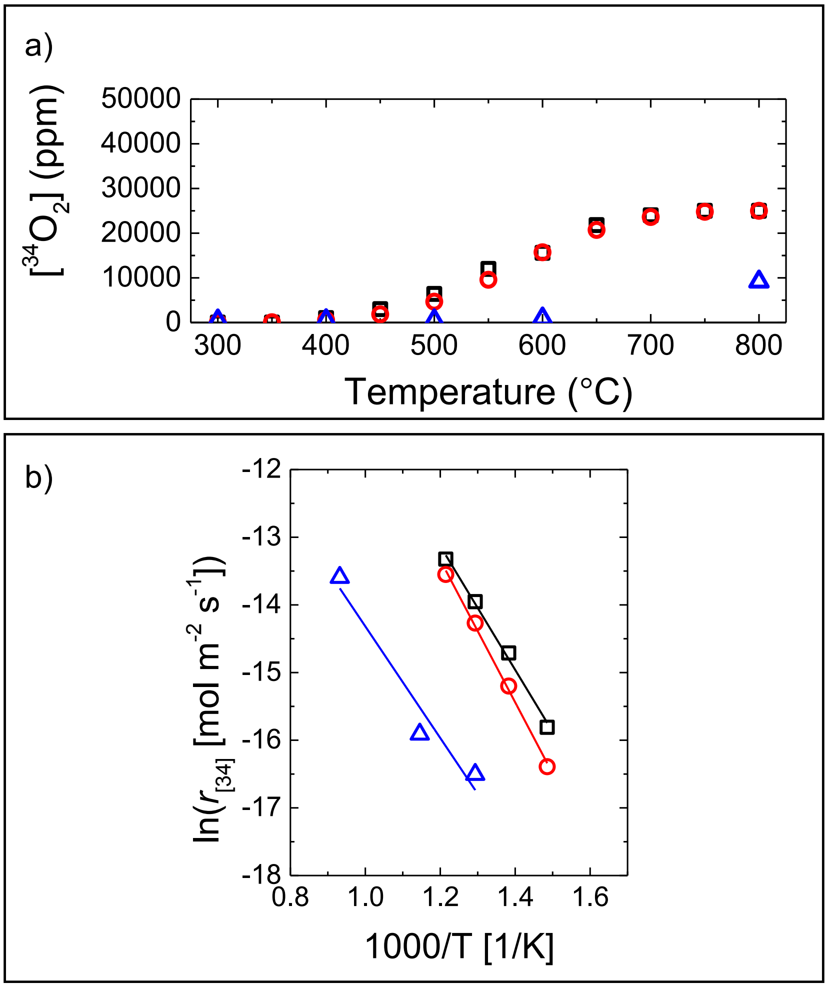

Figure 4.3: The concentration of *34* in ppm (a) and the rate of *34* formation (b) as a function of temperature for LSM (black squares), YSZ (red circles), and LSM-YSZ (blue triangles). The lack of *34* concentration for YSZ from 300-600°C indicates that very little surface dissociation occurs. This is not the case for LSM, and LSM-YSZ, which both show an exponential increase in *34* formation with increasing temperature.

The gas-solid exchange, heteroexchange, can be quantified by calculating the exchange flux, $J(t)$ (the flux of oxygen from the gas phase into the solid phase), using Eq. 4.1, where N is the number of atoms per second entering or leaving the system. Integrating Eq. 4.1 with respect to time, we get the concentration of ^{18}O in the solid phase as a function of time, $M(t)$, shown in Eq. 4.2.

$$J(t) = 2N_{36}^{inlet}(t) - 2N_{36}^{outlet}(t) - N_{34}^{outlet}(t) \qquad [4.1]$$

$$M(t) = \int_0^t J(t)\, dt \qquad [4.2]$$

LSM and YSZ at 400°C and 600°C both show a rapid change from their initial to steady state values, indicating that there is not significant levels of incorporation. In general, the longer it takes to reach steady state values and the greater the area between the *32* and *36* curves, the greater the amount of incorporation. Low levels of incorporation for LSM at 400°C and 600°C are likely caused by a lack of oxygen vacancies at these temperatures. YSZ on the other hand has much higher O^{2-} conductivity due to high oxygen vacancy concentration, and is likely limited by oxygen adsorption/dissociation on the surface at these temperatures. Note that isotope exchange probes the self-exchange process and the levels of oxygen vacancies are crucial for exchange to occur. At 800°C, both the LSM and YSZ exchange curves show higher levels of incorporation, taking *ca.* 15 minutes to reach steady state. Compared to LSM and YSZ, LSM-YSZ composite shows higher levels of incorporation at all three temperatures. The flux curves for LSM-YSZ from 400-750°C are shown in Figure 4.4 (a). As the test temperature increases we can see that the flux curves change more rapidly as time increases, in addition to starting at higher initial values. Higher flux values correspond directly to higher rates of heterogeneous exchange, and O^{2-} incorporation.

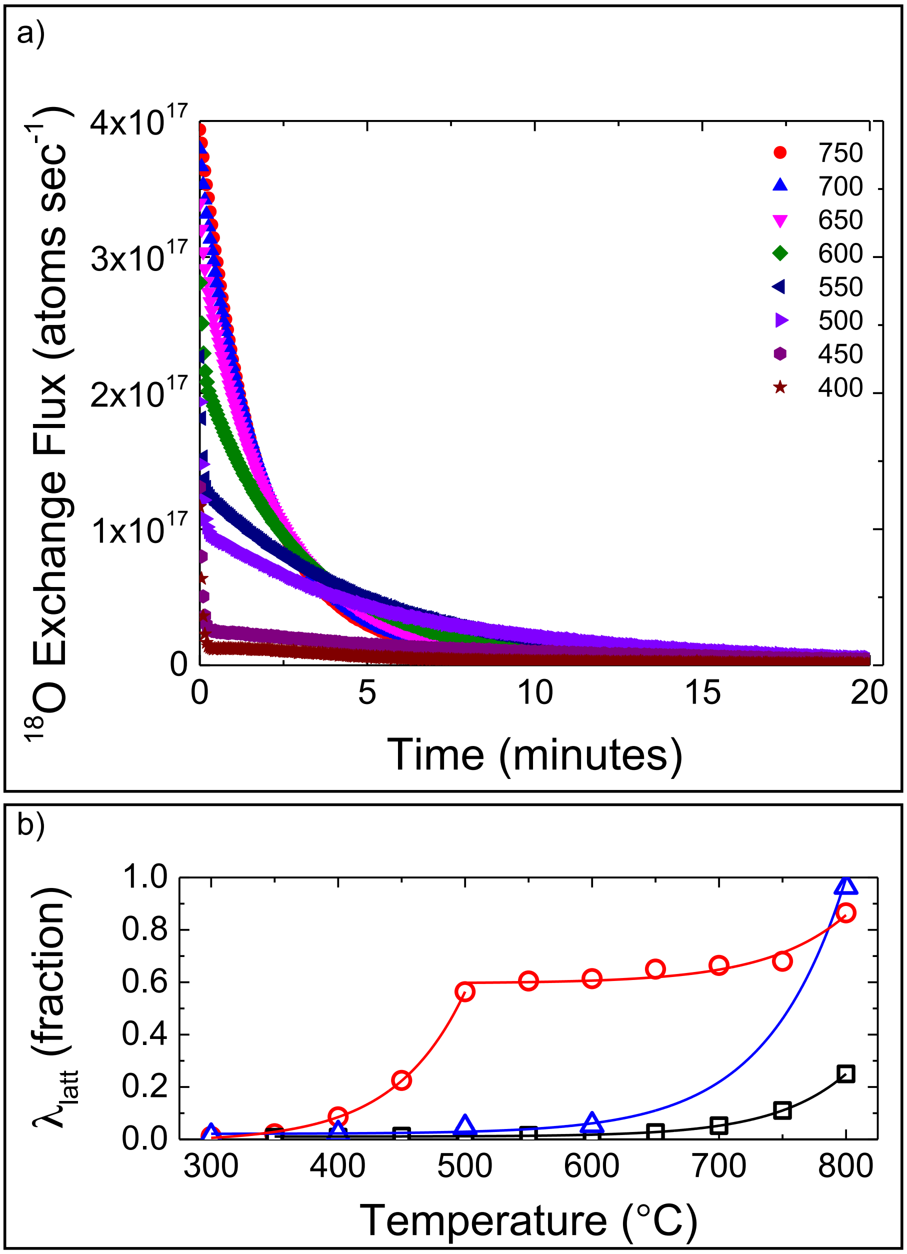

Figure 4.4: The oxygen exchange flux, *J(t)*, for LSM-YSZ composite from 400-750°C (a). The flux is calculated using Eq. (1) and can be used to determine surface exchange coefficients, in addition to the amount of accumulated oxygen in the lattice. The accumulated oxygen at time at steady state, M(∞), can be used to calculate the fraction of exchanged oxygen in the lattice, λ_{latt}. This fraction is plotted as a function of temperature (b) for LSM (black squares), YSZ (red circles), and LSM-YSZ (blue triangles).

Using the Eq. 4.2, we can calculate the amount of accumulated oxygen in the solid phase at steady state, $M(\infty)$. Normalizing the number of exchanged oxygen in the lattice to the number of oxygen sites, we can plot the total fraction of exchanged oxygen,

λ_{latt}. The temperature dependent exchange fraction in each material and their composite provides important information regarding the activity of lattice oxygen participating in heterogeneous exchange. Figure 4.4 (b) is a plot of the total fraction of lattice oxygen, from 0 to 1, that has exchanged from ^{16}O to ^{18}O at steady state. The data is normalized to the 1:1 ratio of ^{16}O:^{18}O, where 50% of the lattice occupied by ^{18}O is equal to 100% conversion. LSM (black squares) shows the lowest levels of heteroexchange, or the smallest fraction of accessible lattice sites, across the entire range of temperatures. At 800°C LSM only exchanges around 25% of it's lattice sites, meaning that the majority of them are still inaccessible. YSZ shows similar levels of exchange from 300°C to 600°C, where the fraction of lattice sites exchanged is below 10%. However, at 800°C the fraction of lattice sites exchanged in YSZ is close to 100%. For both LSM and YSZ, there is an exponential increase in the fraction of lattice exchange as temperature increases. Interestingly, for LSM-YSZ we see two separate exponential increases in lattice incorporation. First, lattice exchange increases from around 0% at 300°C to close to 60% at 500°C. Above 500°C there is almost no increase in lattice exchange until around 750-800°C, where we see a second exponential increase. Unlike YSZ, at 800°C the total level of incorporation only reaches around 85%.

LSM and YSZ both show very low incorporation fractions (Figure 4.4 (b)), with the levels of incorporation in YSZ increasing much more rapidly above 600°C. However, dissociation rates for LSM are much higher than for YSZ (Figure 4.3 (a)), for which dissociation is immeasurable at temperatures lower than 600°C. Comparing the individual materials to the composite cathode, LSM-YSZ shows significantly greater incorporation between 400°C and 750°C, and dissociation rates that are almost equal to those of LSM. If we consider the sequential steps in the ORR the results become clearer. For YSZ, it is likely that the low levels of dissociation, the first step in the ORR, are limiting the amount of incorporation in the 400-600°C temperature region. In contrast, LSM shows higher levels of dissociation, but the low vacancy concentration decreases oxygen ion conductivity reducing incorporation and diffusion. Previously, authors have described LSM as having a small near-surface region for which it is active toward oxygen diffusion, and that only at very high temperature (or under external driving force) does the bulk become active.[18,19] Combining the two materials in a composite powder, we can assume that LSM maintains its ability to dissociate oxygen, while YSZ maintains its incorporation and bulk diffusion properties. It is therefore likely that the two separate exponentials we observe λ_{latt} for LSM-YSZ, as shown in Figure 4.4 (b), result from a new reaction pathway in which LSM is dissociating O_2 and YSZ is incorporating the O-atoms into bulk, leading to the first of the two exponential increases. From 500°C to around 650°C the lattice exchange fraction appears to level-off at about 60% of the total number of lattice sites. Calculating the O-site fraction for YSZ in the LSM-YSZ composite yields a ratio of 0.4:0.6 for LSM:YSZ. This also explains why only ~85% of the total number of sites in LSM-YSZ are filled at 800°C, as the LSM in the composite is still limited to a maximum λ_{latt} of 0.25.

Impedance spectroscopy measurements were made on symmetrical cells consisting of YSZ electrolyte pellets fabricated using hydraulic pressing and sintering, followed by blade coating LSM or LSM-YSZ cathode paste. The symmetrical cells were tested in synthetic air (21%O_2, N_2 balance) in a custom built reactor using Au paste as a current collector. Select Nyquist plots at 550°C, 650°C, and 750°C for LSM and composite LSM-YSZ symmetrical cells are shown in Figure 4.5 (a)-(c). An equivalent circuit model composed of an ohmic resistance in series with two RC components, illustrated in Figure 4.5 (d), was used to fit the spectra for both the LSM and LSM-YSZ symmetrical cells. The LSM and LSM-YSZ responses both consist of an ohmic offset attributed to the bulk resistance of the YSZ electrolyte, followed by a high-frequency arc with a characteristic capacitance near 10^{-6} F. The insets in Figure 4.5 (a)-(c) highlight the high-frequency arcs for both samples. Following the high-frequency arc, the LSM sample has a large low-frequency arc with a characteristic capacitance near 10^{-3}F. The LSM-YSZ symmetrical cell also has a low-frequency portion of the spectra, observable in the Nyquist plot insets. However, in contrast to the LSM sample, this low-frequency portion appears to be composed of two overlapping arcs. Interestingly, the lowest frequency portion, or the third arc, has a characteristic capacitance that is closer to 10^{-2} F, indicating that the low frequency processes for the two cathodes may be different. The magnitude of the low-frequency arc for the LSM cathode is significantly larger than those for the LSM-YSZ sample across all measured temperatures. Figure 4.5 (e) is an Arrhenius plot showing the logarithm of the area specific resistance (log(ASR)) versus inverse temperature. The black squares represent the ASR of the high-frequency arcs for the LSM (open) and LSM-YSZ (closed) samples, while the red circles are the resistances of the low-frequency arcs. The Arrhenius plots further demonstrates the similarity between the high-frequency arcs in the LSM and LSM-YSZ spectra, and the difference in magnitude between the low-frequency portions. A number of experiments on LSM and LSM-YSZ cathodes have been performed previously, yielding a range of results that depend on fabrication and specific testing conditions.[40,47,91,98,99]

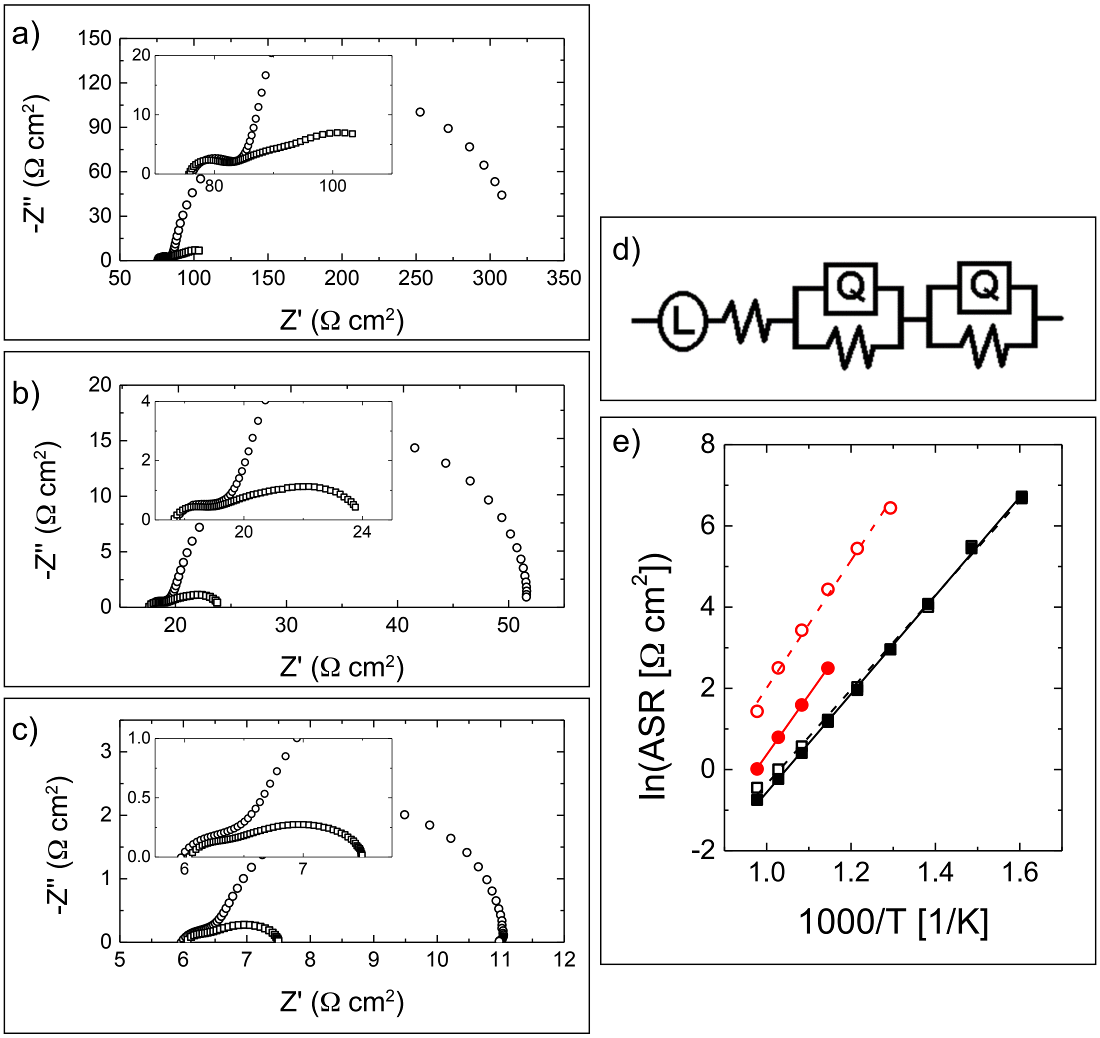

Figure 4.5: Impedance spectra for LSM (black squares) and LSM-YSZ (black circles), at (a) 550°C, (b), 650°C, and (c) 750°C. The insets highlight the much smaller LSM-YSZ spectra. The impedance spectra at each temperature were fit using the simple Voigt circuit (d) consisting of an inductor in series with a resistor and two resistor-CPE parallel circuits. Arrhenius plots of the high and low frequency arc resistances (e) illustrate the similarities between the high frequency arcs (squares), and differences between the low frequency arcs (circles), for LSM (open symbols) and LSM-YSZ (closed symbols). The apparent activation energies for each component can be extracted using a linear fit.

Cronin et al.[40] performed the most similar measurements on LSM-YSZ cells, in which the authors claim that the high frequency response observed is related to grain boundaries in the cathode microstructure, due to a low PO_2 dependence, along with a high activation energy (1.04eV) and a dependence on cathode sintering temperature. Although the explanation of grain boundary resistance in the cathode is a possible explanation, the matching results we obtain for LSM and LSM-YSZ, and a similar high frequency arc observed for YSZ pellets tested with Au electrodes,[95] leads us to believe that the high frequency arc we observe, with no dependence on PO_2 and activation energies of 1.01 and 1.05eV for LSM and LSM-YSZ, respectively, is caused by grain boundary resistance in the YSZ electrolyte. The low-frequency portion of the spectra for LSM and LSM-YSZ are then left to account for processes involved in the ORR. The activation energies of the low-frequency arcs for LSM and LSM-YSZ are similar, within 0.1eV, however the size of the low-frequency arc in LSM is over an order of magnitude greater than that in LSM-YSZ. The significant difference between the two cathodes are total area of LSM and YSZ interface and the totally length of triple phase boundary. Therefore, we can conclude that the resistive and capacitive elements comprising the low-frequency arc must be related to one or both of these parameters.

Based on the above results, we propose the energy barrier schematic for oxygen transport in LSM-YSZ composite, presented in Figure 4.6 (a), to describe the most likely reaction pathways. Each reaction step can be represented by an energy barrier to describe the energy required for the reaction to proceed. As shown in Figure 4.6 (a), YSZ and LSM have different activation energies for dissociation and incorporation, for which YSZ is favorable for incorporation and LSM for dissociation. Although LSM has a lower energy barrier for oxygen dissociation, incorporating oxygen into the LSM lattice has a much higher energy barrier, limiting the amount of oxygen exchange. On the other hand, a lack of ability to dissociate oxygen on YSZ inhibits the formation of dissociated oxygen on the YSZ surface for incorporation even though YSZ has a lower energy barrier for incorporating oxygen. In LSM-YSZ composite, due to the high energy barrier for dissociation on YSZ and oxygen incorporation in LSM, the transport of oxygen tends to follow the pathway with the lowest energy: dissociation on LSM, followed by interphase transport between LSM and YSZ through surface diffusion, and eventually incorporation into YSZ. Based on the proposed mechanism we can fit the oxygen accumulation curves from Eq. 4.2, using either a single or two-pathway model, the results of which are shown in Figure 4.6 (b) and (c). The surface exchange coefficient (k_{ex}) can be extracted using Eq. 4.3, under conditions in which diffusion is not the limiting process. Due to the experimental set-up, and the small grain size for the samples the surface exchange limitation applies.[57]

$$\frac{M(t)}{M_{\infty}} = 1 - \exp\left(-\frac{3k_{ex}t}{a}\right) \qquad [4.3]$$

Figure 4.6 (b) is an Arrhenius plot of k_{ex} with respect to temperature using the single pathway model, in which transport through one material is allowed. In Figure 4.6 (c) we fit the flux curves using the two-pathway model where oxygen only transports from the LSM surface to the YSZ bulk at lower temperature (below 600°C), and the formation of a new pathway above 600°C, where incorporation into LSM is also possible. Fitting results suggest that the two-pathway model is a more likely explanation for oxygen exchange on LSM-YSZ composite powder under the conditions tested.

Comparing the results from 1:1 IIE and impedance spectroscopy, we need to consider the fundamental principles governing each experiment, as there are some similarities and differences. Both experiments are being performed under open-circuit conditions, e.g. there are no external driving forces pushing O_2 molecules or atoms in any particular direction. In the 1:1 IIE experiments we are able to completely separate the studies on the individual materials and then the composite, providing a more complete

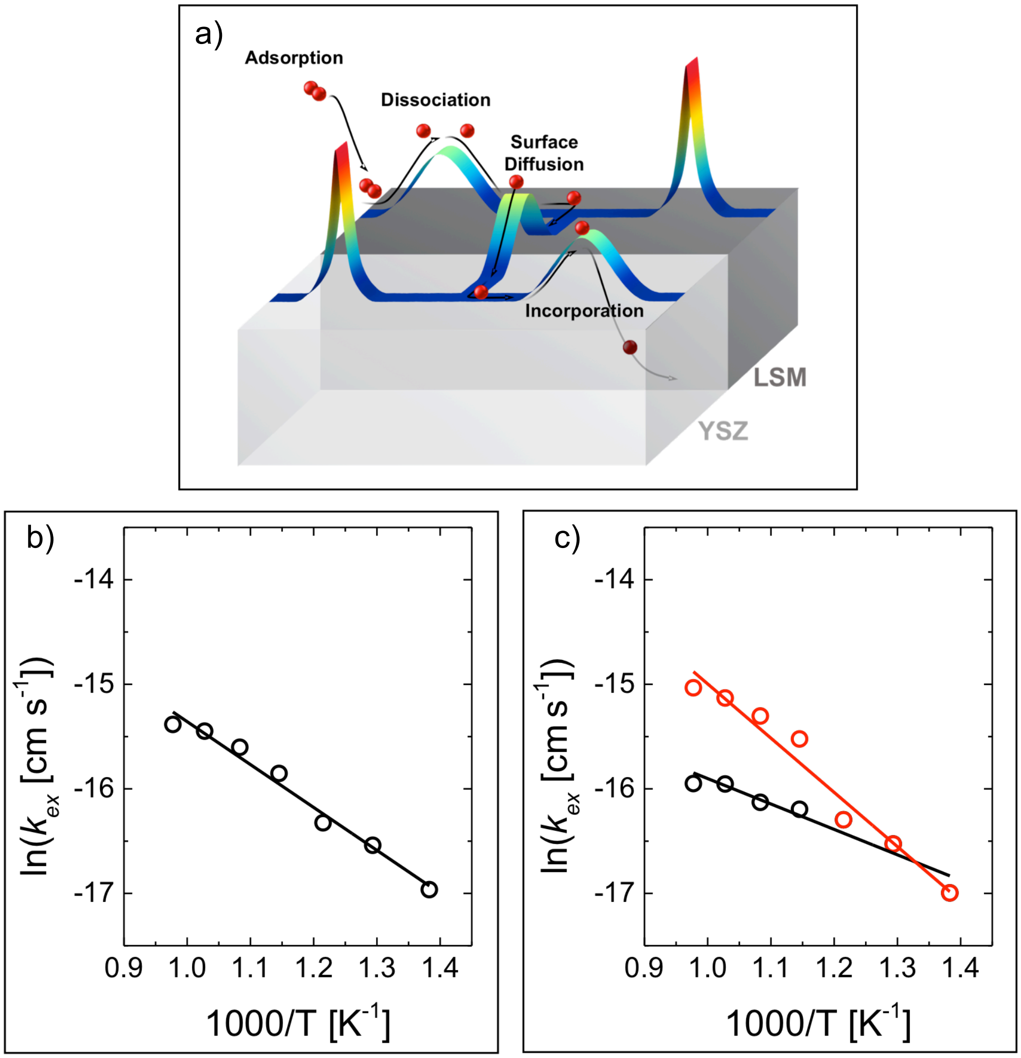

Figure 4.6: Schematic for oxygen transport in composite LSM-YSZ where each reaction step can be represented by an energy barrier (a). YSZ and LSM have different activation energies for dissociation and incorporation, for which YSZ has a lower activation energy for incorporation but a higher activation energy than LSM for dissociation. This leads to two pathways that depend differently on temperature. Fitting of surface exchange coefficients use single-pathway (b) and two-pathway (c) mechanisms.

picture. For impedance spectroscopy, all tests are carried out on YSZ electrolyte, e.g. even for the LSM cathode the response observed can be related to the interface between the LSM cathode and the YSZ electrolyte. The results from 1:1 IIE show us that the only significant difference between the LSM and LSM-YSZ composite powders are in their ability to incorporate oxygen. The dissociation between 400°C and 600°C is similar for both materials, while incorporation into the YSZ in the composite is significantly higher.

In addition, for both 1:1 IIE and EIS we see that there are two distinct processes occurring on similar orders that change differently as a function of temperature: for EIS we see the development of two overlapping arcs as we reach 600°C, while for 1:1IIE the model developed and subsequent fitting of k_{ex} suggests a two-pathway mechanism for exchange.

4.4 Conclusions

Gas phase oxygen isotope exchange on metal oxides and their composites contain real time information to not only quantify dissociation and surface exchange rates but also identify different possible pathways. Oxygen transport on LSM-YSZ composite has been determined via gas phase isotopic oxygen exchange based on a three-step reaction model to individually determine oxygen dissociation and overall surface exchange kinetics. Temperature dependence of oxygen dissociation and overall surface exchange on LSM, YSZ, and LSM-YSZ composite show that LSM, YSZ, and LSM-YSZ have different apparent activation energies. Compared with pure phase LSM and YSZ, total oxygen dissociation on LSM-YSZ is enhanced, possibly due to the third pathway for oxygen dissociation. Pure LSM and YSZ powders only incorporate oxygen above 650°C because of limitations in incorporation and dissociation, respectively, while oxygen incorporation can be observed on LSM-YSZ as low as 400°C. EIS and isotope exchange characterization techniques are combined to elucidate the reaction kinetics of the ORR on composite cathode. An energy-pathway diagram for oxygen transport on composite has been presented. Our work provides a unique point of view for oxygen transport and surface exchange kinetics, a potentially valuable method for evaluating new or lesser-understood composite materials active toward oxygen exchange.

Chapter 5: Role of Water in Oxygen Exchange on Composite LSM-YSZ

Electrochemical reactions on electron and ion conducting oxide materials have wide-ranging application for a number of different technologies. The overall reaction pathway can be described by redox surface reactions occurring between gas phase molecules and catalytically active surfaces, followed by incorporation of surface ions into solid phase electrodes and electrolytes. The combination of heterogeneous catalysis and solid state ionics often leads to challenges in characterizing the fundamental mechanisms governing the overall reaction. Improved techniques and understandings of these systems can aid the development of novel materials to drive progress in numerous energy conversion technologies.[1,83,84]

Oxygen reactions on (LaSr)$MnO_{3\pm\delta}$ (LSM) and $ZrO_2(Y_2O_3)$ (YSZ) are some of the best studied in the field. LSM, a perovskite family oxide, is an electrode material commonly used in solid oxide fuel and electrolyzer cells (SOFC/SOEC) where the oxygen reduction (ORR) and oxygen evolution reactions (OER) take place. LSM, a majority electron conductor, is often paired with the fluorite-structure oxygen ion conductor YSZ to enhance oxygen incorporation kinetics. The interface between LSM, YSZ, and the gas phase is referred to as the triple phase boundary (TPB), and has been shown to scale proportionally with electrode performance.[100] The net oxygen exchange reaction at equilibrium is:

$$\frac{1}{2}\mathrm{O_2} + 2\mathrm{e'} + \mathrm{V_O^{\cdot\cdot}} \leftrightarrow \mathrm{O_O^x} \qquad [5.1]$$

where $V_O^{\cdot\cdot}$ denotes an oxygen vacancy and O_O^x represents oxygen in an oxygen site. The reaction in Eq. 5.1 occurs rapidly on solid oxide electrode materials in both the forward and backward directions, and scales proportionally with temperature. Relative rates of exchange describe the activity of a material toward the ORR/OER.

Although the majority of research on LSM and YSZ concerns oxygen reactions, there have been a number of publications studying the effects of other oxygen-containing gaseous species, namely H_2O and CO_2, on these and similar materials.[33,35,37,69,101–108] Isotope exchange depth profiling (IEDP) results have shown that surface oxygen exchange on YSZ is significantly enhanced in humidified environments,[35,101,109–112] attributed to surface oxygen vacancies ($V_O^{\cdot\cdot}$) and hydroxyl groups (OH^-). Recently, IEDP experiments on mixed conducting perovskites $La_{0.6}Sr_{0.4}FeO_{3-\delta}$ and $SrTi_{0.3}Fe_{0.7}O_{3-\delta}$ revealed a significant increase in oxygen incorporation originating from labeled $H_2{}^{18}O$ in both oxidizing and reducing atmospheres.[113] Literature suggests that water readily participates in surface exchange reactions on ion conducting materials.

In this work, we explore the effects of humidification on LSM-YSZ composite to elucidate competing water and oxygen reaction mechanisms. Initial performance measurements using EIS were collected for both LSM and LSM-YSZ composite electrodes. The results show an overall decrease in cell resistance with humidification. A mechanistic investigation was then carried out using *in situ* gas phase isotopic oxygen exchange to determine dissociation rates and surface exchange rates with humidification. Comparing the results obtained in this investigation with those from previous works,[64] we propose that the role of water in oxygen exchange on composite LSM-YSZ cannot be fully described by its effect on the individual materials. Dissociation rates on LSM-YSZ decrease with humidification, in contrast to changes observed for LSM alone, suggesting a blocking mechanism related to the LSM-YSZ interface. Despite a decrease in dissociation, the overall surface exchange coefficient is slightly higher with humidification, a result that mimics electrochemical measurements.

5.1 Results and Discussion

Electrochemical measurements, such as electrochemical impedance spectroscopy (EIS), can be used to probe the overall effect of humidification on electrodes, but are limited in their ability to apply specific mechanisms to the observed results. EIS was conducted on LSM and LSM-YSZ symmetrical cells dry and humidified air to determine the overall water effect on LSM-YSZ composite. Figure 5.1 (a)-(c) contains Nyquist plots of impedance measurements made on LSM and LSM-YSZ electrodes in synthetic air (21% O_2, 79%N_2) and synthetic air with the addition of 3% water. The differences between the measurements on LSM and LSM-YSZ composite occur solely in the low-frequency portion of the spectra, where gas-solid exchange kinetics dominates. This result can be boiled down to the increased TPB length for the composite. For both LSM and LSM-YSZ the addition of 3% humidification in the gas stream changes the size of the low frequency arc. As the high frequency portion of the spectra does not change due to cathode composition or gas humidification, we choose to not consider it in this analysis.

The low frequency arc in the impedance spectra is fit using a simple Voigt circuit model containing a resistor in series with a resistor-capacitor parallel component, describing a semi-circle shifted along the real-axis. The equivalent circuit model allows us to quantify the resistance and capacitance of the low frequency arc (R_{LF}) for both materials under the two gas conditions. An Arrhenius plot of $\ln(R_{LF})$ as a function of inverse temperature is presented in Figure 5.1 (d). The values of R_{LF} decrease with increasing temperature, with the LSM-YSZ samples having lower values across the entire temperature range. Additionally, we see a slight decrease in the values of R_{LF} for LSM and LSM-YSZ at all temperatures, except for the highest temperature tested for LSM, 750°C. The decrease in R_{LF} suggests that there is a mechanism by which water improves the overall ORR on these materials. The limitations of EIS do not allow for identification of a specific mechanism to ascribe to the process. Gas phase oxygen isotope exchange is an *in-situ* technique capable of simultaneously probing exchange reactions for multiple gaseous molecules in a single environment.

1:1IIE experiments in the presence of water were performed on LSM-YSZ composite powders at temperatures ranging from 350-800°C. The concentration of O_2 gas was a total of 50,000ppm and the level of humidification was 3,000ppm for all of the experiments. Isotopologue concentrations are calculated using the corresponding mass/charge (m/z) signals measured from the reactor effluent with a quadrupole mass spectrometer (QMS). The m/z ratios for $^{16}O_2$, $^{16}O^{18}O$, and $^{18}O_2$ are 32, 34 and 36, respectively. D_2O (m/z=20) was used as the O_2 fragment peak from ^{18}O overlaps with the main peak for H_2O (m/z=18). Select exchange curves for 1:1IIE are shown in Figure 5.2 (a)-(c) at 350°C, 550°C, and 750°C, respectively. The exchange curves show the concentrations in ppm for the O_2 and D_2O isotopologues as a function of time. Time $t = 0$ is the switch from 50,000ppm $^{16}O_2$ with 3,000ppm $D_2{}^{16}O$ to a mixture of 25,000ppm $^{16}O_2$, 25,000ppm $^{18}O_2$, and 3,000ppm $D_2{}^{16}O$. The total concentration of O_2

and D_2O molecules is constant before and after the switch to maintain isobaric conditions. The exchange curves change as a function of time depending on rates of homogeneous and heterogeneous exchange.

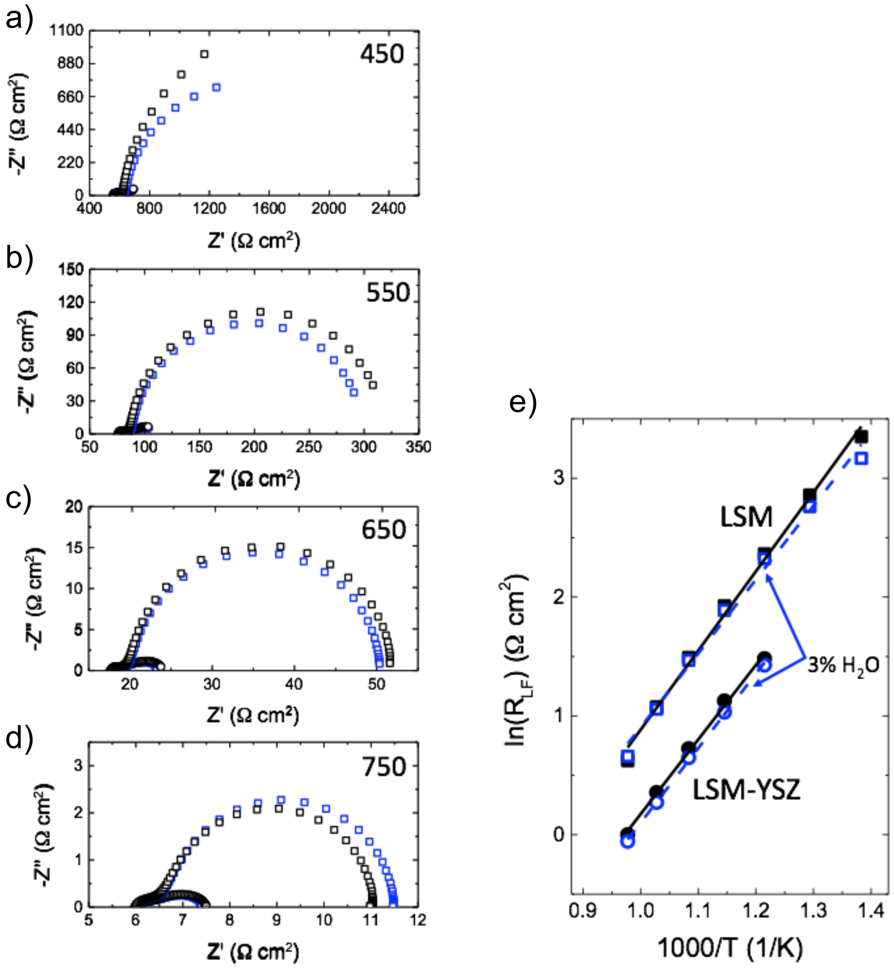

Figure 5.1: Nyquist plots for impedance measurements made on LSM (squares) and LSM-YSZ (circles) in dry (closed, black) and humidified (open, blue) environments at 450°C (a), 550°C (b), 650°C (c), and 750°C (d). Fitting the low frequency arc with a simple parallel resistor-capacitor circuit provides resistance values (R_{LF}) under each condition. The Arrhenius dependence of R_{LF} yields apparent activation energies for the process(es).

At 350°C, Figure 5.2, the starting concentrations of $^{16}O_2$ (black), and $^{18}O_2$ (blue) are very close to 25,000ppm, while the concentration of $^{16}O^{18}O$ (red) is close to zero. These values remain constant as the experiment moves toward steady state. Deviations from the inlet concentrations indicate higher rates of overall exchange. In Figure 5.2 (a) we can also see concentrations for the two water isotopologues $D_2{}^{16}O$ (pink) and $D_2{}^{18}O$

(green). Similar to the oxygen signals, the water signals start at their inlet concentrations, and do no change significantly as a function of time. The exchange curves at 550°C, Figure 5.2 (b), show different starting and ending concentrations than those observed at 350°C. The $^{16}O_2$ concentration at $t = 0$ is close to 35,000ppm while that of $^{18}O_2$ is near 15,000ppm. Similar to 350°C, the starting concentration of $^{16}O^{18}O$ is close to zero at 550°C. As the concentrations of $^{16}O_2$ and $^{18}O_2$ converge toward their starting values (and the inlet concentration) the measured signal for $^{16}O^{18}O$ increases. This same trend is observed for $D_2{}^{18}O$, initially starting at zero, and increasing in concentration with time. This trend continues at 750°C, where we see greater changes in concentration as a function of time, and higher steady state concentrations for $^{16}O^{18}O$ and $D_2{}^{18}O$.

The rate at which oxygen exchanges into the lattice can be calculated using Eq. 5.2, where the ^{18}O flux into the lattice is the difference between the inlet flux of ^{18}O atoms and those that are leaving the reactor in the form of the gaseous by-products $^{18}O_2$, $^{16}O^{18}O$, and $D_2{}^{18}O$. Figure 5.3 (a) is a plot of $J(t)$ versus exchange time for the range of temperatures tested. At the beginning of the experiment we can see the initial exchange flux increases with temperature, followed by a first order decay. Integrating the flux with respect to time, we can generate an oxygen accumulation curve, shown in Eq. 5.3, corresponding to the fraction of the different oxygen isotopes in the solid phase as a function of time. The maximum value from Eq. 5.3, once the system has reached steady state, indicates the effective portion of isotopic oxygen in the overall solid (λ_{latt}). The values for the lattice exchange fraction, λ_{latt}, are plotted in Figure 5.3 (b) for LSM-YSZ with and without the presence of water. For both sets of experiments, λ_{latt} increases exponentially across two separate temperature regions. It was determined previously[64] that the lack of vacancies and low O^{2-} conductivity in LSM at lower temperatures, resulting in incorporation into YSZ at lower temperature, followed by incorporation into LSM at higher temperature. 1:1 IIE performed with the presence of water shows lower values for λ_{latt} across the entire temperature range, but following the a very similar trend. One possible explanation is that the LSM-YSZ composite 'prefers' to heterogeneously exchange with water instead of oxygen across all temperatures. Under these conditions, the result would be a larger overall fraction of ^{16}O in the lattice coming from $D_2{}^{16}O$, instead of $^{18}O_2$, the only ^{18}O source.

$$J(t) = 2 * \left[2N_{36}^{inlet}(t) - 2N_{36}^{outlet}(t) - N_{34}^{outlet}(t) - N_{22}^{outlet}(t)\right] \quad [5.2]$$

$$M(t) = \int_0^t J(t)\,dt \quad [5.3]$$

In addition to lattice exchange fractions, we can also fit the flux curves to extract surface exchange coefficients, k_{ex}, at each temperature. Fitting of the flux curves is performed using:

$$J(t) = J_0\left(1 - \exp\left(-\frac{3k_{\mathrm{ex}}t}{a}\right)\right) \quad [5.4]$$

where a is powder radius and k_{ex} is the surface exchange coefficient. J_0 is the sum of both ^{16}O and ^{18}O exchange flux. The equation considers the case for which surface exchange is limiting the overall reaction, significantly decreasing the complexity of the general solution.[68] The results are plotted as $\ln(k_{ex})$ versus inverse temperature in Figure 5.3 (c), and are compared with previous results for 1:1IIE on LSM-YSZ without the presence of water. The presence of water appears to cause an increase in the values extracted for the surface exchange coefficient. A linear fit of the results yields a lower apparent activation energy for surface exchange, of ~30kJ/mol, as compared to ~36kJ/mol in a dry gas stream, indicating that the effect of water on oxygen exchange of LSM-YSZ is a function of temperature.

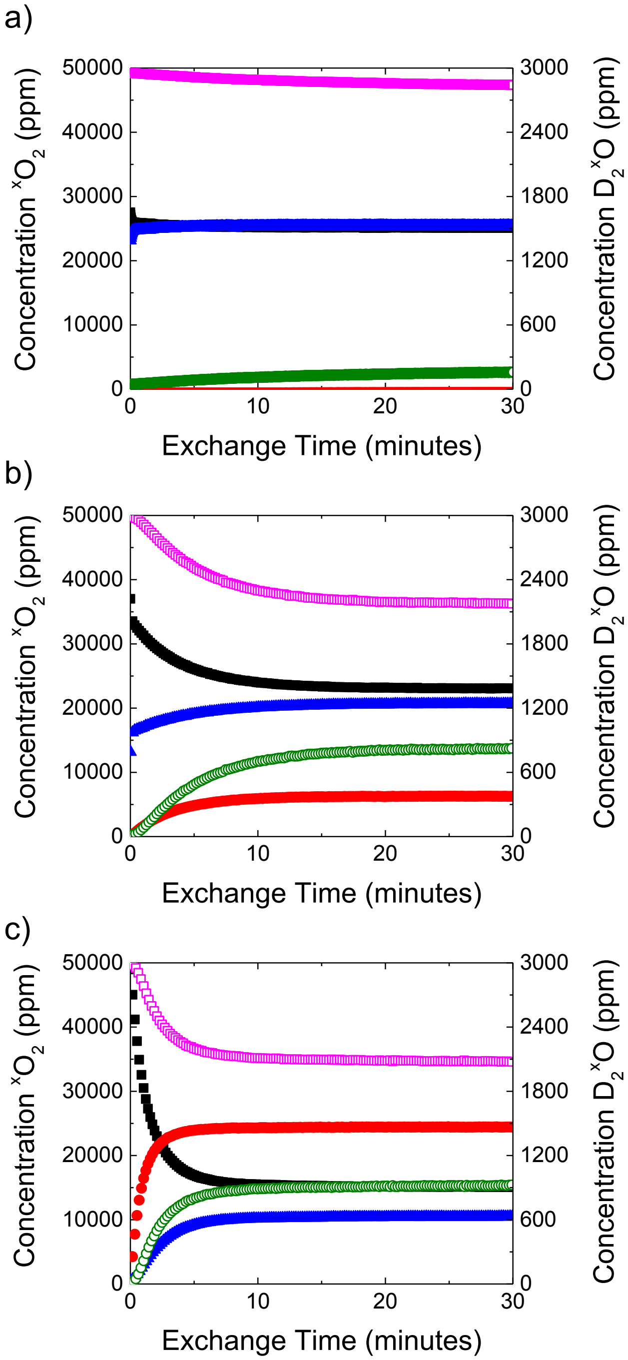

Figure 5.2: Exchange curves for O_2 (closed symbols, left axis) and D_2O (open symbols, right axis) at 350°C (a), 550°C (b), and 750°C (c). Concentration of the three oxygen isotopologues $^{16}O_2$ (black), $^{18}O_2$ (blue), and $^{16}O^{18}O$ (red), are calculated from their m/z signals 32, 36, and 34, respectively. The D_2O concentrations, $D_2{}^{16}O$ (pink) and $D_2{}^{18}O$ (green) are calculated from 20 and 22, respectively. The exchange curves are dependent on rates of homogeneous and heterogeneous exchange and are thus dependent on temperature.

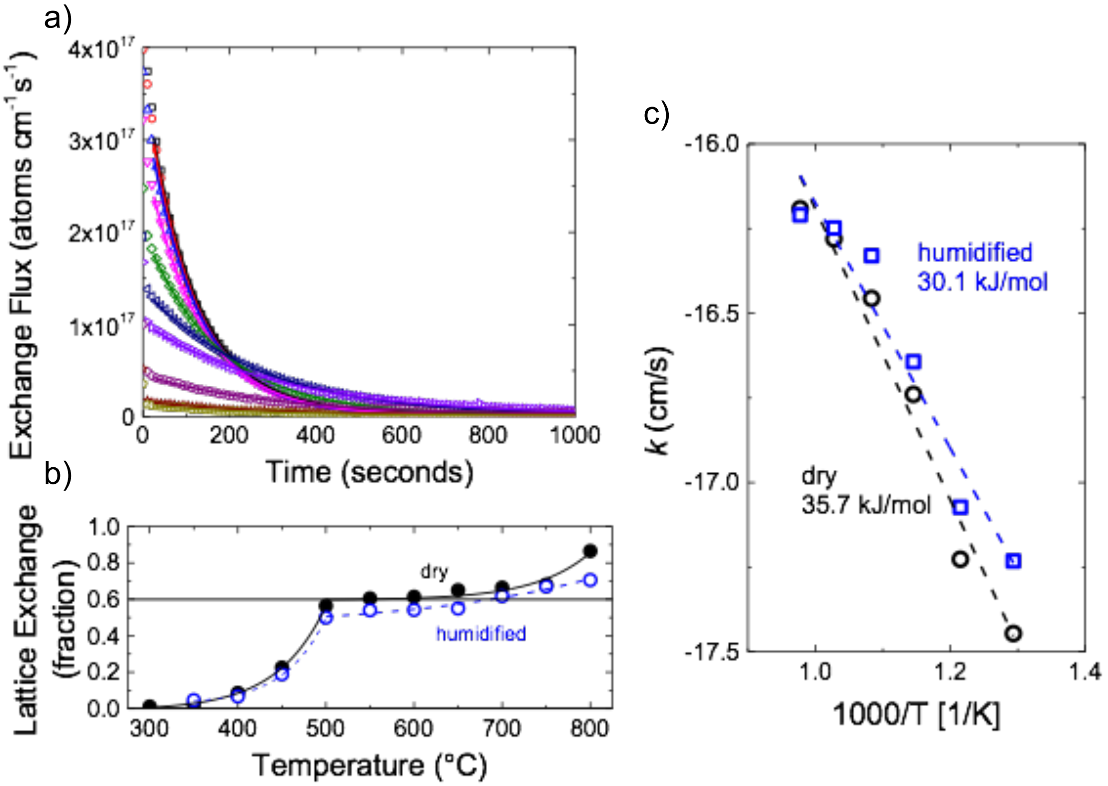

Figure 5.3: The flux of oxygen atoms into the lattice as a function of time (a). The flux can be integrated with respect to time (t) to generate an oxygen accumulation curve. The steady state value at the end of the accumulation curve divided by the total number of available sites provides the fraction of lattice sites that have been exchange (b). Fitting the flux curves with a simplified version of Crank's solution for diffusion in a sphere yields surface exchange coefficients at each temperature tested (c). At lower temperatures there is limited exchange and at higher temperature gas phase mass transfer limitations, resulting in unusable fitting results.

A major benefit of 1:1IIE over other isotope exchange techniques is the ability to differentiate dissociation from the other reaction steps in the overall process. The dissociation rates can be calculated based on the steady state values of $^{16}O^{18}O$ in the exchange curves. In Figure 5.2 (a)-(c) the $^{16}O^{18}O$ concentration is represented by the red symbols. We calculate r_{diss} using the final concentration, at 30 minutes, normalizing to mass flow rates and sample surface area. Figure 5.4 is an Arrhenius plot of values of r_{diss} for LSM-YSZ in humidified environments. Values for LSM-YSZ without humidification, and LSM, both with and without humidification, are plotted as well for comparison. For LSM, a humidified environment increases dissociation across the studied temperature range. In contrast, the effect of water on dissociation for LSM-YSZ is the opposite, where its presence decreases the overall dissociation rate. All four data sets yield similar activation energies based on linear fits from Figure 5.4. Activation energies in kJ/mol for LSM are 76 (dry) and 86 (humidified), and 87 (both dry and humidified) for LSM-YSZ.

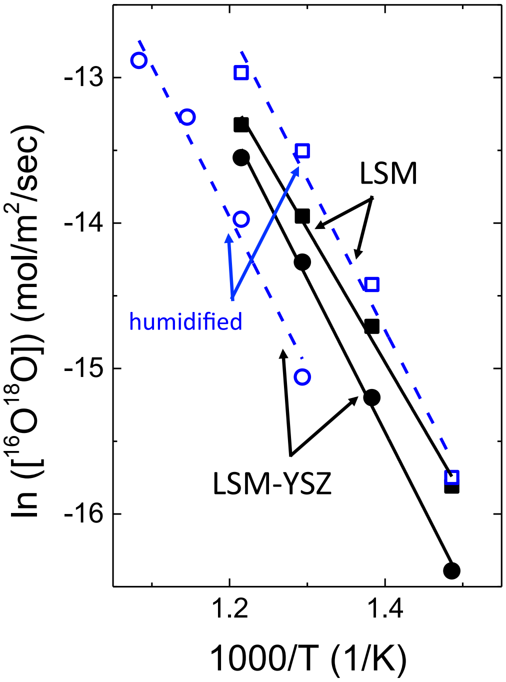

Figure 5.4: The rate of dissociation (r_{diss}) for LSM (squares) and LSM-YSZ (circles) as a function of temperature in dry (closed, black) and humidified (open, blue) environments. Rates are extracted from steady state values of $^{16}O^{18}O$ and $D_2{}^{18}O$. The values are plotted as ln(r_{diss}) vs. 1000/T and fit with lines to determine apparent activation energies. Humidity increases r_{diss} for LSM but decreases rates for LSM-YSZ composite. The presence of D_2O may decrease the role of TPB in dissociating O_2.

Comparing LSM and LSM-YSZ exchange in the presence of water, we can look at the residence time of D_2O in the system for the two materials. Using Eq. 5.5, we can fit the $D_2{}^{18}O$ exchange curves and extract values for τ, the mean residence time constant for D_2O exchange, as a function of temperature. The results for LSM are plotted along with those for LSM-YSZ, in Figure 5.5.

$$F^i(t) = \exp\left(-\frac{t}{\tau^i}\right) \quad [5.5]$$

where $F^i(t)$ is the normalized signal for water, and τ_i is the apparent time constant for water exchange. This apparent time constant normally describes the time required for water to equilibrate in the system and can be used to identify the rate-limiting-step in the overall water exchange. The odd dependence of τ on temperature for LSM is a result of a change in mechanism between surface dominated homogeneous exchange, and the formation of oxygen vacancies at higher temperatures. The result is a decreasing τ due to increased rates of homogeneous exchange between D_2O and O_2, followed by an increasing τ caused by heterogeneous exchange between D_2O and ^{18}O in the lattice, which we believe to depend significantly on oxygen vacancies. LSM-YSZ on the other hand shows a steady decrease in τ with increased temperature. This is likely caused by the relatively stable vacancy concentration in the composite, dominated by those in YSZ, and overall increases in the rates of exchange for both homogenous and heterogeneous exchange. Higher τ values for the composite as compared to LSM are thus a result of much greater heterogeneous exchange.

The above results give us some insight into how water exchanges on LSM-YSZ, and also affects molecular O_2 exchange on LSM-YSZ. In order to develop a more detailed picture, each material has to be considered individually. Previous results have shown that direct exchange of D_2O with O in LSM only occurs in a very limited temperature region under low PO_2 conditions. Similarly, heterogeneous exchange of O_2 on LSM on occurs above 650°C. A lack of coordinated surface vacancies, due to LSM oxygen super-stoichiometry, likely limits the incorporation of adsorbed oxygen, from both O_2 and D_2O. However, our 1:1IIE results show that the dissociation of O_2 on LSM,

Figure 5.4, increases in humidified environments. For YSZ, oxygen exchange is limited by dissociation. Heterogeneous exchange of water, on the other hand, has been shown by us and other authors to occur readily on YSZ, and is governed by dissociative-adsorption at surface vacancy sites, forming surface hydroxides (OH^-).[34,35,102,112–114] These results are very similar to those found for ceria (CeO_2).[115]

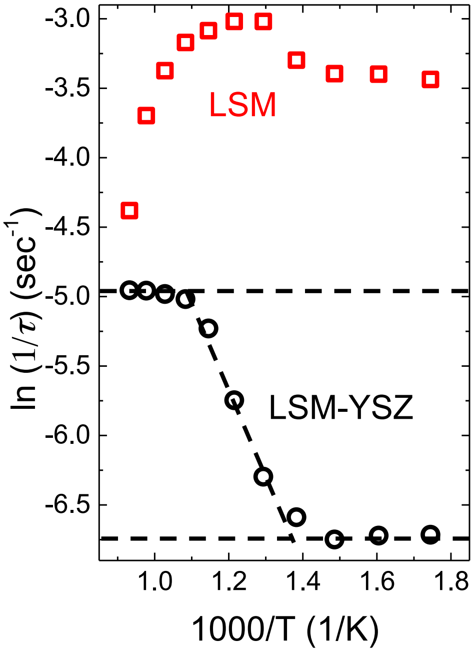

Figure 5.5: Arrhenius plot of time constant (*τ*) for water exchange on LSM (red square) and LSM-YSZ (black circle). The temperature dependent *τ* is a result of multiple surface reactions and the slowest reaction step should correspond to the *τ*.

Considering that O_2 dissociation on LSM increases in humidified environments, and that O_2 dissociation on LSM-YSZ composite under dry conditions is greater than LSM (per LSM surface area), we might expect that O_2 dissociation on LMS-YSZ under humid environments leads to an increase as well. Our results however, show that O_2 dissociation on LSM-YSZ decreases with the presence of D_2O. One possible explanation for such a result can be explained by the transport mechanism presented in Figure 5.6.

Under dry conditions, fast surface transport of adsorbed oxygen on LSM to the YSZ surface, leads to increased dissociation as compared to the same surface area of LSM alone. This surface transport effect is likely mitigated by readily adsorbed D_2O under humid conditions. The effect is depicted in Figure 5.6 through adsorbed hydroxyls blocking O-surface diffusion on YSZ. Based on the results presented here, and those in previous paper, we believe that these are the most likely mechanisms governing O_2 exchange in humidified gas environments.

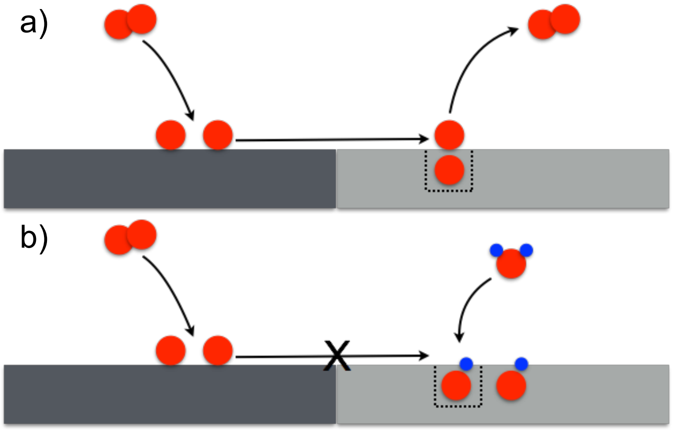

Figure 5.6: Mechanism describing O_2 and O_2-D_2O co-exchange on LSM-YSZ composite surfaces. (a) The increase of r_{diss} observed for LSM-YSZ composite is likely due to fast-surface diffusion of O-atoms from LSM onto the YSZ surface, where they can desorb into the gas phase. (b) Humidification of the gas stream causes blocking of the YSZ surface by stable hydroxyl groups (OH^-), preventing fast O surface diffusion from LSM to YSZ, decreasing r_{diss} as compared to the dry sample.

5.2 Conclusions

The technique 1:1IIE is able to simultaneously determine dissociation rates (r_{diss}) and in surface exchange coefficients for ion conducting materials and material systems. The *in situ* nature of 1:1IIE allows for observation of how O_2 interacts not only with the solid phase material, but also other O-containing molecules in the gas phase. The mechanisms governing O_2 exchange on composite LSM-YSZ in humidified gas environments have been proposed using results from gas phase oxygen isotope exchange. The role of surface hydroxyls adversely affects dissociation on LSM-YSZ composite, while the overall rate of heterogeneous exchange is improved. The results contribute to bridging heterogeneous catalysis and solid-state ionics.

Chapter 6: *in operando* Isotope Exchange

6.1 Introduction

SOFCs are exposed to a wide range of conditions during operation; including different temperatures, PO_2's, electrical loads, and exposure to a range of gas environments. Under these wide-ranging conditions, the chemical and physical properties of materials used in SOFC electrodes can change drastically, ultimately affecting their performance and durability. Therefore, it is imperative to characterize SOFC electrode materials under conditions close to those experienced during operation. There has been significant effort recently toward the development of *in situ* surface analysis techniques such as XPS, XAS, etc., aimed at characterizing solid oxide materials and electrodes at or near SOFC operating temperatures. At high temperature and with applied bias it has been shown that the surface electronic structure of MIECs can change significantly. The formation of oxygen vacancies, exsolution of cations are just a couple of the effects already observed in literature, leading to changes in transport kinetics and catalytic activity. The need for new *in operando* characterization methods to study solid oxide cells (SOCs) is perhaps best described by a recent transaction from Traulen et al. (2015). The authors highlight the current state of *in operando* for SOFC (SOEC) systems, and describe potential directions for future endeavors. This chapter describes the development of an *in operando* oxygen tracer experiment aimed at determining the effects of applied bias on oxygen reaction transport and kinetics on SOFC electrodes.

6.1.1 Isotope plus *in operando*

Gas phase oxygen isotope exchange is a technique that is capable of extracting fundamental kinetics rates for the oxygen exchange reaction. Although the parameters that can be extracted thus far using IIE (k_{ex}, r_{diss}, D*) can provide insight into the fundamental mechanisms that govern oxygen exchange, they are limited in their application to electrode materials under operating conditions. Ideally we would like to determine how these, and other important kinetic factors change when an electrode is exposed to an applied external field, a reducing gas environment, or exposure to secondary reactive gas species.

The *in situ* nature of gas phase oxygen isotope exchange makes it particularly well suited for testing under operating conditions. Here, we detail the development of *in operando* gas phase isotope exchange for characterization of oxygen reaction kinetics on electrodes under conditions mimicking those of SOC operation. In isotope exchange, isotopically labeled oxygen works as a tracer, providing information for the movement of oxygen on or in the materials. Based on the concentration profiles of each oxygen isotopologue in gas phase, the surface exchange kinetics can be back calculated. In *in operando* isotope exchange, where the external driving force is applied, the movement of oxygen under such conditions can probe the difference between OCV and under working conditions.

6.2 Experimental

The *in operando* sample was fabricated using a 3YSZ electrolyte tube (McDaniel Ceramics) and typical cell fabrication techniques. An LSM paste (Fuel Cell Materials) was coated around the outside of the tube using a scotch tape mask to control the electrode area and thickness. The LSM electrode (WE) was then sintered at 1300°C for 4 hours to decrease the total surface area and ensure good electrode/electrolyte contact. After sintering the LSM electrode the inside of the YSZ tube was painted with Pt paste (Heraeus) for a counter electrode. The Pt paste was fired at 900°C for 1 hour, creating a porous Pt counter electrode. Au mesh was used to contact the LSM electrode, and a Pt wire connected to the inside of the YSZ tube. The sample (LSM/YSZ/Pt) was then loaded into a quartz tube with custom three-way vacuum fittings.

A schematic of the *in operando* set-up is shown in Figure 6.1. In this schematic we can see the sample described above and how it fits into the overall experimental set-up. The working electrode (WE) and counter electrode (CE) gas environments are controlled using mass flow controllers, and the gas effluent from the WE is monitored using a quadrupole mass spectrometer (QMS). A Keithley 2400 is used to control an external applied potential (load) between the WE and CE. The most important aspect of the reactor/experimental design is that we are able to control the gas environment at the working and counter electrodes, in addition to an externally applied potential (load). To avoid any external electrochemical potential driven by the difference of oxygen partial pressure (ΔPO_2), mass flow controllers were used to maintain the same level of oxygen partial pressure in each side of YSZ tube.

The WE gas flow is fixed at 20 SCCM with a PO_2=0.05 atm., matching the PO_2 of the CE. Before each experiment, the sample were pretreated at 850°C for 30 minutes in normal isotope oxygen ($^{16}O_2$) to clean the sample surface and saturate the O-lattice sites with ^{16}O. Then the sample was cooled down to the experiment temperature. An external current was then applied using a Keithley 2400. After 30 minutes, once the system was at steady state, a pneumatic valve was used to switch half of the $^{16}O_2$ to $^{18}O_2$ with a 1000 ppm Ar tracer. As the total concentration of O_2 stays the same, we can consider the gas environment to be isobaric. The mass/charge ratios (m/z) of the oxygen isotopologues $^{16}O_2$ (m/z=32), $^{18}O_2$ (m/z=36), and $^{16}O^{18}O$ (m/z=34) were monitored using a QMS. *In operando* experiments were performed on the LSM/YSZ/Pt sample at different temperature and applied currents.

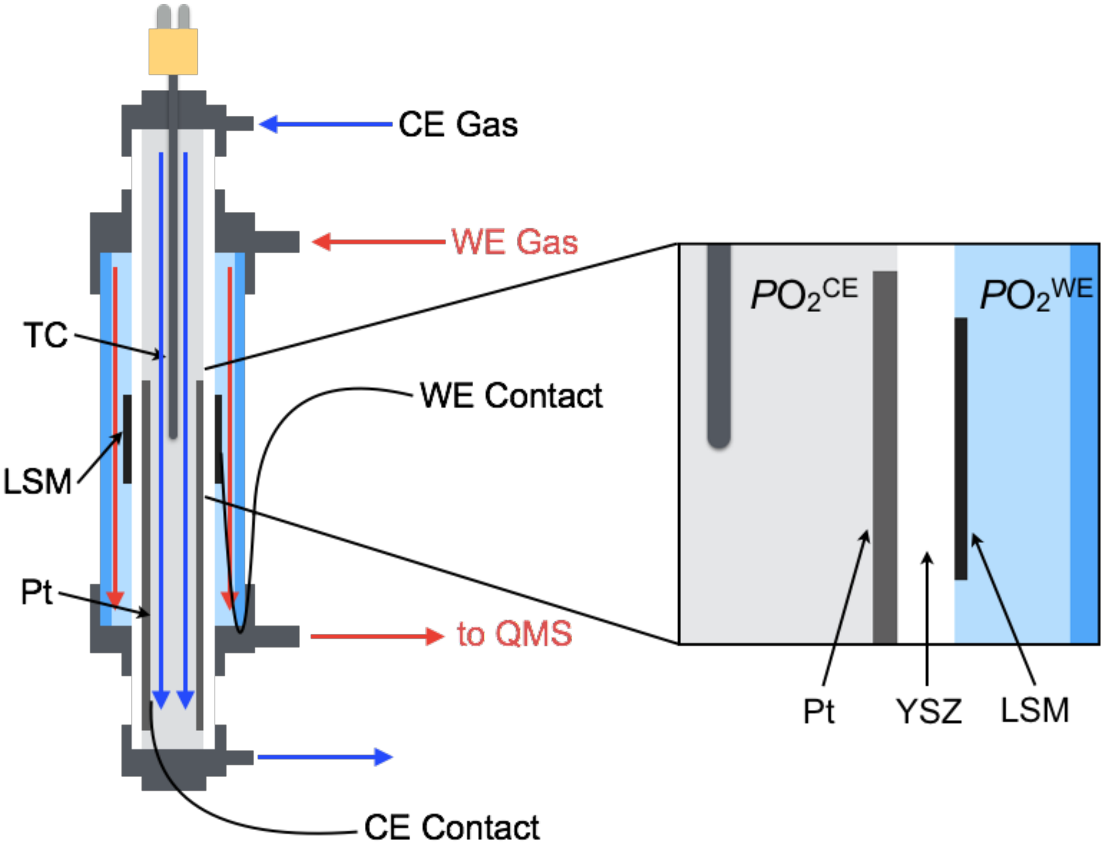

Figure 6.1: Schematic diagram of the *in operando* sample and reactor design. The sample consists of a tubular half-cell: an LSM WE is coated on a YSZ electrolyte tube, and the inside of the YSZ tube painted with porous Pt for a CE. The PO_2 of the WE and CE can be controlled using MFCs. The WE gas stream, capable of isotopic switching, is analyzed with a downstream QMS. The temperature of the sample is monitored and controlled with a TC inside the reactor.

6.3 Results

6.3.1 Impedance Spectroscopy

EIS measurements were performed on the LSM/YSZ/Pt *in operando* sample to obtain a basic understanding of the cell performance. Figure 6.2 is Arrhenius plots of the ohmic and non-ohmic impedances, de-convoluted from EIS spectra at different temperatures. The activation energy of the electrolyte conductivity, extracted from the ohmic resistance, yields values close to those for 3YSZ in literature[8] for both total conductivity and activation energy (76.5kJ mol^{-1}), as shown in Figure 6.2 (a). In Figure 6.2 (b) we see an Arrhenius plot of the cell ASR, which yields an apparent activation energy of 158.5 kJ mol^{-1}. This is well within the range of literature values for LSM electrodes, which can range from ~100-200kJ mol^{-1}.

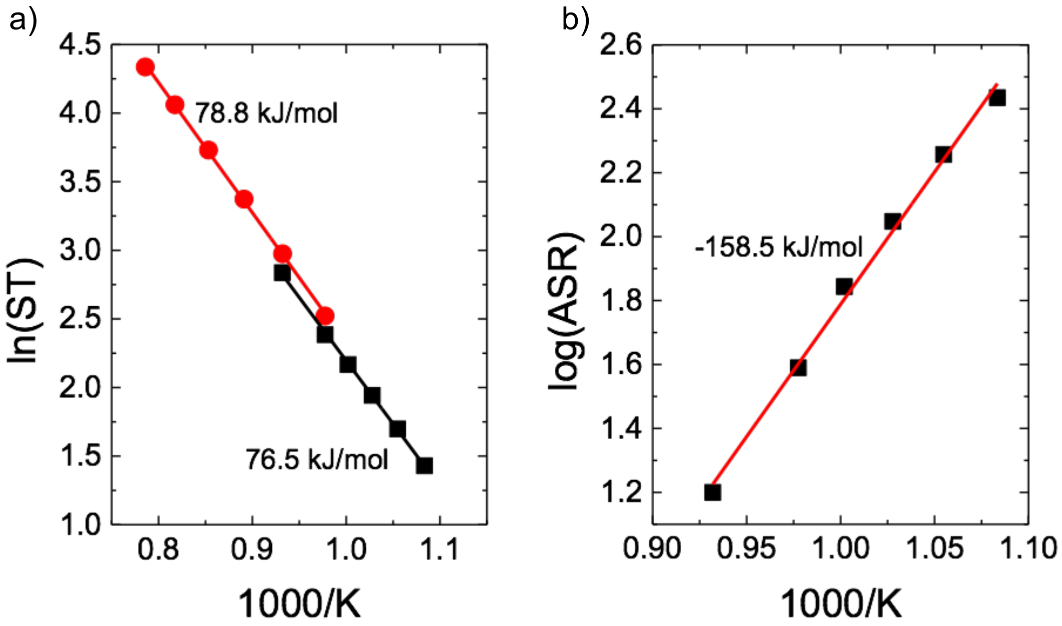

Figure 6.2: Electrolyte conductivity (a) and cell ASR (b) as a function of temperature from EIS measurements. The activation energy for the 3YSZ tube (black squares) is similar to literature values (red circles)[8].

Using the impedance data to remove the uncompensated resistance (resistance between RE1 and RE2 resulting from the electrolyte, the current-voltage data is plotted as log(i) versus overpotential (η), also known as a Tafel plot. Electrode overpotential was calculated based on the potential drop due to the non-ohmic portion of impedance.

According to Butler–Volmer equation, the slope of the best-fit line is proportional to the apparent charge transfer coefficient (α), while the intercept is the exchange current density (i_0):

$$i = i_0 \left[\exp\left(\frac{\alpha_a zF\eta}{RT}\right) - \exp\left(-\frac{\alpha_c zF\eta}{RT}\right)\right] \quad [6.1]$$

where z is the number of electrons involved in the reaction, T represents temperature, R is the universal gas constant and F is Faraday constant. Fitting the Tafel data, we extract values for α_c of 0.20 and 0.21 for 750°C and 650°C, respectively. Additionally, values for i_0 at 750°C and 650°C are 3.0 mA cm^{-2} and 0.2 mA cm^{-2}. The exchange current density can be compared to the surface exchange rate extracted from isotope exchange experiments.

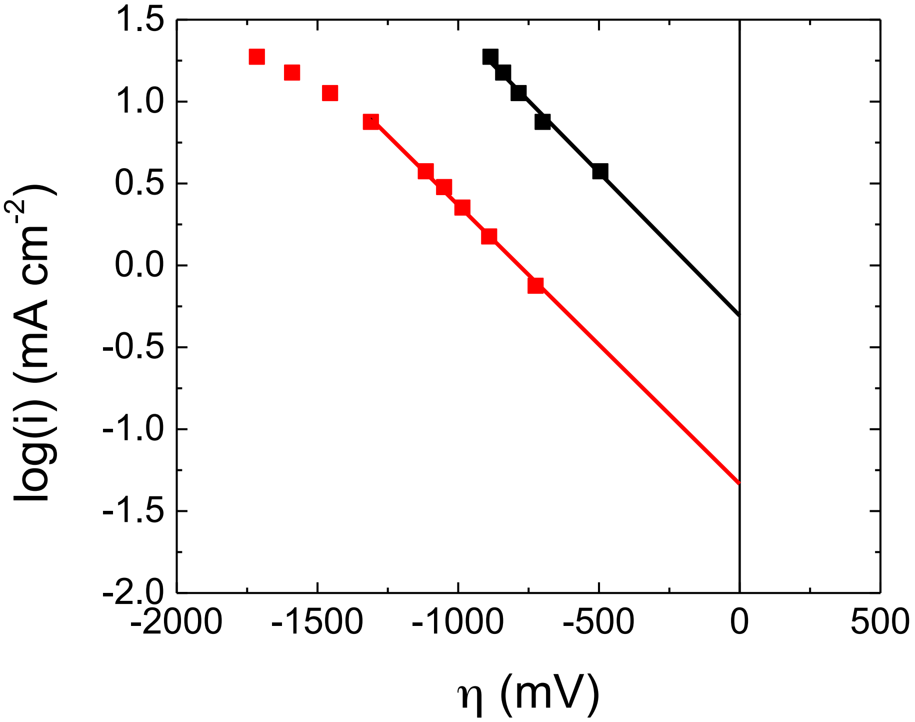

Figure 6.3: Tafel plot from EIS data showing the dependence of current density on electrode overpotential. The slope of the best-fit line is proportional to the apparent charge transfer coefficient (α), while the intercept is the exchange current density (i_0)

6.3.2 Current vs. PO_2

Changes in PO_2 were measured as a function of applied current at 750°C to determine basic characteristics of the *in operando* set-up. The results are presented in Figure 6.4 (a) and (b), where $\log(PO_2)$ is plotted versus applied current in (a) and versus the resultant voltage in (b). The voltages in Figure 6.4 (b) are measured and recorded once the cell has stabilized from the step-change in applied current. In the case of a positive current (voltage), the LSM WE is under an anodic polarization, e.g. the electrode is undergoing the oxygen evolution reaction (OER), and increasing the concentration of O_2 in the WE gas stream, which is the stream measured using the QMS. The opposite is true for a negative applied current; the LSM is undergoing the oxygen reduction reaction (ORR) driving oxygen into the CE gas stream.

The relationship between the oxygen flux and current can be established based on mass and charge balance according to:

$$J = \frac{i}{4F} \qquad [6.2]$$

where J is the oxygen flux (molecules s^{-1}), i is the applied current (A) and F the appropriate Faraday constant. We can compare the measured PO_2 to calculated values, shown as red circles in Figure 6.4 (a). The oxygen flux can be subtracted from the know flow rate (mol s^{-1}) from the mass flow controllers, and converted into a partial pressure. The measured PO_2 is comparable to the PO_2 calculated based on a flux balance, assuming one O^{2-} is passed through the cell for every two e^- that pass through the external circuit (no losses to recombination or electronic leakage). The $\log(PO_2)$ vs. cell voltage plot in Figure 6.4 (b) represents the overpotential losses associated with the LSM electrode in ORR and OER modes.

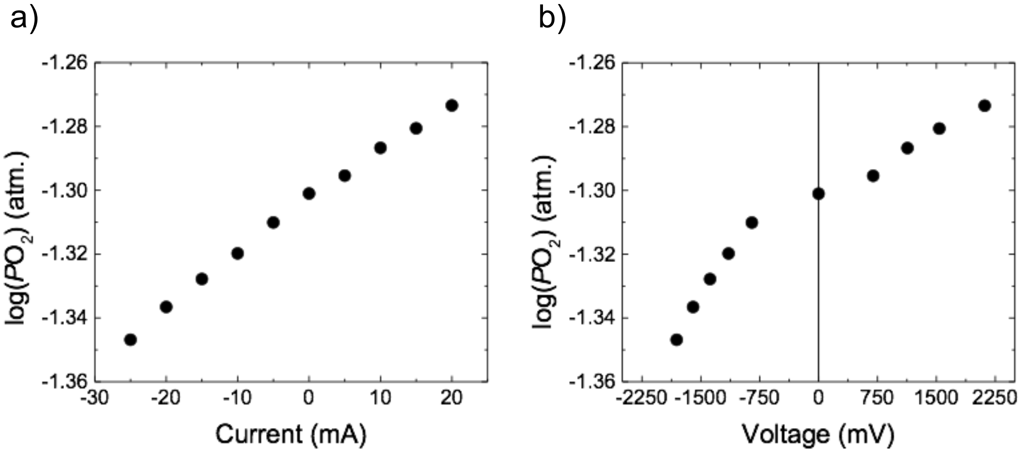

Figure 6.4: PO_2 as a function of (a) cell voltage and (b) applied current. The PO_2's are calculated based on the O_2 signal in the mass spectrometer. The PO_2 as a function of applied current has a linear relationship (oxygen flux), while the voltage-PO_2 relationship depends on the cell overvoltage.

6.3.3 Isotope Exchange Profiles

Isotope exchange measurements were performed under five polarization conditions. The conditions were selected such that a measurable change in PO_2 was observed. Figure 6.5 (a)-(c) shows the oxygen exchange curves for 1:1IIE on the LSM/YSZ/Pt *in operando* sample at 750°C under +5, 0, -5, -15, and -25 mA of current applied between the WE and CE. At time *t*=0, the gas feed stream for the WE is switched from 50,000ppm $^{16}O_2$ to 25,000ppm $^{16}O_2$ with 25,000ppm $^{18}O_2$.

Isotope exchange profiles can provide important information on two different aspects: steady state concentrations of each isotopologue and the transient signal response to the step change in isotope concentrations. The steady state concentration of each isotopologue describes the kinetic equilibrium at the gas-solid interface, and represents the fraction of exchanged vs. non-exchange O_2. The transient signals show the transport of ^{18}O into the solid phase and could be used to estimate the energy barriers for each reaction step.

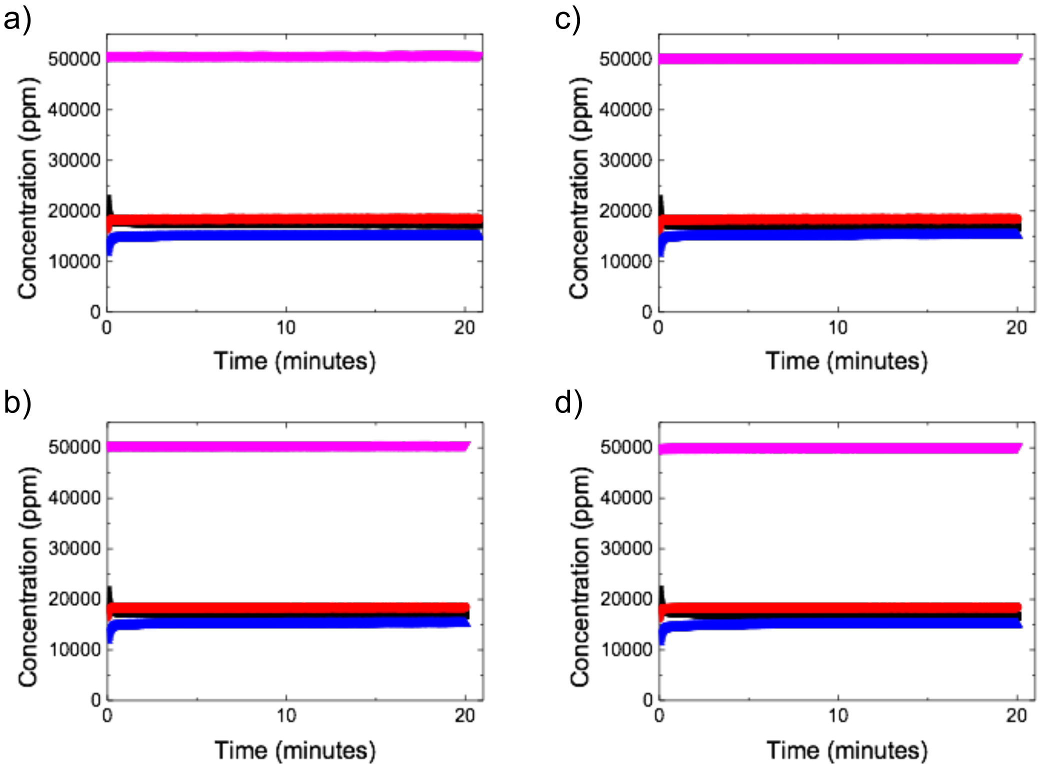

Figure 6.5: Isotope exchange curves at 750°C under applied current conditions at (a) +5mA, (b) -5mA, (c) -15mA, and (d) -25mA. The $^{16}O_2$ (black), $^{18}O_2$ (blue), and $^{16}O^{18}O$ (red) concentrations are shown as a function of exchange time. The total concentration of O_2 is shown in pink.

Using Eq. 4.1 we can calculate the oxygen flux, based on the number of ^{18}O atoms entering and leaving in the gas phase, leading to the flux plots in Figure 6.6 (a). The final steady-state flux values for Figure 6.6 (a) increase as a function of more negative current. That is, the flux of oxygen increases, the more reducing the polarization. Oxygen can be pumped in or out based on the applied bias. Normalizing to the steady-state flux during 0mA polarization, the "current-free" flux, we get the flux curves shown in Figure 6.6 (b). This leads to steady-state flux values that are derivative of the applied current through the sample. In this plot we can see that for the +5mA sample we observe a net negative flux, resulting in an increase in the total amount of oxygen on the WE side of the cell. In this case, the LSM electrode is in an OER regime. For the negative biases, the higher the bias, the greater then steady state flux value.

Finally, we can subtract out the effects of current, leaving only the flux we would normally calculate for 1:1IIE under no applied bias. It helps here to make a distinction between the total flux, and the flux due to isotope exchange, or what we will call exchange flux. The exchange flux is what would typically be observed for an isotope exchange experiment, where the net concentration of O_2 remains constant both before and after the switch to an isotopically labeled gas stream. For an *in operando* experiment there is an additional flux that is caused by the application of a current, driving O^{2-} either into (positive) or out of (negative) the WE gas stream, through the YSZ electrolyte. As such, we consider that the total oxygen flux is a sum of the "current flux" (J^c) and the "exchange flux" (J^{ex}), an approach used by Fleig et al.[116,117] A plot of J^{ex} for the different applied currents is shown in Figure 5 (c). Subtraction of J^c leads to very similar flux curves for all of the samples, showing just slight differences as a function of time. Integrating the flux curves we get ^{18}O accumulation curves, showing the total amount of ^{18}O that has accumulated in the lattice. The accumulation curves corresponding to the flux curves in Figure 6.6 (a)-(c), are shown in Figure 6.7 (a)-(c). The flux based on raw and 0mA normalization leads to accumulation curves that increase linearly as a function of time as a result of J^c. This is not the case for Figure 6.7 (c), where the flux has been normalized to the applied current. We can see in Figure 6.7 (c) accumulation curves very similar to those acquire under no applied current.

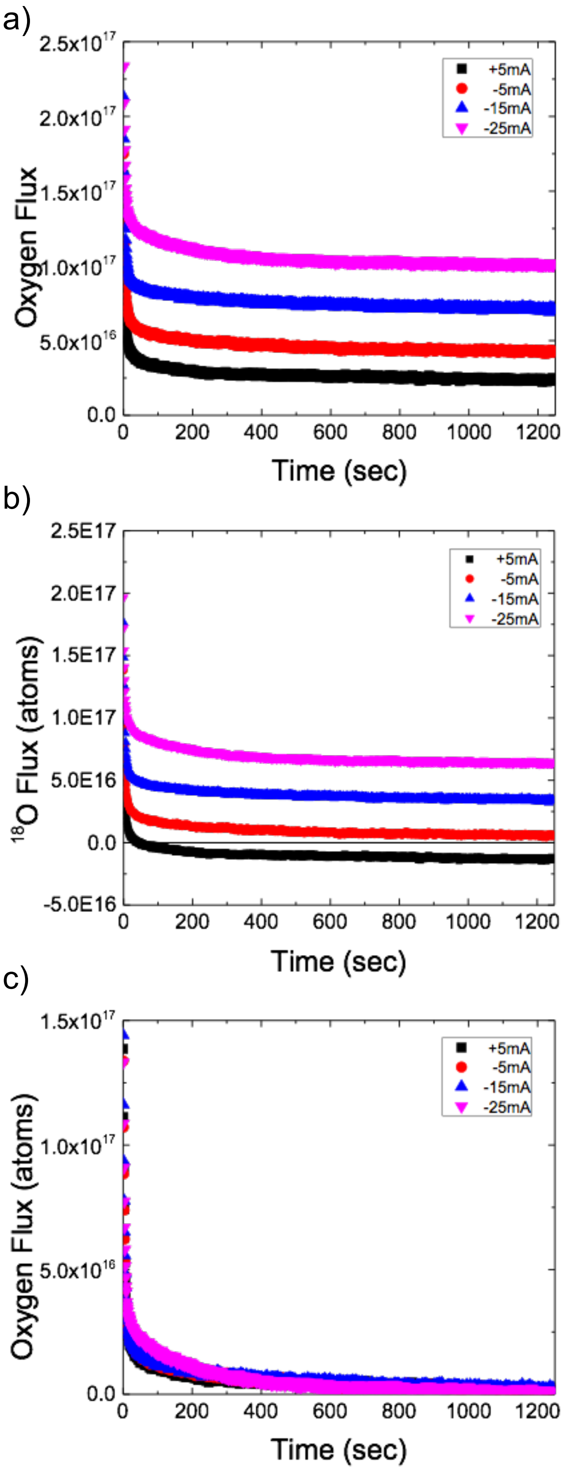

Figure 6.6: Flux curves for isotope exchange under various applied currents. The three sets of flux curves are for (a) flux without normalization to current, (b) subtraction of steady-state open circuit exchange flux, and (c) subtraction of steady-state value for each applied current.

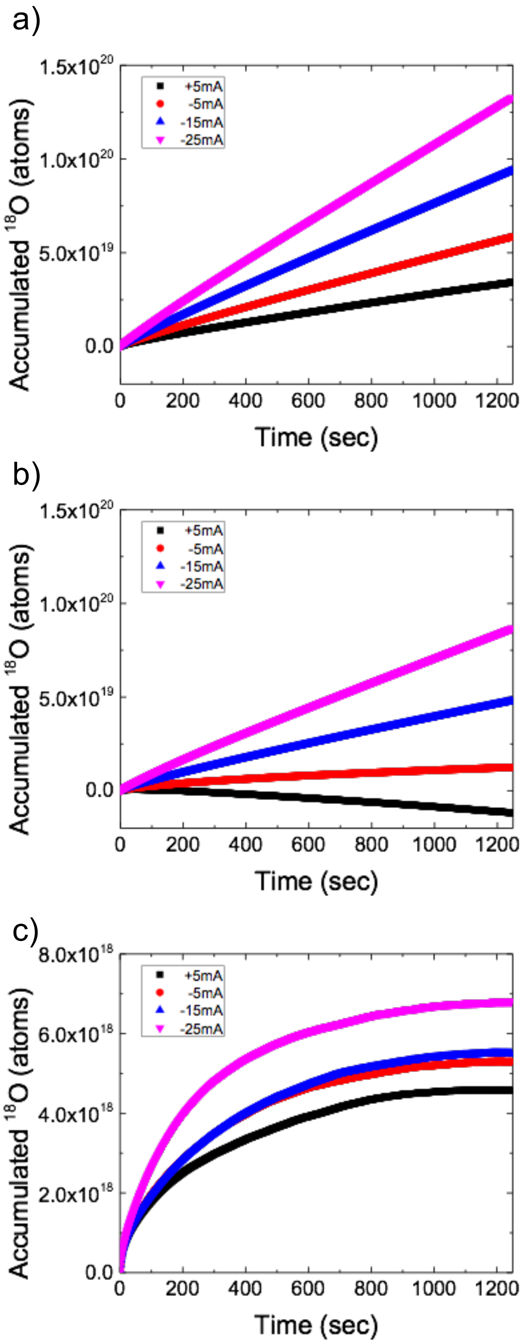

Figure 6.7: Oxygen accumulation curves calculated by integrating the exchange flux with respect to time. The accumulation curves (a), (b) and (c) correspond to the flux curves in Figure 6.6 (a), (b) and (c), respectively. The slope of the end of the accumulation curve in (b) is representative of the oxygen flux resulting directly from applied current.

Considering the boundary conditions of the system, we can fit the J^{ex} curves based on Crank's solution for diffusion into a semi-infinite plane:

$$C'(x,t) = \frac{C(x,t) - C_{bg}}{C_g - C_{bg}} = \mathrm{erfc}\left[\frac{x}{2\sqrt{Dt}}\right] - \left[\exp\left(\frac{kx}{D} + \frac{k^2 t}{D}\right) \mathrm{erfc}\left(\frac{x}{2\sqrt{Dt}} + k\sqrt{\frac{t}{D}}\right)\right] \qquad [6.3]$$

where $C(x,t)$ is the fraction of ^{18}O, C_{bg} is the background signal for ^{18}O, and C_g is the concentration of isotope entering the system. Additionally, x, t, k, and D are distance into the bulk, time, surface exchange coefficient and diffusion coefficient, respectively. If we consider that we are observing the fraction of ^{18}O on the surface as a function of time, where x=0, we can simplify the equation to:

$$C'(0,t) = 1 - \exp\left(\frac{k^2 t}{D}\right) \mathrm{erfc}\left(\mathrm{k}\sqrt{\frac{t}{D}}\right) \qquad [6.4]$$

Eq. 6.4 describes the change in concentration of ^{18}O on the surface of the sample, which we assume to be represented by the gas phase concentration. Using estimated literature values for the diffusion coefficient for YSZ[8], D=8.9x10^{-13}, we fit the normalized isotope fraction from 0 to 1 based on J^{ex}, using Eq. 6.4. The experimental data and fitting results are shown in Figure 6.8 (a)-(d). The values for k_{ex} as a function of applied bias are shown in Figure 6.9. The surface exchange coefficient decreases slightly with increasingly negative current, with the +5mA sample having the highest surface exchange coefficient. This result is consistent with recent findings by Chueh et al.[118] using AP-XAS on La-transition metal perovskites. They suggest that during redox reactions, the lattice anion plays a significant role in electron transfer to adsorbed O_2 molecules. Therefore, under conditions where the anion concentration on the surface is increased for LSM, the surface exchange rate may be expected to increase as well through faster electron transfer.

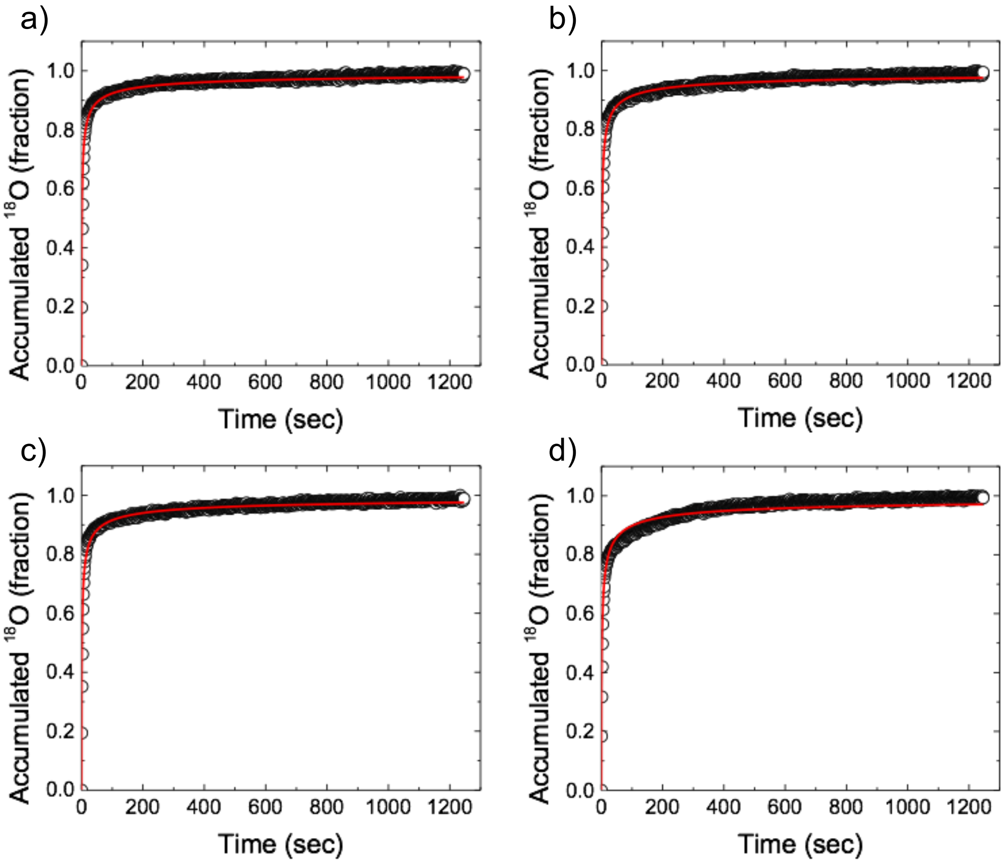

Figure 6.8: Data for normalized oxygen accumulation curves (black cirlces) at (a) +5mA, (b) -5mA, (c) -15mA, and (d) -25mA. The best-fit line from Eq. 6.4 is shown in red.

The steady state concentrations are a result of multiple bias effects on the system, including the increase/decrease of dissociation and incorporation rates. Polarization can change the surface features of LSM, leading to changes in surface catalytic properties. Additionally, it may alter the energy barriers for the ORR. Changes of steady state concentrations are the sum of these individual effects. If surface catalytic activity increases we would expect the $^{16}O^{18}O$ signal to increase, as it is an indicator for surface dissociation. However, once incorporation increases, the total concentration of $^{16}O^{18}O$ decreases, leading to the opposite results. Therefore, knowing the change of $^{16}O_2$, $^{16}O^{18}O$, and $^{18}O_2$ signals as a function of cathodic or anodic bias can help us elucidate the applied bias effect on each reaction step. Dissociation rate as a function of applied current density is shown in Figure 6.10. The dissociation rates were calculated by considering the fraction of oxygen that incorporates due to current (steady-state flux) and the fraction of $^{16}O^{18}O$ that evolves from recombination The dissociation appears to increase with increasing cathodic bias, and that the dissociation rate of LSM depends linearly with the applied current. However, the linear dependence may only occur at high overpotentials, and measurements at overpotentials near open circuit may yield a different result. This is the first time that the dissociation rate of these materials under polarization has been quantified, with a slope of 2.7×10^{14} (molecules sec^{-1} mA^{-1}). The outlying data point for the open circuit measurement is likely a result of calibration error for the 34 m/z signal.

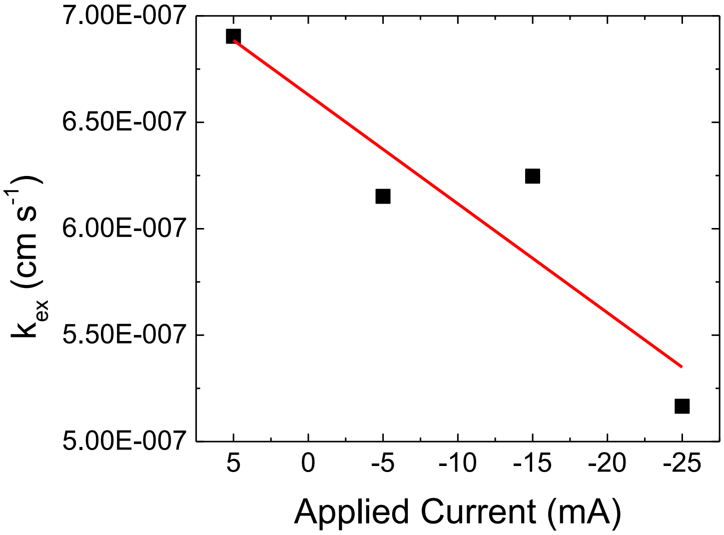

Figure 6.9: Values for k_{ex} for the best-fit lines shown in Figure 6.8 as a function on applied current. The surface exchange coefficient decreases as a function of increasing negative bias.

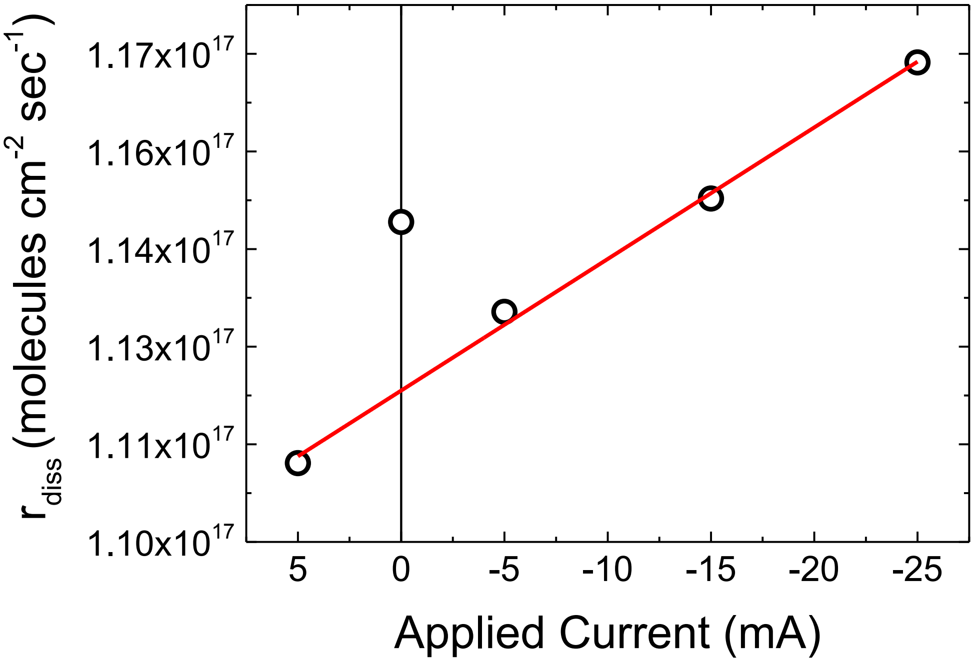

Figure 6.10: Dissociation rate as a function of applied current. The dissociation appears to increase with increasing cathodic bias. The outlying data point for the open circuit measurement is likely a result of calibration error for the 34 m/z signal.

6.4 Conclusions

The design and results of an *in operando* gas phase isotope exchange experiment has been presented. The experimental design allows for measurement of isotope exchange on electrochemical cells at temperatures and gas conditions analogous to those observed in realistic working conditions. Using a simple model we separate the oxygen flux into two parts; one ascribed to the direct role of an applied current J^{c}, and the second directly related to the exchange flux typically associated with oxygen isotope experiments J^{ex}. This allows us to directly determine the affect of applied current on exchange caused by a fundamental change in the materials properties. These changes are likely related to charged species, such as oxygen vacancies or the oxidation state of Mn. Additionally, the rate of dissociation as a function of applied bias at 750°C was determined. The results open a doorway to a new and exciting class of experiments that can directly observe the kinetic properties of electrochemical cells under operating conditions.

6.5 Future Work

Fundamental understanding is limited by sample knowledge in this case. A well-defined or simple cathode microstructure would increase the accuracy of results. Microstructure has a large impact on the extracted kinetics. Addition of a reference electrode would allow more in-depth impedance analysis. Ultimately, the electrochemical measurements can be compared to gas-phase analysis.

Chapter 7: Performance and Degradation of Stabilized Bi_2O_3 Electrolytes and Composite Cathodes

7.1 Introduction

Delta-phase bismuth oxide (δ-Bi_2O_3) has the highest known oxygen ion conductivity of any fuel cell electrolyte. At high temperature Bi_2O_3 has a fluorite structure (cubic, CaF_2) in which ¼ of the anion sites are vacant, creating a large number of carriers for O^{2-} transport. This conductivity however, is limited to a narrow temperature window (~730-825°C) above which the melting temperature of the material is reached, and below which a phase transformation to multiple phases, including monoclinic α-Bi_2O_3, tetragonal β- Bi_2O_3, and bcc γ-Bi_2O_3, occurs. Over the course of the past 50 years, there have been many attempts to stabilize the high conductivity cubic phase with varying success. Typically, researchers have doped Bi_2O_3 with rare earth elements in the Lanthanide (Ln) series, and a few other select dopants including, the alkaline earths Sr and Ca, along with some transition metals. Stabilization of the cubic phase to room temperature is accomplished primarily through the use of the heavy lanthanides (Dy through Yb) as well as Y, at relatively high dopant concentrations (~15-40%). Stabilizing δ-Bi_2O_3 using this approach brings with it two main drawbacks; the intrinsic conductivity of δ-Bi_2O_3 decreases with increasing doping concentration, which is near 15% on the low end, and although the cubic phase can be stabilized all the way to room temperature an oxygen-ordering phase transformation occurs at temperatures <650°C resulting in a drop in conductivity of ~1 order of magnitude. In the doped system, oxygen vacancies order along the <110> and <111> directions, leading to an ordered super-lattice with low oxygen conductivity.[119] It is believed that the oxygen ordering phenomenon is related to the bond strength between lattice oxygen and the dopant, where the rare earth-oxygen bond, RE-O, is stronger than that of Bi-O.

7.2 Ordering Kinetics in $Er_{0.4}Bi_{1.6}O_3$

Previously, researchers investigated ordering in stabilized bismuth oxide in relation to the type and amount of dopant in the material.[120–124] Jiang et al.[121] and Fung et al.[120] explored ordering kinetics for Ln-Bi_2O_3 systems containing rare earths Dy through Yb and found that the rate of ordering depends strongly on the dopant radii as well as dopant concentration. As the cation radii increased (Yb toward Dy) the time constant (τ) for ordering increased. The authors also found that the concentration of the dopant (x) in $(Er_2O_3)_x(Bi_2O_3)_{1-x}$ changes the rate of ordering in the system, where increased values for x, from 15-25 mol %, increased τ. These results also lead to the conclusion that the structures lattice parameter alone does not control ordering kinetics.[121] Therefore, τ should be a function of material properties, such as grain size or impurity concentration.

Here, the effect of sintering time on 20 mol % erbium stabilized bismuth oxide (20ESB) ordering kinetics was investigated using techniques similar to those found in previous studies. $Er_{0.4}Bi_{1.6}O_3$ was prepared using solid-state methods. Er_2O_3 and Bi_2O_3 (Alfa-99.999 pure) powders were mixed by ball milling in ethanol with yttria stabilized zirconia media. The powders were then calcined at 800°C in air for 2 hours. After calcination, the powders were ground and pressed into pellets in a 8mm die. The 20ESB pellets were then fired at 890°C for varying lengths of time.

Once sintered, the 20ESB pellets were polished and Au paste painted on both sides and dried in a 70°C oven. The samples were then loaded into a custom built reactor and heated to 750°C to fire the Au paste. Afterward, the samples were cooled to the aging temperature and impedance spectroscopy measurements acquired every 10 minutes. The high-frequency intercept of the impedance spectra, representing the ohmic resistance, was used to calculate the conductivity of the sample.

7.2.1 Effect of Sintering

Conductivity at 600°C as a function of time for 20ESB pellets sintered for 4, 20, 40 and 100 hours is shown in Figure 7.1. Each sample shows a similar conductivity at time t=0 when the sample first reaches 600°C. This value is stable for the first 25 hours, at which time we start to see decay in conductivity for some of the samples. Each sample appears to have a different rate of conductivity decay, eventually leading to a stable, final conductivity that is similar for each sample.

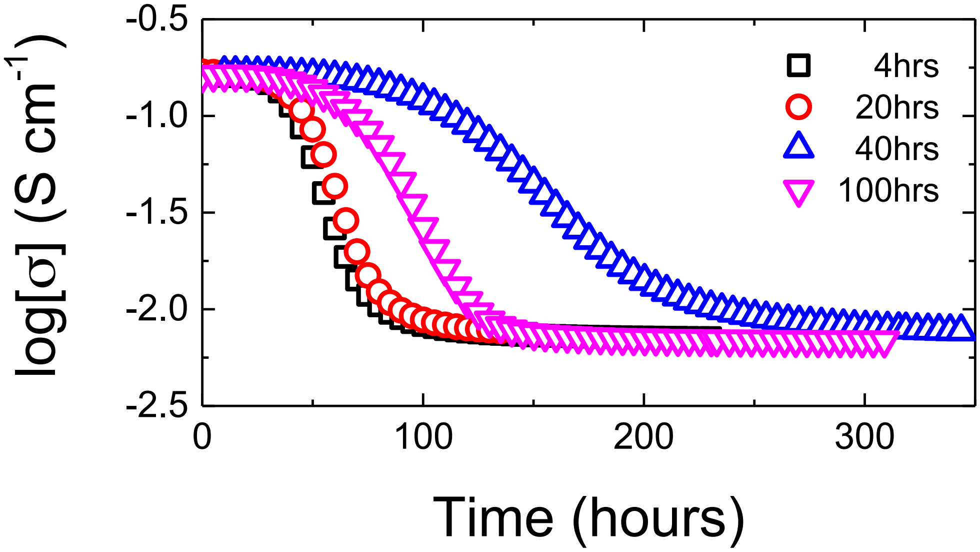

Figure 7.1: Conductivity as a function of time for 20ESB samples sintered at 875°C for 4, 20, 40 and 100 hours. Impedance measurements were performed at 600°C Each sample shows distinctly different total times for conductivity decay, an effect of the ordering kinetics in the material.

Analysis of the ordering rate was performed using the Avrami equation[125], Eq.

7.1, which generally describes the kinetics of phase transformations in solids based on a nucleation and growth mechanism. In the Avrami equation, *x(t)* represents the phase fraction of the growing phase in the material, t is time, and τ is the growth rate time constant of interest. Additionally a dimensional parameter m describes the direction(s) the secondary phase grows in the sample and the mechanism (diffusion or interface) by which it occurs. The value of m can range from 1 to 5 according to the dimensions of growth mechanism. The ordered fraction, $x(t)$, as a function of time, for ESB sintered for 20 hours is plotted in Figure 7.2. The concentration of charge carriers, $[V_O]$, does not change during order-disorder transition, and the only change is the energy barrier for the oxygen transport from the order or disorder state. Therefore, order-disorder fraction can be related directly to log of conductivity, yielding a symmetrical "S" shape for the ordered fraction as a function of time, a characteristic of phase-transformation kinetics.

$$x(t) = 1 - \mathrm{e}^{\left(\frac{t}{\tau}\right)^{m}} \qquad [7.1]$$

Solving for t in Eq. 7.1, we acquire a log-log dependence which can be used to solve for τ by plotting $\ln\ln(1/(1-x(t)))$ versus $\ln(t)$. These plots for samples sintered at different temperatures are shown in Figure 7.3. A linear fit of the data in Figure 7.3 provides a slope, m, and an intercept, where the intercept is equal to $-m\ln(\tau)$. Using this relationship we can extract time constants for each sample, and plot the dependence of τ on sintering time for ESB pellets, Figure 7.4. In Figure 7.4, the ESB sample sintered for 40 hours appears as a clear outlier. Future work characterizing the sintered pellets may yield the relationship between ordering kinetics and sintering time.

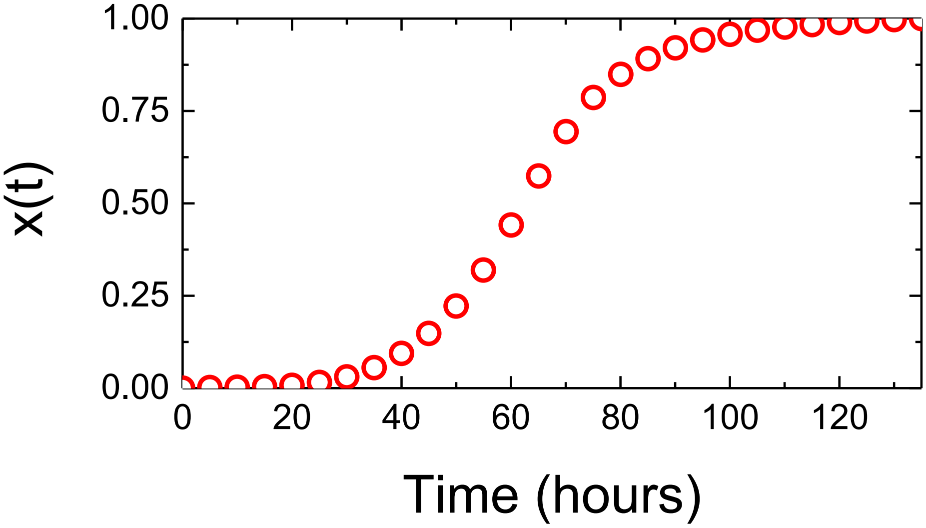

Figure 7.2: The ordered fraction in 20ESB sintered for 20 hours as a function of time. Calculated by normalized log(σ) from 0 (disordered) to 1 (ordered). The trend has a distinct "S" shape, a feature that is characteristic of phase-transformation kinetics.

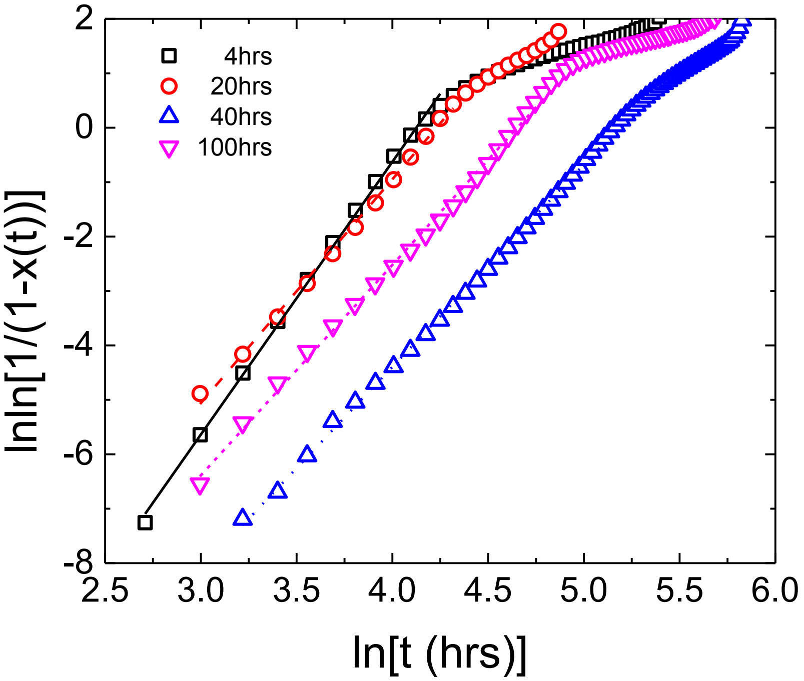

Figure 7.3: Using the Avrami equation to describe the kinetics of the disordered-ordered phase transformation. Plotting the double natural log of the ordered fraction, lnln(1/(1-*x*)), as a function of ln(*t*), the slope, *m*, describes the order of the reaction in terms of the number of dimensions for growth, and can be used to calculate a time constant for the process.

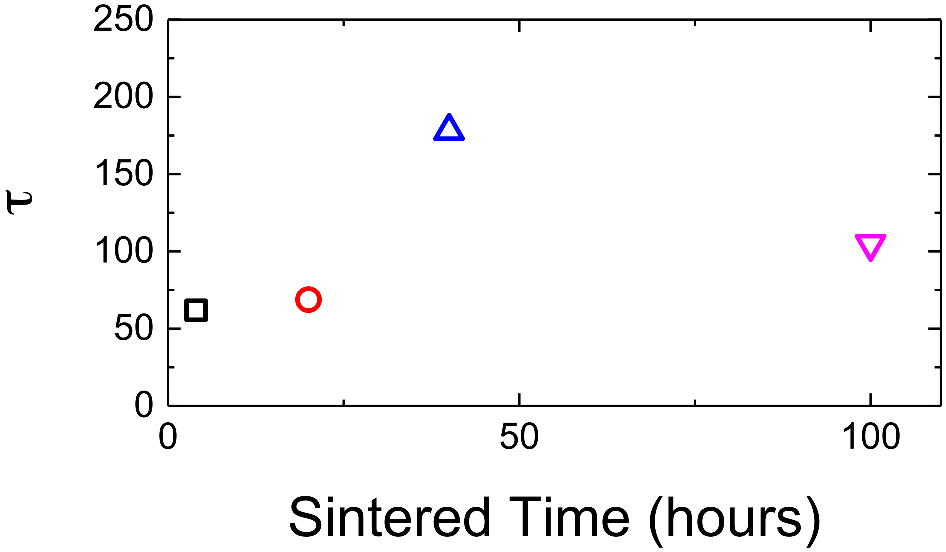

Figure 7.4: The ordering time constant, τ, for 20ESB samples sintered for different lengths of time. The time constants are extracted using the Avrami equation.

7.3 Degradation of $Er_{0.4}Bi_{1.6}O_3$ for Bi-Layer Electrolytes

The use of 20ESB in bi-layer electrolytes has provided some renewed interest in their potential use. It is well known that under reducing PO_2 (~10^{-13} atm.) that bismuth oxide undergoes reduction and forms Bi-metal. The melting point of Bi-metal is 271.4°C, making this reduction irreversible. Therefore, the typical reducing atmospheres reached at the anode side of an SOFC (~$PO_2 = 10^{-20}$ atm.) will cause rapid growth of Bi-metal and subsequent electronic shorting in the cell. In a bi-layer configuration, two electrolyte materials are combined where each material is exposed only to either the air or fuel side of the cell. It is well knows that GDC has small amounts of n-type electronic conductivity do changes in Ce oxidation state. The addition of a Bi_2O_3 electrolyte layer on the cathode side provides an electronically blocking layer that is not exposed to highly reducing conditions, increasing the OCV of the cell, and the drop in electronic leakage from GDC leads to an increase in the power output of the cell.

7.3.1 Effect of Humidity on Performance and Stability

The effect of humidity on 20ESB was explored for its potential use in bi-layer electrolyte applications. It is well known that degradation of cathode materials can occur due to reactions cause by exposure to the naturally occurring humidity in ambient air. As 20ESB is a proposed air-side material for a bi-layer fuel cell, it is necessary to understand any possible degradation issues caused by humidified environments. Previously, Huang et al. studied the effects of water on 25 mol % Y_2O_3 stabilized Bi_2O_3.[126] It was found that submersion of 25YSB pellets in water at 50°C causes decomposition and the growth of $Bi_2O_2CO_3$ and $Y(OH)_3$ crystals. To further explore the affect of humidity on samples under operating conditions, exposure to ESB cells at higher temperatures was performed.

Isotope exchange was used initially to probe exchange between gaseous water and ESB powder samples, to identify particular exchange temperatures. A temperature profile for oxygen exchange on ESB was acquired using ISTPX, shown in Figure 7.5. The oxygen exchange profile shows that exchange on ESB begins at 200°C and continues, at an increasing rate through 750°C. This increasing rate of water exchange with 20ESB as a function of temperature differs from exchange that was seen for previously tested electrolytes (YSZ and GDC), where exchange reached a maximum around 300°C and then decreased with increasing temperature. A decrease in D_2O residence time on the material surface can cause decreased exchange at increasing temperatures. However, the increasing rate of exchange on 20ESB as a function of temperature indicates an alternate exchange mechanism and possibly a different D_2O-surface bond.

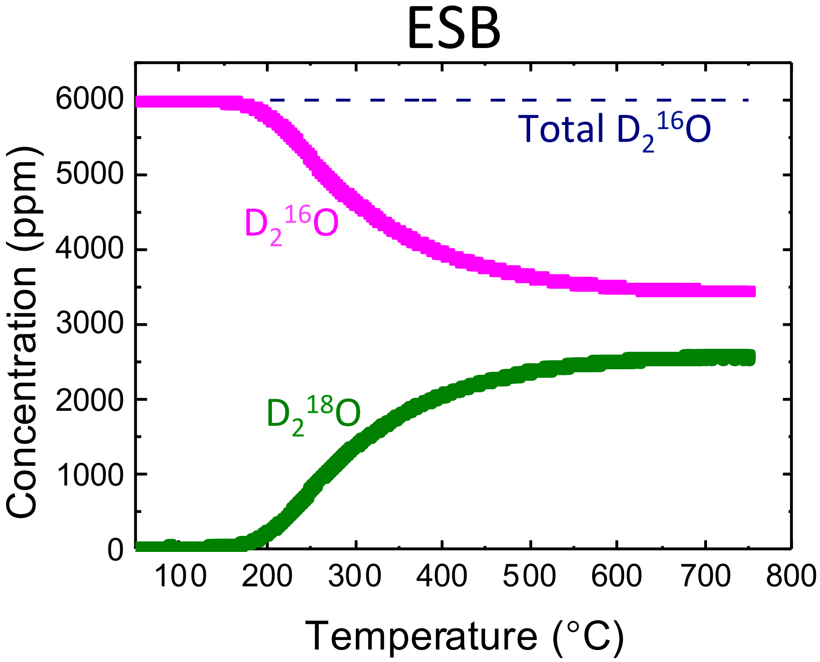

Figure 7.5: ISTPX exchange curves for 20ESB in the presence of D_2O balanced in He. 20ESB shows exchange with D_2O starting at ~200°C and increases with increasing temperature. It appears that at ~700°C a maximum level of exchange is reached.

Based on isotope exchange results, EIS was performed on ESB aged in water at different temperatures. The stability of 20ESB in humidified air atmospheres was tested under a variety of conditions by measuring changes in conductivity. Fabrication and testing of the 20ESB samples followed typical procedures. 20ESB powder was manufactured using solid-state methods. A stainless steel die was then used to press the powder into pellets. Unless otherwise noted, the ESB pellets were sintered at 890°C for 4 hours with a 5°C/min ramp rate for heating and cooling. The pellets were then polished using SiC paper and Au-paste (Heraues) painted on both sides for a current collector. ESB powder manufactured in house is denoted as HM ESB (homemade), while purchased powders (Trans Tech Inc.) is denoted as TT ESB.

Samples were loaded into a custom built reactor and heated to the testing temperature. Gas conditions ranged from 20% H_2O in air (21% O_2, bal. N_2) to dehumidified air, at both 650°C and 600°C. The results at 650°C and 600°C are shown in Figure 7.6 and Figure 7.7, respectively. At 650°C there is no change in ESB conductivity in air as a function of aging time with or without humidity. At 600°C we see an exponential decrease in the conductivity of ESB after approximately 25 hours at temperature.

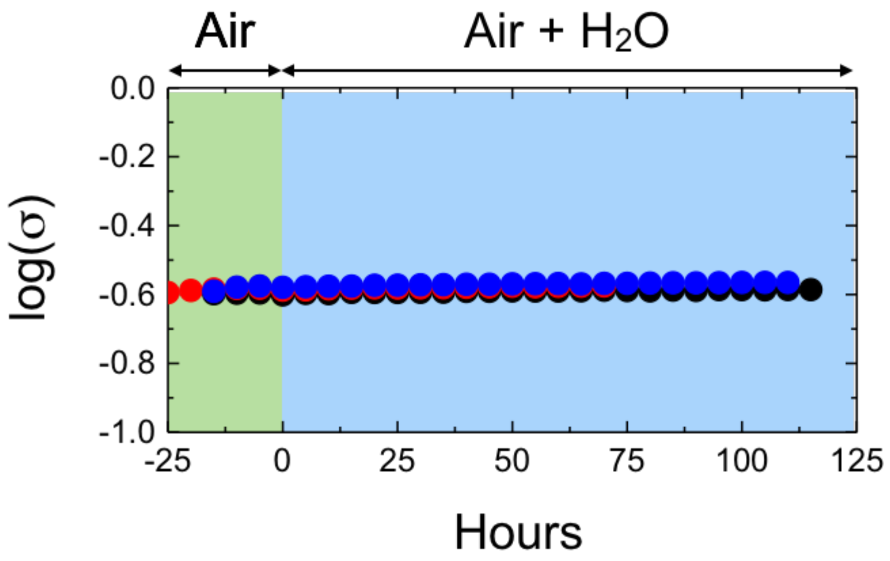

Figure 7.6: Conductivity as a function of time for ESB pellets tested in air (black, red) and air followed by 20% humidified air (blue) at 650°C. Area highlighted in green is without humidification, while area highlighted in blue is humidified.

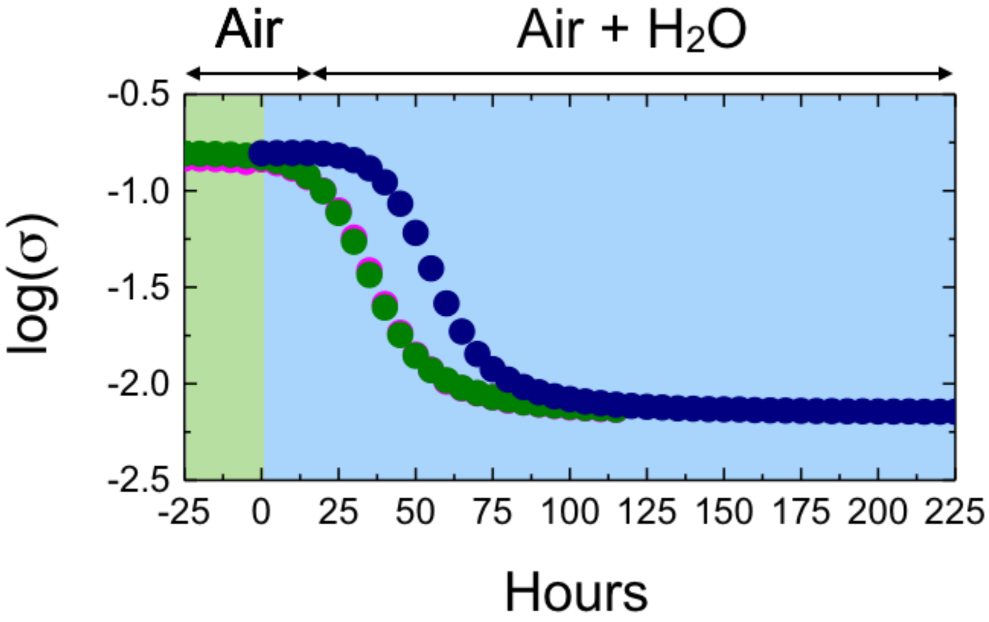

Figure 7.7: Conductivity as a function of time for ESB pellets tested in dehumidified air (green) and air followed by 20% humidified air (navy, pink) at 600°C. Area highlighted in green is without humidification, while area highlighted in blue is humidified.

After testing in both humidified and dehumidified conditions, the results indicate that the decrease in ESB conductivity is only a function of the disorder-order phase transition and not an effect of exposure to H_2O. The results for all humidification-induced aging experiments are shown in Table II. Our results show that there is no observable effect of H_2O on the performance or stability of ESB in air at operating temperatures.

Table II: Test conditions for ESB samples in various dehumidified and humidified conditions. HM and TT stand for ESB made using solid-state methods and purchased from Trans Tech Inc., respectively.

No.	Sample Desc.	Test Temp.	Test Cond.	Test Duration	Purpose	Status	Notes
1	HM ESB	650°C	3% H_2O in Air	100h	Baseline test	Completed	No degradation observed for 100h+
2	TT ESB	650°C	3% H_2O in Air	100h	Baseline test	Completed	No degradation observed for 70h+ **computer shutdown after 70hrs
4	HM ESB	650°C	20% H_2O in Air	100h	Observe if there is decay, if so, how it behaves	Completed	No degradation observed for 100h+
5	HM ESB	600°C	Dry Air (dehumidifier)	Degr. Rate Under 0.2% per hour (50+)	Baseline test	Completed	Degradation observed, rate of < 0.2% reached at 140 hrs
8	HM ESB	600°C	20% H_2O in Air	Degr. Rate Under 0.2% per hour (50+)	Compare with No. 7 to see difference and determine effect of high H_2O	Retested	Degradation observed, issues with gas flow/water content
9	HM ESB	retest*	No. 8			Completed	Very similar to No. 5 and 8(1)

7.3.2 Applied Bias

In addition to exposure to humidified gas environments, samples were also tested for stability under applied bias conditions. The 3-electrode cell configuration shown in Figure 7.8 was used to remove contributions of the half-cell under the opposite bias condition, (e.g. the side subject to reducing conditions is measured separate from the side under oxidizing conditions, the combination of which offsets the result). Unless specifically indicated, the samples consist of a 20ESB pellet with Au-paste working (WE) and counter (CE) electrodes, with a Au-paste reference electrode placed inside a grove around the circumference of the pellet, equidistant from the WE and CE surfaces.

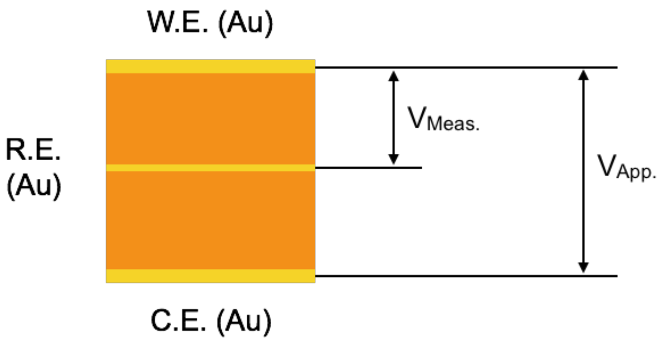

Figure 7.8: Cell configuration for measuring impedance under an applied bias on 20ESB pellets. A Au working electrode (WE), counter electrode (CE) and reference electrode (RE), allow the bias to be applied across the entire pellet, while the impedance measurement is only performed on one half of the cell.

Initial impedance measurements were made on 20ESB with Au electrodes under select cathodic and anodic biases ranging from -0.5V to 0.3V at 650°C. The Nyquist plot for each measurement is shown in Figure 7.9, where we can see a clear dependence of the impedance spectra on applied bias. At first glance, it is apparent that the size of the arc for low anodic biases decreases the total size of the arc, while low cathodic bias increases to total size of the arc. This trend for cathodic bias reverses for values greater (more negative) than -0.3V. To best visualize the effect of bias on the impedance spectra, 3-dimensional Bode plots have been developed. These plots, shown in Figure 7.10, are color maps that can be easily used to qualitatively describe how the magnitude and phase shift of the frequency response changes as a function applied bias. The magnitude, $|Z|$, the distance from the origin, is plotted in the z-axis in Figure 7.10 (a), while the phase shift, σ, is the z-axis in Figure 7.10 (b). Following along the y-axis, we can observe how the impedance spectra change as a function of applied bias. Clearly, there is a relationship between applied bias and the polarization resistance for a Au-electrode on an ESB pellet. The increase/decrease in polarization resistance under applied bias may be related to electronic defects in ESB under oxidizing and reducing conditions, similar to GDC.

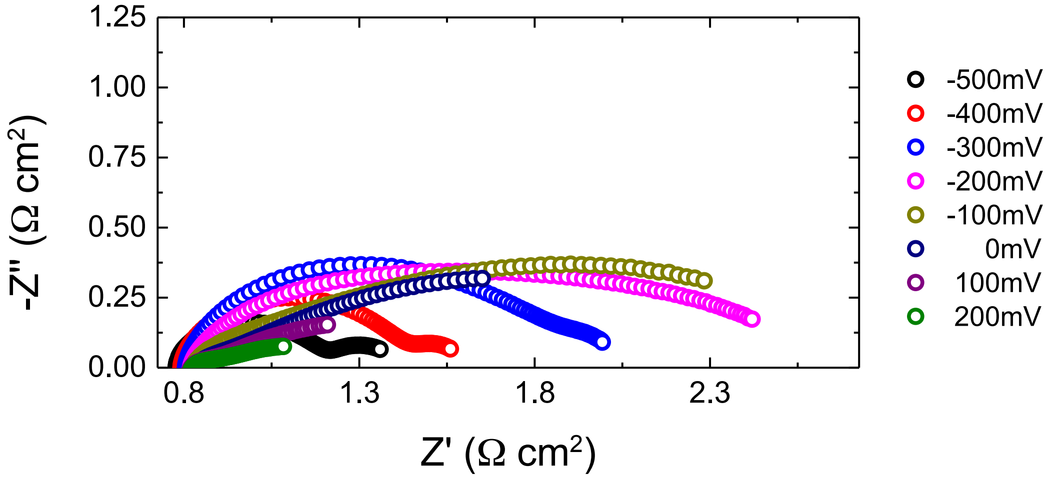

Figure 7.9: Select Nyquist plots for 20ESB measurements under applied bias. Anodic bias (OER) appears to decrease the total polarization resistance for cell, while a cathodic bias (ORR) appears to increase the spectra size at low bias (< 300mV) and decrease it at higher bias (> 300mV).

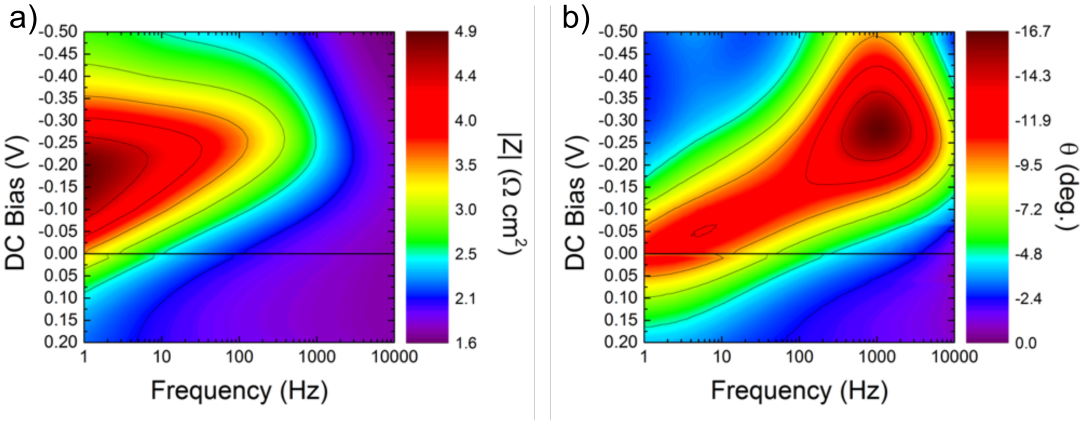

Figure 7.10: Contour Bode plots of (a) magnitude and (b) phase shift for a 20ESB 3-electrode sample under a range of polarization conditions. The plots provide a qualitative map for the effect of polarization on the impedance spectra.

One possibility that was explored is the reduction of Bi^{3+} to Bi^0 (metallic Bi). Under reducing conditions, it is possible to for Bi^0 on the surface to decrease the resistance of the cell, eventually leading to irreversible loss of the Bi_2O_3 phase. To test this possibility, the samples were held at increasing negative bias for ~16hrs. The conductivity as a function of time at each bias condition is plotted in Figure 7.11 (a), and the corresponding polarization resistance in a contour Bode plot in Figure 7.11 (b). In Figure 7.11 (a) we can see that although the conductivity appears to increase slightly with increasing cathodic bias, the conductivity at each bias appears to be constant. Additionally, the contour plot, with time along the y-axis, shows that the polarization resistance is also relatively stable. The changes in the polarization resistance as a function of applied bias indicate that the ESB electrolyte is playing an active role in the ORR. The odd dependence of polarization resistance on bias is being investigated further, and a future comparison to better-known materials, such as GDC and YSZ will be conducted.

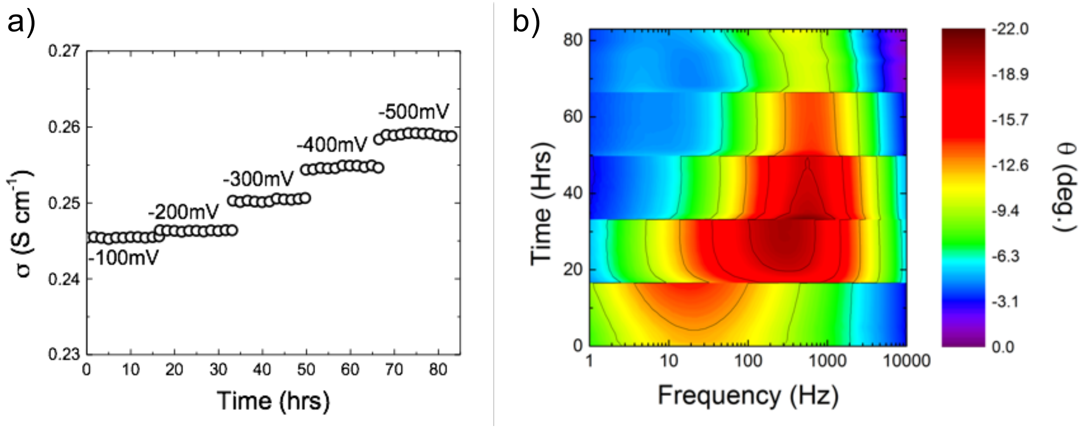

Figure 7.11: (a) Conductivity as a function of time for 20ESB with increasing DC bias. The conductivity appears to increase with increasing bias, while the conductivity is stable with short-term aging at each bias. (b) Phase shift (σ) as a function of frequency and aging time. Each horizontal line in the plot represents the phase shift in a Bode plot. The greater the red shift in the plot the higher the phase shift, which is representative of the size of the arc.

Analysis of the polarization resistance (or overpotential) as a function of the cell current was used to characterize the ORR of the Au/ESB interface. The electrode overpotential can be extracted from impedance measurements using:

$$\eta = i(R_T - R_\Omega) \tag{7.2}$$

where η is the electrode overpotential, i is the applied current, R_S is the ohmic resistance, and R_T the total resistance. Using Eq. 7.2 we can calculate η for different applied biases and plot the values versus log(i) to create a Tafel plot. From the Butler-Volmer equation, we can fit the slopes of the plots to extract the anodic and cathodic charge transfer coefficients, α_a and α_c, respectively, as well as the exchange current density i_0. Figure 7.12 depicts log(i_0) as a function of η for the Au-electrode on ESB at four PO_2's.

$$i = i_0 \left(\exp\left(\frac{\alpha_a F\eta}{RT}\right) - \exp\left(-\frac{\alpha_c F\eta}{RT}\right)\right) \qquad [7.3]$$

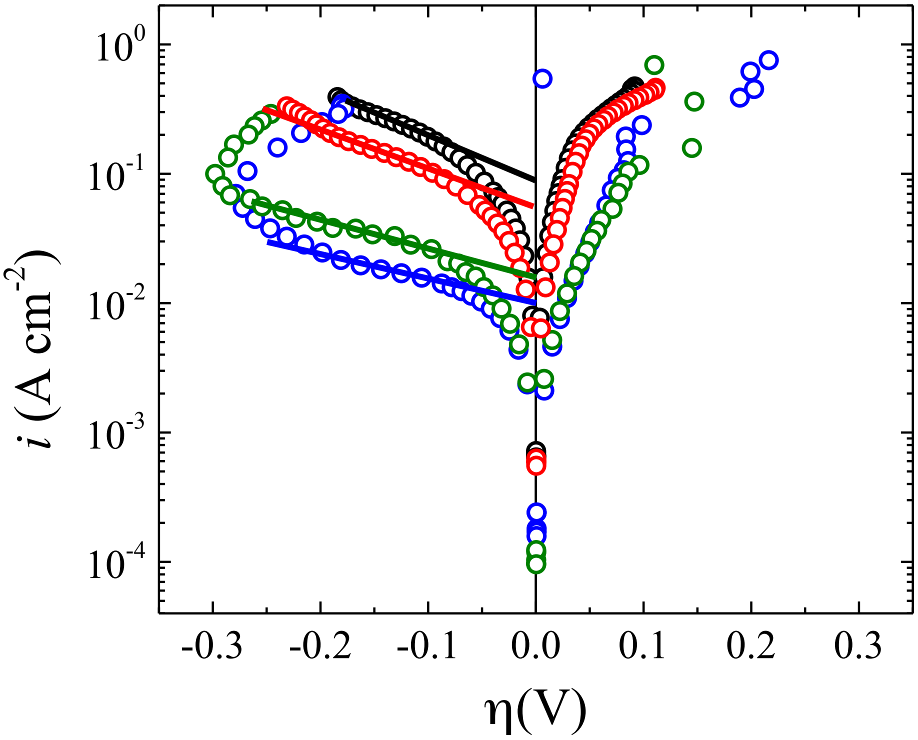

Figure 7.12: Tafel plots for an Au electrode on ESB at 650°C under different PO_2 conditions: 1 (black), 0.21 (red), 0.01 (green), and 0.0001 atm. (blue). Fitting the linear portions of the curves we extract values for the cathodic exchange current density and charge transfer coefficient for the Au/ESB interface.

Fitting the data, we get values for α_c and i_0 as a function of PO_2 shown in Figure 7.13 (a) and (b). The values are compared to results from van Hassel et al. on the Au/YSZ interface[127]. The values of α_c for Au/YSZ as well as Au/ESB are close to 0.5 at higher PO_2. However, α_c for Au/YSZ is stable, while that for Au/ESB decreases with decreasing PO_2. The value of the charge transfer coefficient is dependent on the rate-limiting step in the ORR, and should be near 0.5 if the rate-limiting step involves the transfer of a single electron[95]. The exchange current density extracted for Au/ESB is ~4 orders of magnitude greater than the values obtained for Au/YSZ. Additionally, we can determine the PO_2 dependence of i_0, where $i_0 \propto (PO_2)^m$. van Hassel et al. claim their value for Au/YSZ of $m \cong 0.60$ is indicative of a co-limited mass transport/charge transfer reaction. From Figure 7.13 (b) we extract a slope of $m \cong 0.25$. According to the model from van Hassel et al., a charge transfer coefficient of 0.5 and a value of $m = 3/8$ indicates that the oxygen exchange reaction is limited mainly by the charge transfer process. Based on our results ESB exhibits a higher exchange current flux than YSZ, which is desirable for electrolyte applications. However the PO_2 dependence of ESB suggest that the transport properties of ESB change during polarization, which could be a concern under real working conditions.

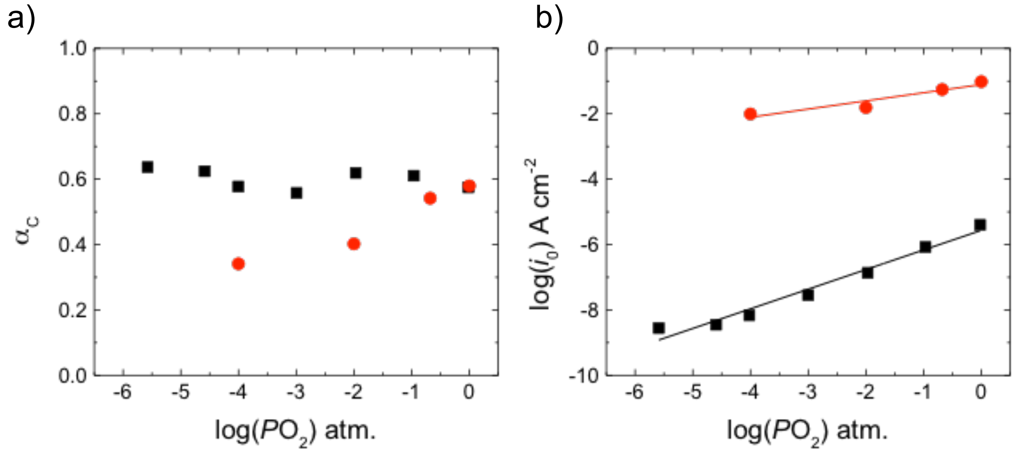

Figure 7.13: The cathodic charge transfer coefficient (a) and exchange current density (b) for a Au electrode on ESB as a function of PO_2. The values for Au/ESB are compared to those from van Hassel et al. for an Au/YSZ sample[127]. The results show a clear difference in the ORR for the two materials.

The sample tested in pure N_2 (PO_2=0.0001) showed signs of shorting during testing, as indicated by the rapid increase in current as a function of η. Images of the ESB pellet after -1V applied across the WE and CE are shown in Figure 7.14 (a) and (b). The cathode side of the sample showed current blackening under a reducing bias, a result of

Bi^0 formation. It is challenging to say exactly what PO_2 the surface of the ESB electrolyte experiences as the cell is tested in a single environment chamber. According to the Nernst equation, a potential of -0.5V vs. ref. in N_2 should produce a PO_2 of 10^{-10}, assuming the PO_2 of N_2 is 10^{-4}. The effect of applied bias on ESB is a concern that needs to be further analyzed for its use in bi-layer electrolytes.

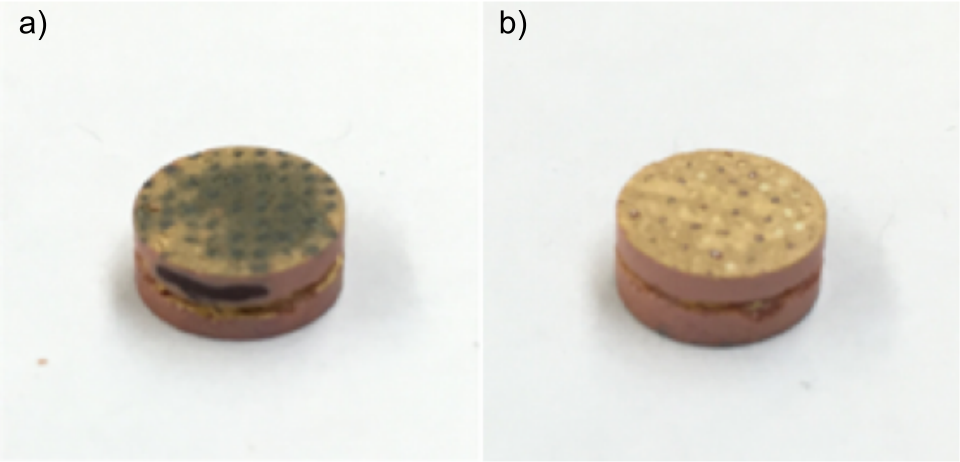

Figure 7.14: Photographs of the (a) WE and (b) CE sides of a Au-20ESB sample tested in pure N_2 (PO_2 = 0.0001 atm.) at 650°C under increasing cathodic polarization up to -0.5V vs. ref. Blackening of the sample is representative of reduction of Bi^{3+} to Bi^0.

7.4 *Performance and Stability of β-phase $Nd_{0.08}Gd_{0.08}Bi_{1.84}O3$*

The performance of composite NGSB ($Nd_{0.04}Gd_{0.04}Bi_{0.92}O_3$) and LSM ($La_{0.80}Sr_{0.20}MnO_3$) was also tested and compared to that of LSM-ESB, one of the highest performance cathode materials. NGSB is a newly developed doped-bismuth oxide electrolyte for low/intermediate temperature SOFCs. Figure 7.15 compares the conductivity and stability of NGSB at 500°C to that of ESB at both 600°C and 500°C. After over 700 hours of aging, the conductivity of NGSB is over an order of magnitude higher than that of ESB. The rhombohedral β_1/β_2-phase does not undergo the ordering process that is observed for the cubic δ-phase (ESB), and the low dopant concentration helps to maintain higher initial conductivities. This is attributed to the rhombohedral structure and low dopant concentration of the material, as the rare earth-oxygen (RE-O) bond is stronger than the bismuth-oxygen (Bi-O) bond.

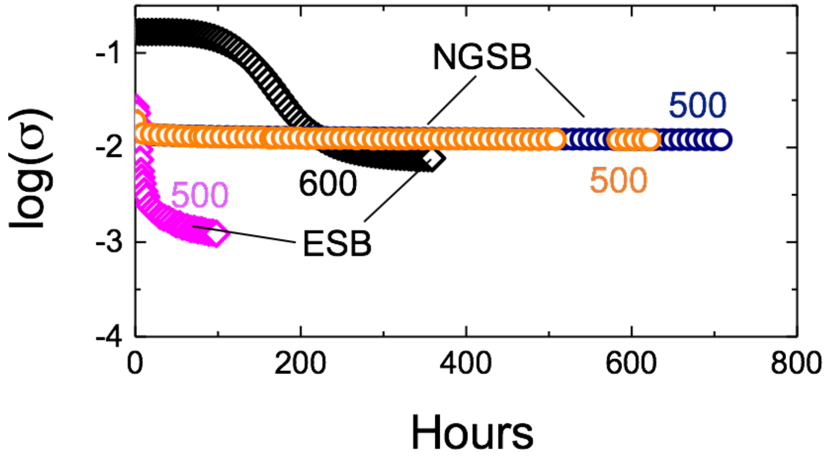

Figure 7.15: A comparison of conductivity and ordering in 20ESB and 4N4GDB. The conductivity of 20ESB undergoes ordering at both 600°C and 500°C, while the NGSB appears to maintain stable conductivity for over 700 hours.

Symmetrical cells were fabricated by pressing NGSB pellets and blade coating NGSB-LSM and LSM-ESB pastes onto separate cells. The pastes were made by mixing a 50-50 volume % of solid state NGSB and ESB powders with LSM (Fuel Cell Materials) and ESL441 vehicle (ESL ElectroScience). The conductivity and area specific resistance (ASR) at 500°C for each cell is shown in Figure 7.16. The electrical conductivity (left axis, top plots) for both samples is equal. This is expected, as both cathodes have been deposited on NGSB pellets, which accounts for the majority of the electrical resistance in the cell.

In contrast the ASR for the NGSB-LSM after 700 hours is 3x lower than that of the ESB-LSM. For the ESB-LSM sample, we see a rapid increase in ASR at the beginning of the aging process, which is likely attributed to oxygen ordering at 500°C. As ordering does not occur in the rhombohedral phase, the ASR for NGSB-LSM is stable as a function of time. The performance and stability of NGSB and NGSB-LSM composite is promising for the development of new electrolyte and cathode materials for high performance bi-layer fuel cells. Future development for bi-layer fuel cell operation below 650°C should be toward the improvement of non-ordering Bi_2O_3 materials.

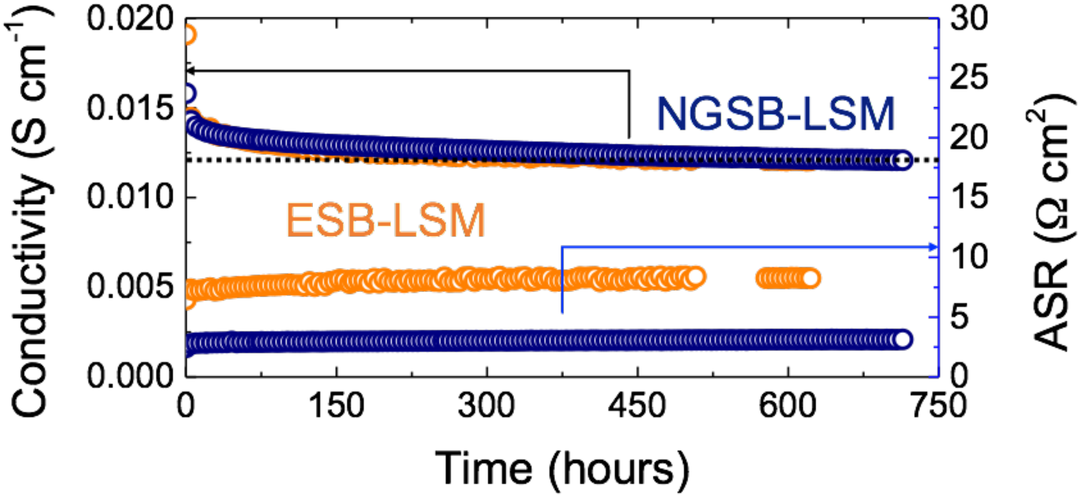

Figure 7.16: The conductivity and ASR of composite 20ESB-LSM and 4N4GSB-LSM. Both samples show some initial decrease in conductivity, while the 20ESB-LSM shows an ASR 3x greater than 4N4GSB, with a rapid increase initially, corresponding to the drop in conductivity caused by ordering.

7.5 Conclusions

The high conductivity of stabilized bismuth oxides is attractive for use as an electrolyte in SOFCs, and the concept of a bi-layer electrolyte provides a new avenue for high performance SOFCs, where materials that unstable in oxidizing and reducing atmospheres can be separated. The stability of ESB in H_2O conditions at operating temperatures does not appear to be an issue for implementation. Further investigation on the stability of LSM-ESB cathodes may yield a different result. An interesting aspect of ESB is the possibility of its more active role (compared to other electrolytes) in the ORR and therefore, the significant improvement of LSM-ESB cathodes over LSM composites. This role becomes more evident under polarization studies using Au as an electrode, as

Au has very limited activity for the ORR. Further investigation of how exactly ESB participates in the ORR could help in the identification of electronically conductive materials other than LSM, as neither the conductivity nor the dissociation kinetics on LSM are particularly high, when compared to comparable materials. Although ESB electrolyte and cathode performance is high, the operating window for the material is not very large, as exposure to temperatures below 650°C leads to ordering of the oxygen sub-lattice and a ~2 order of magnitude drop in conductivity. New materials such as NGSB clearly show an alternate route to achieve both high electrolyte conductivities at temperatures below 650°C and potential for new high performance cathode materials as well, where the ASR of LSM-NGSB at 500°C is 3x lower than that of LSM-ESB after 600 hours.

Chapter 8: Future Work

EIS and isotope exchange have been used to investigate the ORR reaction for SOFC cathode materials, in terms of the fundamental mechanisms as well as the role of the gas phase contaminants CO_2 and water. As an individual technique, EIS provides a vast amount of data for electrode performance; however, de-convolution of the data is challenging and often leads to little mechanistic information due to the complexities of the cathode microstructure. On the other hand, the test conditions in isotope exchange are capable of probing oxygen exchange kinetics and identifying specific oxygen exchange pathways. Additionally, isotope exchange can easily be modified to study how CO_2 and water exchange both with and without the presence of O_2, helping elucidate the reactions of O-containing gaseous species. The drawback of isotope exchange is that it is not performed on real electrodes and does not include the effects microstructure and electrode/electrolyte interfaces, and most importantly electrochemical potentials. Therefore, we proposed *in operando* isotope exchange as a potential technique to combine the best aspects of isotope exchange and impedance spectroscopy, which can be performed on the same sample under the same operating conditions. Recommendations for future work are listed below:

1. CO_2 on LSCF shows a reversible change in the overall impedance spectra. It suggests that the effect of CO_2 on the cathode could be removed after exposing to the fresh air. Applied bias conditions, where the O atom in adsorbed CO_2 is being driven into the electrolyte, may yield a different result. Studies aimed at identifying how CO_2 interacts with LSCF under operating conditions could yield

important mechanistic insights. *In operando* surface characterization techniques could provide such information.

2. EIS and isotope exchange on LSM, YSZ, and LSM-YSZ suggests that the pathway for the ORR is inherently dependent on the properties of the materials in question. Expanding the scope of studied materials to LSM-ESB and LSM-GDC would help to identify the role of the electrolyte in the ORR and the rational design of new high performance cathode materials and composites.
3. EIS and isotope exchange also show that water has a different impact on LSM, YSZ, and LSM-YSZ composite. A combination of ambient pressure-photoelectron spectroscopy (AP-XPS) and isotope exchange would help elucidate why water promotes the surface exchange rate on some materials, while it inhibits exchange on others.
4. It is important that complementary technique used to study electrode kinetics and mechanisms, be performed on samples with similar or quantifiable structural/interfacial parameters, or ideally on the same samples. One limitation of most techniques employed currently that fulfill this requirement, is that the samples are often quite dissimilar to those used in real cells. Therefore, exploring new experimental designs, such as *in operando* isotope exchange, could provide unique results unachievable with other techniques.
5. Results show that the role of the electrolyte in a composite cathode is significant. Further investigation of how ESB participates in the ORR could lead to improved performance through replacement of LSM. Although ESB electrolyte and cathode performance is high, the material suffers from oxygen ordering. New stabilized

bismuth oxides that don’t undergo an order-disorder transformation, such as rhombohedral phase NGSB, show an alternate route to achieve both high electrolyte conductivities at temperatures below 650°C and the potential for novel high performance composite cathodes.

Bibliography

(1) Wachsman, E. D.; Lee, K. T. *Science* **2011**, *334* (6058), 935–939.

(2) Steele, B. C. H. *Mater. Sci. Eng. B* **1992**, *13*, 79–87.

(3) Singhal, S.; Kendall, K. *High-temperature solid oxide fuel cells*; Elsevier Advanced Technology: New York, 2003.

(4) Wachsman, E. D.; Marlowe, C. A.; Lee, K. T. *Energy Environ. Sci.* **2012**, *5* (2), 5498–5509.

(5) Simner, S. P.; Anderson, M. D.; Engelhard, M. H.; Stevenson, J. W. *Electrochem. Solid-State Lett.* **2006**, *9* (10), A478–A481.

(6) Hsiao, Y. C.; Selman, J. R. *Solid State Ionics* **1997**, *98*, 33–38.

(7) Yokokawa, H.; Tu, H.; Iwanschitz, B.; Mai, A. *J. Power Sources* **2008**, *182* (2), 400–412.

(8) Ivers-Tiffée, E.; Weber, A.; Herbstritt, D. *J. Eur. Ceram. Soc.* **2001**, *21*, 1805–1811.

(9) DOE EERE. Solid oxide fuel cells http://energy.gov/eere/fuelcells/types-fuel-cells (accessed May 1, 2015).

(10) Boreskov, G. K. *Heterogeneous Catalysis*; Nova Science Publishers: Hauppauge, New York, 2003.

(11) Chorkendorff, I.; Niemantsverdriet, J. W. *Concepts of modern catalysis and kinetics*; Wiley-VCH: Weinheim Germany, 2003.

(12) Kan, C. C.; Kan, H. H.; Van Assche IV, F. M.; Armstrong, E. N.; Wachsman, E. D. *J. Electrochem. Soc.* **2008**, *155* (10), B985–B993.

(13) Carter, S.; Selcuk, A.; Chater, R. J.; Kajda, J.; Kilner, J. A.; Steele, B. C. H. *Solid State Ionics* **1992**, *53–56*, 597–605.

(14) Mastrikov, Y. A.; Merkle, R.; Heifets, E.; Kotomin, E. A.; Maier, J. *J. Phys. Chem. C* **2010**, *114* (7), 3017–3027.

(15) Adler, S. B. *Chem. Rev.* **2004**, *104* (10), 4791–4843.

(16) Jiang, S. P. *Solid State Ionics* **2002**, *146* (1–2), 1–22.

(17) Yamazoe, N.; Teraoka, Y. *Catal. Today* **1990**, *8*, 175–199.

(18) Mizusaki, J.; Tagawa, H.; Naraya, K.; Sasamoto, T. *Solid State Ionics* **1991**, *49*, 111–118.

(19) Mizusaki, J.; Yonemura, Y.; Kamata, H.; Ohyama, K.; Mori, N.; Takai, H.; Tagawa, H.; Dokiya, M.; Naraya, K.; Sasamoto, T.; Inaba, H.; Hashimoto, T. *Solid State Ionics* **2000**, *132*, 167–180.

(20) Lane, J. A.; Benson, S. J.; Waller, D.; Kilner, J. A. *Solid State Ionics* **1999**, *121*, 201–208.

(21) Wang, S.; Katsuki, M.; Dokiya, M.; Hashimoto, T. *Solid State Ionics* **2003**, *159* (1–2), 71–78.

(22) Bouwmeester, H. J. M.; Den Otter, M. W.; Boukamp, B. A. *J. Solid State Electrochem.* **2004**, *8* (9), 599–605.

(23) Østergård, M. J. L.; Clausen, C.; Bagger, C.; Mogensen, M. *Electrochim. Acta* **1995**, *40*, 1971–1981.

(24) Juhl, M.; Primdahl, S.; Manon, C.; Mogensen, M. *J. Power Sources* **1996**, *61*, 173–181.

(25) Murray, E. P.; Sever, M. J.; Barnett, S. A. *Solid State Ionics* **2002**, *148* (1–2), 27–

34.
(26) Yamamoto, O.; Takeda, Y.; Kanno, R.; Noda, M. *Solid State Ionics* **1987**, *22*, 241–246.
(27) Murray, E. P.; Tsai, T.; Barnett, S. A. *Solid State Ionics* **1998**, *110*, 235–243.
(28) Hagen, A.; Chen, M.; Neufeld, K.; Liu, Y. L. *ECS Trans.* **2009**, *25* (2), 439–446.
(29) Oh, D.; Gostovic, D.; Wachsman, E. D. *J. Mater. Res.* **2012**, *27* (15), 1992–1999.
(30) Nielsen, J.; Mogensen, M. *Solid State Ionics* **2011**, *189* (1), 74–81.
(31) Chen, A.; Smith, J. R.; Duncan, K. L.; DeHoff, R. T.; Jones, K. S.; Wachsman, E. D. *J. Electrochem. Soc.* **2010**, *157* (11), B1624–B1628.
(32) Wang, W.; Jiang, S. P. *Solid State Ionics* **2006**, *177* (15–16), 1361–1369.
(33) Benson, S. J.; Waller, D.; Kilner, J. A. *J. Electrochem. Soc.* **1999**, *146*, 1305–1309.
(34) Raz, S.; Sasaki, K.; Maier, J.; Riess, I. *Solid State Ionics* **2001**, *143* (2), 181–204.
(35) Sakai, N.; Yamaji, K.; Horita, T.; Xiong, Y. P.; Kishimoto, H.; Yokokawa, H. *J. Electrochem. Soc.* **2003**, *150* (6), A689–A694.
(36) Zhao, Z.; Liu, L.; Zhang, X.; Wu, W.; Tu, B.; Ou, D.; Cheng, M. *J. Power Sources* **2013**, *222*, 542–553.
(37) Nielsen, J.; Hagen, A.; Liu, Y. L. *Solid State Ionics* **2010**, *181* (11–12), 517–524.
(38) Zhao, Z.; Liu, L.; Zhang, X.; Wu, W.; Tu, B.; Cui, D.; Ou, D.; Cheng, M. *Int. J. Hydrogen Energy* **2013**, *38* (35), 15361–15370.
(39) Yu, Y.; Luo, H.; Cetin, D.; Lin, X.; Ludwig, K.; Pal, U.; Gopalan, S.; Basu, S. *Appl. Surf. Sci.* **2014**, *323*, 71–77.
(40) Cronin, J. S.; Muangnapoh, K.; Patterson, Z.; Yakal-Kremski, K. J.; Dravid, V. P.; Barnett, S. A. *J. Electrochem. Soc.* **2012**, *159* (4), B385–B393.
(41) Matsui, T.; Mikami, Y.; Muroyama, H.; Eguchi, K. *J. Power Sources* **2013**, *242*, 790–796.
(42) Macdonald, J. R. *Ann. Biomed. Eng.* **1992**, *20*, 289–305.
(43) Barsoukov, E.; Macdonald, J. R. *Impedance Spectroscopy: Theory, Experiment, and Applications*, Second Edi.; Wiley-Interscience: Hoboken, 2005.
(44) Barbucci, A.; Bozzo, R.; Cerisola, G.; Costamanga, P. *Electrochim. Acta* **2002**, *47*, 2183–2188.
(45) Jørgensen, M. J.; Primdahl, S.; Mogensen, M. *Electrochim. Acta* **1999**, *44*, 4195–4201.
(46) Baumann, F. S.; Fleig, J.; Habermeier, H. U.; Maier, J. *Solid State Ionics* **2006**, *177* (11–12), 1071–1081.
(47) Jørgensen, M. J.; Mogensen, M. *J. Electrochem. Soc.* **2001**, *148* (5), A433–A442.
(48) Nielsen, J.; Hjelm, J. *Electrochim. Acta* **2014**, *115*, 31–45.
(49) Schichlein, H.; Muller, A. C.; Krugel, A.; Ivers-Tiffée, E. *J. Appl. Electrochem.* **2002**, *32*, 875–882.
(50) Randles, J. E. B. *Discuss. Faraday Soc.* **1947**, *1*, 11.
(51) Boukamp, B. a. *tm - Tech. Mess.* **2004**, *71* (9–2004), 454–459.
(52) Bouwmeester, H. J. M.; Song, C.; Zhu, J.; Yi, J.; van Sint Annaland, M.; Boukamp, B. A. *Phys. Chem. Chem. Phys.* **2009**, *11* (42), 9640–9643.
(53) den Otter, M. W.; Boukamp, B. A.; Bouwmeester, H. J. M. *Solid State Ionics* **2001**, *139*, 89–94.
(54) De Souza, R. A.; Zehnpfenning, J.; Martin, M.; Maier, J. *Solid State Ionics* **2005**, *176* (15–16), 1465–1471.

(55) Horita, T.; Shimonosono, T.; Kishimoto, H.; Yamaji, K.; Brito, M. E.; Yokokawa, H. *Solid State Ionics* **2012**, *225*, 141–145.

(56) Kilner, J. A.; Skinner, S. J.; Brongersma, H. H. *J. Solid State Electrochem.* **2011**, *15* (5), 861–876.

(57) Armstrong, E. N.; Duncan, K. L.; Oh, D. J.; Weaver, J. F.; Wachsman, E. D. *Journal of The Electrochemical Society*. 2011, pp B492–B499.

(58) Armstrong, E. N.; Duncan, K. L.; Wachsman, E. D. *Phys. Chem. Chem. Phys.* **2013**, *15* (7), 2298–2308.

(59) Hargreaves, J. S. J.; Mellor, I. M. 2006; pp 115–132.

(60) Kan, C. C.; Wachsman, E. D. *Solid State Ionics* **2010**, *181* (5–7), 338–347.

(61) Huang, Y.-L.; Pellegrinelli, C.; Wachsman, E. D. *ACS Catal.* **2016**, *6*, 6025–6032.

(62) Kan, C. C.; Kan, H. H.; Van Assche, F. M.; Armstrong, E. N.; Wachsman, E. D. *J. Electrochem. Soc.* **2008**, *155* (10), B985.

(63) Armstrong, E. N.; Duncan, K. L.; Wachsman, E. D. *J. Electrochem. Soc.* **2011**, *158* (3), B283–B298.

(64) Huang, Y.-L.; Pellegrinelli, C.; Wachsman, E. D. *J. Electrochem. Soc.* **2016**, *163* (3), F171–F182.

(65) Huang, Y.-L. Fundamental understanding of SOFC cathode durability; A kinetics and catalysis study, University of Maryland, College Park, 2015.

(66) Klier, K.; Novakova, J.; Jiru, P. *J. Catal.* **1963**, *2* (6), 479–484.

(67) Boreskov, G. K. *Discuss. Faraday Soc.* **1966**, *41*, 263–276.

(68) Crank, J. *The Mathematics of Diffusion*, 2nd ed.; Clarendon Press: Oxford, Eng, 1975.

(69) Huang, Y.-L.; Pellegrinelli, C.; Wachsman, E. D. *J. Electrochem. Soc.* **2016**, *163* (3), F171–F182.

(70) Hayd, J.; Ivers-Tiffee, E. *J. Electrochem. Soc.* **2013**, *160* (11), F1197–F1206.

(71) Hagen, A.; Neufeld, K.; Liu, Y. L. *J. Electrochem. Soc.* **2010**, *157* (10), B1343–B1348.

(72) Bucher, E.; Sitte, W.; Klauser, F.; Bertel, E. *Solid State Ionics* **2012**, *208*, 43–51.

(73) Arregui, A.; Rodriguez-Martinez, L. M.; Modena, S.; Bertoldi, M.; Sglavo, V. M. *Fuel Cells* **2013**, *13* (5), 720–728.

(74) Gong, Y.; Patel, R. L.; Liang, X.; Palacio, D.; Song, X.; Goodenough, J. B.; Huang, K. *Chem. Mater.* **2013**, *25* (21), 4224–4231.

(75) ten Elshof, J. E.; Bouwmeester, H. J. M.; Verweij, H. *Appl. Catal. A Gen.* **1995**, *130*, 195–212.

(76) Huang, Y.-L.; Pellegrinelli, C.; Wachsman, E. D. *In Progress*; 2016.

(77) Adler, S. B.; Lane, J. A.; Steele, B. C. H. *J. Electrochem. Soc.* **1996**, *143*, 3554–3564.

(78) Adler, S. B. *Solid State Ionics* **1998**, *111*, 125–134.

(79) Hildenbrand, N.; Boukamp, B. A.; Nammensma, P.; Blank, D. H. A. *Solid State Ionics* **2011**, *192* (1), 12–15.

(80) Jorcin, J.-B.; Orazem, M. E.; Pébère, N.; Tribollet, B. *Electrochim. Acta* **2006**, *51*, 1473–1479.

(81) Xia, C.; Liu, M. *Society* **2001**, *905* (8), 1903–1905.

(82) Steele, B. C. H. *Solid State Ionics* **2000**, *129*, 95–110.

(83) Chueh, W. C.; Abbott, M.; Scipio, D.; Haile, S. M. *Science* **2010**, *63* (December),

2010.
(84) Hong, W. T.; Risch, M.; Stoerzinger, K. A.; Grimaud, A.; Suntivich, J.; Shao-Horn, Y. *Energy Environ. Sci.* **2015**, *8* (5), 1404–1427.
(85) Fleig, J. *Annu. Rev. Mater. Res.* **2003**, *33* (1), 361–382.
(86) Ding, D.; Li, X.; Lai, S. Y.; Gerdes, K.; Liu, M. *Energy Environ. Sci.* **2014**, *7* (2), 552–575.
(87) Haider, M. A.; McIntosh, S. *J. Electrochem. Soc.* **2009**, *156* (12), B1369–B1375.
(88) Kan, C. C.; Kan, H. H.; Van Assche IV, F. M.; Armstrong, E. N.; Wachsman, E. D. *J. Electrochem. Soc.* **2008**, *155* (10), B985–B993.
(89) Ji, Y.; Kilner, J. A.; Carolan, M. F. *Solid State Ionics* **2005**, *176* (9–10), 937–943.
(90) De Souza, R. A.; Kilner, J. A. *Solid State Ionics* **1998**, *106*, 175–187.
(91) Duong, A. T.; Mumm, D. R. *J. Electrochem. Soc.* **2012**, *159* (1), B40.
(92) Pakalapati, S.; Gerdes, K.; Finklea, H.; Gong, M.; Liu, X.; Celik, I. *Solid State Ionics* **2014**, *258*, 45–60.
(93) Finklea, H.; Gerdes, K.; Lee, S.; Fann, L.; Hackett, G.; Abernathy, H.; Energy, N.; Virginia, W. 4000.
(94) Adler, S. B.; Chen, X. Y.; Wilson, J. R. *J. Catal.* **2007**, *245* (1), 91–109.
(95) van Hassel, B. A.; Boukamp, B. A.; Burggraaf, A. J. *Solid State Ionics* **1991**, *48*, 139–154.
(96) van Hassel, B. A.; Boukamp, B. A.; Burggraaf, A. J. *Solid State Ionics* **1992**, *51*, 161–174.
(97) Hsieh, G.; Ford, S. J.; Mason, T. O.; Pederson, L. R. *Solid State Ionics* **1996**, *91*, 191–201.
(98) Wilson, J. R.; Cronin, J. S.; Duong, A. T.; Rukes, S.; Chen, H. Y.; Thornton, K.; Mumm, D. R.; Barnett, S. *J. Power Sources* **2010**, *195*, 1829–1840.
(99) Nielsen, J.; Hjelm, J. *Electrochim. Acta* **2014**, *115*, 31–45.
(100) Huber, T. M.; Kubicek, M.; Opitz, a. K.; Fleig, J. *J. Electrochem. Soc.* **2014**, *162* (3), F229–F242.
(101) Sakai, N.; Yamaji, K.; Horita, T.; Kishimoto, H.; Xiong, Y. P.; Yokokawa, H. *Solid State Ionics* **2004**, *175* (1–4), 387–391.
(102) Sakai, N.; Yamaji, K.; Horita, T.; Xiong, Y. P.; Kishimoto, H.; Brito, M. E.; Yokokawa, H. *Solid State Ionics* **2004**, *174* (1–4), 103–109.
(103) Kim, S. H.; Shim, K. B.; Kim, C. S.; Chou, J. T.; Oshima, T.; Shiratori, Y.; Ito, K.; Sasaki, K. *J. Fuel Cell Sci. Technol.* **2010**, *7* (2), 21011.
(104) Knöfel, C.; Chen, M.; Mogensen, M. *Fuel Cells* **2011**, *11* (5), 669–677.
(105) Nielsen, J.; Mogensen, M. *Solid State Ionics* **2011**, *189* (1), 74–81.
(106) Bucher, E.; Sitte, W.; Klauser, F.; Bertel, E. *Solid State Ionics* **2011**, *191* (1), 61–67.
(107) Feng, Z. a; Machala, M. L.; Chueh, W. C. *Phys. Chem. Chem. Phys.* **2015**, *17* (18), 12273–12281.
(108) Hu, B.; Mahapatra, M. K.; Singh, P. *J. Ceram. Soc. Japan* **2015**, *123* (1436), 199–204.
(109) Georges, S.; Skinner, S. J.; Lacorre, P.; Steil, M. C. *Dalton Trans.* **2004**, No. 19, 3101–3105.
(110) Liu, J.; Chater, R. J.; Morris, R. J. H.; Skinner, S. J. *Solid State Ionics* **2011**, *189* (1), 39–44.

(111) Kessel, M.; De Souza, R. A.; Yoo, H. I.; Martin, M. *Appl. Phys. Lett.* **2010**, *97* (2), 95–98.

(112) Pietrowski, M. J.; De Souza, R. A.; Fartmann, M.; Ter Veen, R.; Martin, M. *Fuel Cells* **2013**, *13* (5), 673–681.

(113) Nenning, A.; Navickas, E.; Hutter, H.; Fleig, J. *J. Phys. Chem. Lett.* **2016**, *7* (14), 2826–2831.

(114) Yokokawa, H. *Solid State Ionics* **2012**, *225*, 6–17.

(115) Feng, Z. a; El Gabaly, F.; Ye, X.; Shen, Z.-X.; Chueh, W. C. *Nat. Commun.* **2014**, *5*, 4374.

(116) Fleig, J. *Phys. Chem. Chem. Phys.* **2009**, *11* (17), 3144.

(117) Fleig, J.; Schintlmeister, A.; Opitz, A. K.; Hutter, H. *Scr. Mater.* **2011**, *65* (2), 78–83.

(118) Mueller, D. N.; Machala, M. L.; Bluhm, H.; Chueh, W. C. *Nat. Commun.* **2015**, *6*, 6097.

(119) Aidhy, D. S.; Nino, J. C.; Sinnott, S. B.; Wachsman, E. D.; Phillpotw, S. R. *J. Am. Ceram. Soc.* **2008**, *91* (7), 2349–2356.

(120) Fung, K. Z.; Chen, J.; Virkar, A. V. *J. Am. Ceram. Soc.* **1993**, *76*, 2403–2418.

(121) Jiang, N.; Wachsman, E. D. *J. Am. Ceram. Soc.* **1999**, *82*, 3057–3064.

(122) Jung, D. W.; Nino, J. C.; Duncan, K. L.; Bishop, S. R.; Wachsman, E. D. *Ionics (Kiel).* **2010**, *16* (2), 97–103.

(123) Wachsman, E. D.; Boyapati, S.; Kaufman, M. J. *J. Am. Ceram. Soc.* **2000**, *83*, 1964–1968.

(124) Jung, S.-H.; Wachsman, E. D.; Jiang, N. *Ionics (Kiel).* **2002**, *8*, 210.

(125) Avrami, M. *J. Chem. Phys.* **1940**, *8*, 212–224.

(126) Huang, C.-C.; Fung, K.-Z. *J. Mater. Res.* **2011**, *18* (11), 2624–2632.

(127) van Hassel, B. A.; Boukamp, B. A.; Burggraaf, A. J. *Solid State Ionics* **1991**, *48*, 155–171.